SPRINGER BRIEFS IN MATERIALS

E. McCafferty

Surface Chemistry of Aqueous Corrosion Processes

Springer

SpringerBriefs in Materials

More information about this series at http://www.springer.com/series/10111

E. McCafferty

Surface Chemistry of Aqueous Corrosion Processes

Springer

E. McCafferty
Alexandria, VA
USA

ISSN 2192-1091 ISSN 2192-1105 (electronic)
SpringerBriefs in Materials
ISBN 978-3-319-15647-7 ISBN 978-3-319-15648-4 (eBook)
DOI 10.1007/978-3-319-15648-4

Library of Congress Control Number: 2015932239

Springer Cham Heidelberg New York Dordrecht London

Printed on acid-free paper

Springer International Publishing AG Switzerland is part of Springer Science+Business Media (www.springer.com)

Preface

This communication utilizes a surface chemistry/physical chemistry approach toward the study of aqueous corrosion processes. Topics included are acid–base properties of surface oxide films, capillarity and corrosion, corrosion inhibition, metal/polymer adhesion, formation of water films on the iron oxide surface, passivity of Fe–Cr and Fe–Cr–Ni alloys, the relationship between the isoelectric point and the potential of zero charge for passive metals, and the uptake of chloride ions and the pitting of aluminum.

Alexandria, VA, USA, 2015 E. McCafferty

Contents

Chapter 1
Acid-Base Properties of Surface Oxide Films

Introduction

The properties of metal oxide films are important in a number of corrosion phenomena, including passivity and its breakdown, corrosion inhibition by organic molecules, and the adhesion of organic coatings. In addition, the properties of metal oxide films are important in related surface phenomena, such as friction and wear, lubrication, and electrocatalysis. This chapter will consider the acid-base nature of oxide films and the role of acid-base properties in pitting, the adhesion of organic coatings, and corrosion inhibition. Examples and references given here are intended to be illustrative rather than being exhaustive.

Surface Hydroxyl Groups

It is well known that oxide surfaces or oxide-covered metals exposed to either the ambient environment or immersed in aqueous solutions terminate in an outermost layer of hydroxyl groups due to their interaction with water molecules [1–3]. The reaction of a surface oxide with a water molecule is depicted in Fig. 1.1. Using quantitative X-ray photoelectron spectroscopy, the concentration of surface hydroxyls in the air-formed oxide films on various metals has been found to be 6–20 OH groups/nm^2 [4]. The depth of the hydroxylated region extends 5–8 Å into the oxide. Although the surface hydroxyl layer is quite thin, it has nonetheless a large influence on the properties of the oxide film, especially on its surface charge.

In aqueous solutions, the surface hydroxyl groups may remain undissociated. In such an instance, the oxide surface is said to be at its isoelectric point (pH_{pzc}) and will have a net surface charge of zero. This will occur only if the pH of the aqueous solution has the same value as the isoelectric point of the oxide. It is more likely,

E. McCafferty, *Surface Chemistry of Aqueous Corrosion Processes*,
SpringerBriefs in Materials, DOI 10.1007/978-3-319-15648-4_1

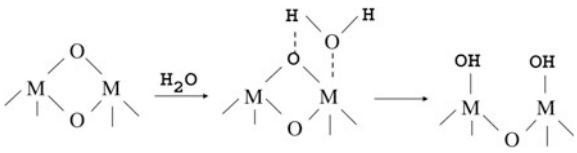

Fig. 1.1 Interaction of a water molecule with a metal oxide surface to form an outermost layer of surface hydroxyl groups

however, that the oxide film will be charged. If the pH is less than the isoelectric point, the surface will acquire a positive charge:

$$-\mathrm{MOH_{surf}} + \mathrm{H^+_{(aq)}} \rightleftharpoons -\mathrm{MOH_2{}^+{}_{surf}} \tag{1.1}$$

where M denotes a surface site occupied by a metal cation. If the pH is greater than the isoelectric point, the surface will acquire a negative charge:

$$-\mathrm{MOH_{surf}} + \mathrm{OH^-} \rightleftharpoons -\mathrm{MO^-{}_{surf}} + \mathrm{H_2O}$$

or:

$$-\mathrm{MOH_{surf}} \rightleftharpoons -\mathrm{MO^-{}_{surf}} + \mathrm{H^+_{(aq)}} \tag{1.2}$$

In the above reactions the surface species $-\mathrm{MOH_2^+}$ is a Bronsted acid because it is a proton donor [in the reverse direction of Eq. (1.1)]; and $-\mathrm{MO^-}$ is a Bronsted base in Eq. (1.2) (reverse direction) because it is a proton acceptor. The surface species $-\mathrm{MOH}$ is amphoteric, being a Bronsted base in Eq. (1.1) (forward direction) and a Bronsted acid in Eq. (1.2) (forward direction).

The acidity constants for the above are:

$$\mathrm{K_1} = \frac{[\mathrm{MOH_{surf}}][\mathrm{H^+}]}{[\mathrm{MOH_{2\ surf}^+}]} \tag{1.3}$$

and:

$$\mathrm{K_2} = \frac{[\mathrm{MO^-{}_{surf}}][\mathrm{H^+}]}{[\mathrm{MOH_{surf}}]} \tag{1.4}$$

At the isoelectric point, $[\mathrm{MO^-{}_{surf}}] = [\mathrm{MOH_2{}^+{}_{surf}}]$, so that Eqs. (1.3) and (1.4) combine to give:

$$\mathrm{pH_{pzc}} = \frac{\mathrm{pK_1} + \mathrm{pK_2}}{2} \tag{1.5}$$

where $pK_i = -\log K_i$ and pH_{pzc} is the isoelectric point. Differences in the surface acidities of various surface hydroxyls MOH depend on the nature of the metallic cation M, similar to the way that the identity of an organic radical R influences the behavior of organic alcohols, ROH.

Nature of Acidic and Basic Surface Sites

A broader view of acids and bases has been given by G. N. Lewis, in which a Lewis acid is an electron acceptor and a Lewis base is an electron donor [5, 6]. This definition allows a wide variety of molecules, ions, and compounds to be classified as Lewis acids or Lewis bases. With this in mind, the following lists the types of acid sites on metal oxide surfaces. See also Fig. 1.2.

1. unhydroxylated metal ions, $M^{+\delta s}$
2. protonated surface hydroxyls, $-MOH_2{}^{+}{}_{surf}$

$$-MOH_2{}^{+}{}_{surf} \rightarrow -MOH_{surf} + H^{+}{}_{(aq)}$$

3. surface hydroxyls, $-MOH_{surf}$

$$-MOH_{surf} \rightarrow -MO^{-}{}_{surf} + H^{+}{}_{(aq)}$$

where δ_s is the partial charge on a metal surface ion. The first of these acid sites above is a Lewis acid because the metal ion $M^{+\delta s}$ can accept electrons [7, 8].

The basic sites [7, 8] on metal oxides are listed below. See also Fig. 1.3.

4. unhydroxylated oxygen anions, $O^{-\gamma s}$
5. dissociated surface hydroxyls, $-MO^{-}{}_{surf}$

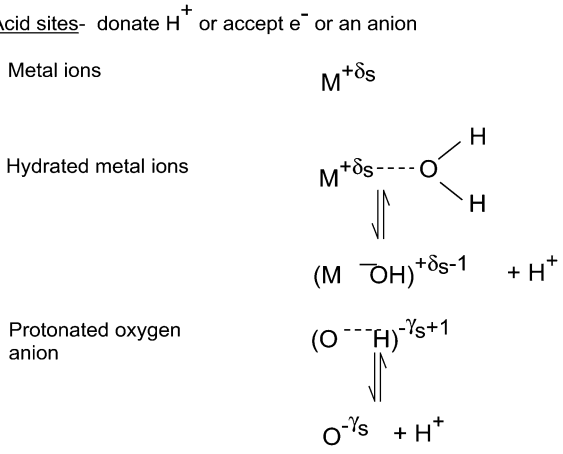

Fig. 1.2 Various types of acid sites in a metal oxide [8]. +δ refers to a partial charge on the metal cation and −γ to a partial charge on the oxygen ion

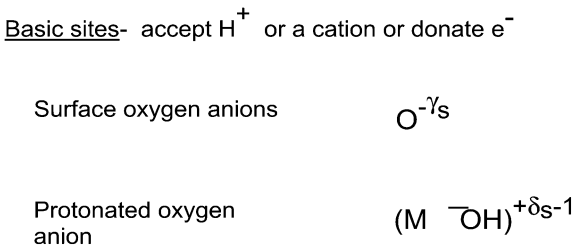

Fig. 1.3 Various types of basic sites in a metal oxide [8]. +δ refers to a partial charge on the metal cation and −γ to a partial charge on the oxygen ion

$$-\mathrm{MO}^{-}{}_{\mathrm{surf}} + \mathrm{H}^{+}{}_{(\mathrm{aq})} \rightarrow -\mathrm{MOH}_{\mathrm{surf}}$$

6. surface hydroxyls, $-\mathrm{MOH}_{\mathrm{surf}}$

$$-\mathrm{MOH}_{\mathrm{surf}} + \mathrm{H}^{+}{}_{(\mathrm{aq})} \rightarrow -\mathrm{MOH}_2{}^{+}{}_{\mathrm{surf}}$$

where γ_s is the partial charge on an surface oxygen anion. The first of these basic sites above is a Lewis base because the oxygen anion $O^{-\gamma_s}$ can be an electron donor.

While all these different types of acid or basic sites are possible, the acid-base properties of the oxide are usually dominated by the behavior of the hydroxyl groups.

Kaltchev and Tysoe [9] have used NH_3 (a Lewis base) to probe surface sites on thin oxide films on aluminum. Using infrared spectroscopy, these authors found that NH_3 adsorbed on both hydroxylated and dehydroxylated oxide surfaces. In a study on pure chromium, Ma et al. [10] found that the NH_3 molecule reacted with Cr^{+3} acid sites in the chromium oxide film formed in vacuum on Cr(100) but did not react with Cr^{+3} acid sites in the passive film on chromium. Ma et al. concluded that the acid-base properties of the passive film on chromium are dominated by the properties of the OH layer.

Determination of Isoelectric Points of Metal Oxides and Oxide Films

The isoelectric point of a bulk oxide or oxide film can be measured in several different ways. Several methods are discussed here. It should be noted that there have been many more experimental determinations for oxide powders than for intact oxide films on low-area flat sheets or foils.

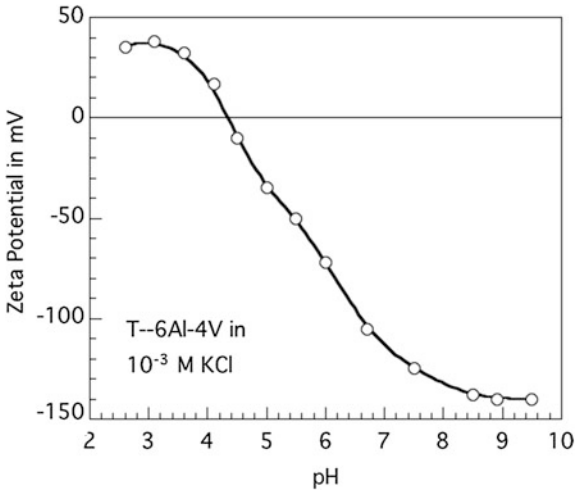

Fig. 1.4 The pH dependence of the zeta potential for the air formed oxide film on T-6Al-4V. Redrawn from Ref. [13] with the permission of Elsevier

Streaming Potential Measurement

One method of determining the isoelectric point of an oxide-covered metal is to measure the zeta potential, i.e., the potential drop across the diffuse part of the electrical double layer, as a function of the pH of the electrolyte. This can be done by streaming potential measurements [11–15] in which the aqueous phase is forced to flow across a fixed solid surface. The zeta potential goes through zero at the isoelectric point of the solid surface, as shown in Fig. 1.4. The basic idea is that the total charge at the metal/oxide/solution interface, σ_{total}, is the sum of the charge at the surface, $\sigma_{surface}$, plus that in the diffuse double layer, $\sigma_{diffuse}$:

$$\sigma_{total} = \sigma_{surface} + \sigma_{diffuse} \tag{1.6}$$

At the isoelectric point, $\sigma_{total} = 0$, so that when $\sigma_{diffuse}$ goes through 0, so does the surface charge $\sigma_{surface}$.

Contact Angle Measurements

Another method is to measure contact angles of aqueous droplets on the oxide-covered metal surface [16–19]. In this approach, contact angles are measured at the hexadecane/aqueous solution interface, as show in Fig. 1.5. The pH of the aqueous phase is varied, and the contact angle is observed to go through a maximum at the isoelectric point of the oxide film, as shown in Fig. 1.6.

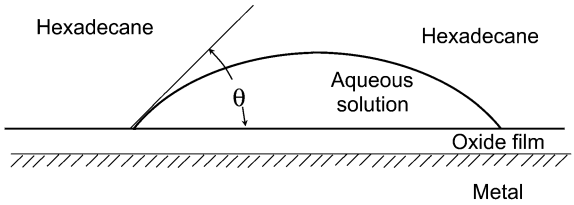

Fig. 1.5 Schematic diagram for a contact angle in the two liquid-solid system [17]

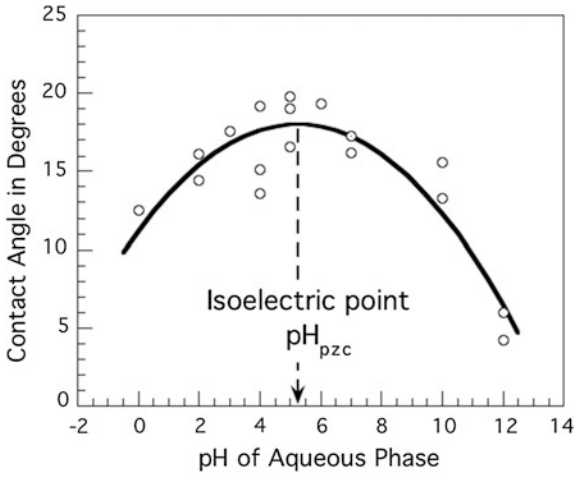

Fig. 1.6 Contact angles as measured by the goniometer technique for chromium-plated steel (Ferrotype) at the hexadecane/aqueous solution interface. Redrawn from Ref. [13] with the permission of Elsevier

The expression for the surface charge density σ at the oxide/solution interface is:

$$\sigma = z\,F\left(\Gamma_{H^+}^{S1} \quad -\Gamma_{O^-}^{S1}\right) \tag{1.7}$$

where F is the Faraday, z = 1 here, and Γ_i refers to surface excesses of H^+ or O^-. Use of Eq. (1.7) along with Young's equation for contact angles, and the Gibbs expression for surface thermodynamics leads to [16–18]:

$$\frac{d\cos\theta}{d\,pH} = \frac{1}{\gamma_{12}}\left[\frac{\sigma}{zF}\left(-2.303\,RT + zF\frac{d\psi}{d\,pH}\right) + \Gamma_{O^-}^{S1}\,zF\frac{d\psi}{d\,pH}\right] \tag{1.8}$$

At the isoelectric point, the surface charge density σ is zero and the surface concentration of dissociated hydroxyl groups $\Gamma_{O^-}{}^{S1}$ is also zero, so that Eq. (1.8) becomes:

$$\left(\frac{d\cos\theta}{d\,pH}\right)_{\sigma=0} = 0 \tag{1.9}$$

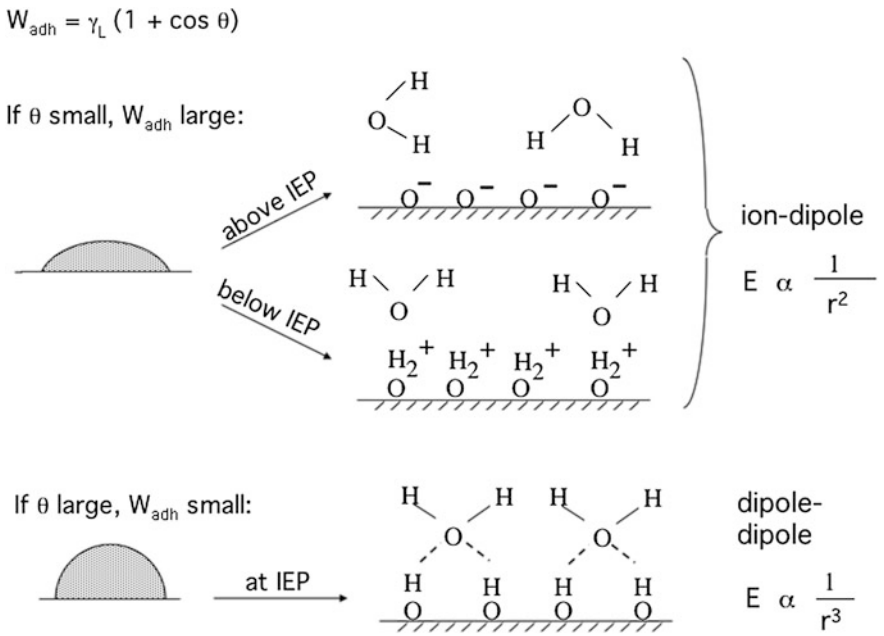

Fig. 1.7 Schematic diagram showing the interaction of a water molecule with an oxide film above, at, and below the isoelectric point (IEP) of the oxide. E is the energy of attraction, r is the distance of approach, and W_{adh} is the thermodynamic work of adhesion. Reproduced from Ref. [91] with the permission of Elsevier

At the isoelectric point, the cosine of the contact angle goes though a minimum and the contact angle through a maximum. Contact angles can be measured directly using an optical goniometer or indirectly using a Wilhemy balance.

This same conclusion can be reached independently by a qualitative argument shown in Fig. 1.7. The relationship between the contact angle and the thermodynamic work of adhesion W_{adh} is given by the Young-Dupré equation [20]:

$$W_{adh} = \gamma_L(1 + \cos\theta) \tag{1.10}$$

At the isoelectric point of the oxide film, the oxide surface consists of hydroxyl groups which can interact with water molecules by double hydrogen bonding, as shown in Fig. 1.7. These interactions are dipole-dipole interactions, for which the energy of attraction E is [21]:

$$E \propto \frac{1}{r^3} \tag{1.11}$$

where r is the distance of approach. Above the isoelectric point, water molecules interact with a negatively charged surface, while below the isoelectric point, water

molecules interact with a positively charged surface, as is also shown in Fig. 1.7. For these ion-dipole interactions, the energy E is given by [21]:

$$E \propto \frac{1}{r^2} \tag{1.12}$$

and thus are stronger than interactions at the isoelectric point.

When the energy of attraction is the highest (below and above the isoelectric point where the stronger ion-dipole interactions occur), then the work of adhesion W_{adh} has its highest values. Thus, cos θ also displays its highest values, but θ its lowest. By the same argument, at the isoelectric point where the oxide surface is hydroxlyated, the energy of interaction with water molecules is lowest (due to weaker dipole-dipole interactions). Thus W_{adh} and cos θ are also lowest, but θ has its highest value. Thus, the contact angle for aqueous solutions measured as a function of pH goes though a maximum at the isoelectric point of the oxide surface.

The contact angle method has been used experimentally to determine the isoelectric point of oxide films on silver [16], chromium, aluminum, and tantalum [17, 18], on an Al-5 % Mg alloy [22], and on aluminum, zinc, and copper [23].

Surface Reaction Method of Simmons and Beard

In this method, developed by Simmons and Beard [24], negatively charged surface groups $MO^-{}_{surf}$ are allowed to react with aqueous K^+ ions (a Lewis acid) and positively charged surface groups $MOH_2{}^+{}_{surf}$ are reacted with aqueous anions or amines (Lewis bases). The extent of the surface reaction is followed by X-ray photoelectron spectroscopy (XPS) or some other suitable surface analysis technique.

Above the isoelectric point, the predominant surface species is $MO^-{}_{surf}$, as in Eq. (1.2). When $MO^-{}_{surf}$, surface groups interact with dissolved K^+ ions, then:

$$MO^-{}_{surf} + K^+{}_{(aq)} \rightleftharpoons MO^-K^+{}_{surf} \tag{1.13}$$

After reaction with K^+ ions, the various types of surface sites are given by:

$$[MOH_{surf}] + [MO^-{}_{surf}] + [MO^-K^+{}_{surf}] = N_o \tag{1.14}$$

The surface concentration of unreacted negatively charged sites $MO^-{}_{surf}$ is negligible for excess K^+, so that Eq. (1.14) becomes:

$$[MOH_{surf}] + [MO^-K^+{}_{surf}] = N_o \tag{1.15}$$

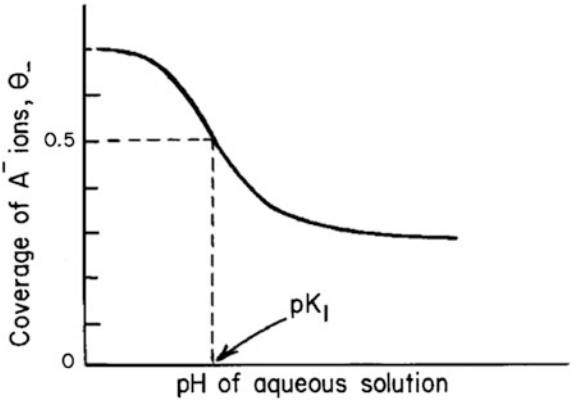

Fig. 1.8 Schematic diagram showing determination of the oxide acidity constant pK_1 from a plot of the surface coverage of adsorbed anions versus the pH of the solution

Use of $[MO^-{}_{surf}] = [MO^-K^+{}_{surf}]$ along with Eq. (1.15) in Eq. (1.4) gives:

$$pK_2 = pH - \log\left(\frac{\theta_+}{1-\theta_+}\right) \tag{1.16}$$

where $\theta_+ = [MO^-K^+{}_{surf}]/N_o$. Equation (1.16) has the form shown in Fig. 1.8. The surface equilibrium constant K_2 is determined from Eq. (1.16) and the pH where $\theta_+ = 0.5$.

Below the isoelectric point, the predominant surface species is $MOH_2{}^+{}_{surf}$, as in Eq. (1.1). When $MOH_2{}^+{}_{surf}$ surface groups interact with dissolved anions A^- (Lewis bases), then:

$$MOH_2{}^+{}_{surf} + A^-{}_{(aq)} \rightleftharpoons MOH_2{}^+A^-{}_{surf} \tag{1.17}$$

Considerations similar to those for the case of the negatively charged surface gives the result:

$$pK_1 = pH + \log\left(\frac{\theta_-}{1-\theta_-}\right) \tag{1.18}$$

where $\theta_- = [MOH^+{}_2A^-{}_{surf}]/N_o$ and is the fractional coverage of reacted $MOH_2{}^+{}_{surf}$ sites. Equation (1.18) has the form shown in Fig. 1.9. The surface equilibrium constant K_2 is determined from Eq. (1.18) and from the pH where $\theta_- = 0.5$.

In this manner, Simmons and Beard determined $pK_1 = 8.5$ and $pK_2 = 11.5$ for oxide-covered flat surfaces of iron. Thus, the isoelectric point is $pH_{pzc} = 10.0$ by Eq. (1.5). This method has also been used by Watts and Gibson [25] who exchanged surface hydroxyls on the oxide-covered iron surface with either K^+ cations or phosphate anions and determined $pK_1 = 8.4$, $pK_2 = 11.5$, and $pH_{pzc} = 10.0$, in excellent agreement with the results of Simmons and Beard.

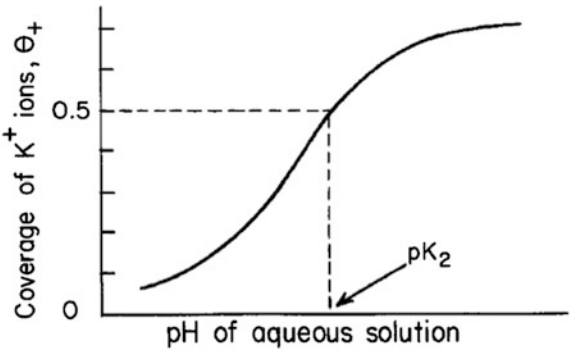

Fig. 1.9 Schematic diagram showing determination of the oxide acidity constant pK_2 from a plot of the surface coverage of adsorbed cations versus the pH of the solution

Ionic Interaction Model of Parks [26]

This model provides a way to correlate the isoelectric points of various oxides (or oxide films) rather than experimental determination of their values. However, the isoelectric point of an oxide not yet determined experimentally can be estimated from this correlation.

The equilibrium between positively and negatively charged surface groups in the hydroxylated layer is:

$$-\mathrm{MO^-}_{\mathrm{surf}} + 2\ \mathrm{H^+}_{(\mathrm{aq})} \rightleftharpoons -\mathrm{MOH_2}^+_{\mathrm{surf}} \tag{1.19}$$

which combines Eqs. (1.1) and (1.2). The equilibrium constant for Eq. (1.19) is:

$$\mathrm{K} = \frac{[\mathrm{MOH_2}^+_{\mathrm{surf}}]}{[\mathrm{MO^-}_{\mathrm{surf}}][\mathrm{H^+}]^2} \tag{1.20}$$

and the free energy change for Eq. (1.19) is:

$$\Delta \mathrm{G} = -2.303\ \mathrm{RT}\ \log \mathrm{K} \tag{1.21}$$

At the isoelectric point, $[-\mathrm{MO^-}_{\mathrm{surf}}] = [-\mathrm{MOH_2}^+_{\mathrm{surf}}]$ and $\mathrm{pH} = \mathrm{pH}_{\mathrm{pzc}}$. Under these conditions, Eqs. (1.20) and (1.21) combine to give:

$$\Delta \mathrm{G} = -2.303\left(2\ \mathrm{pH}_{\mathrm{pzc}}\right) \tag{1.22}$$

The free energy change can also be calculated from the various surface interactions operative in Fig. 1.10. The surface free energy change consists of contributions from three terms:

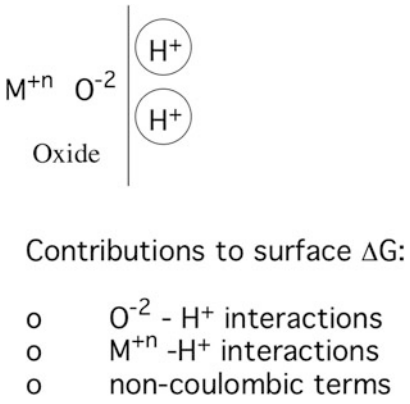

Fig. 1.10 Interaction of protons with an oxide surface in the ionic interaction model of Parks [26]

$$\Delta G = \Delta G\ (\text{non-coulombic}) + \Delta G\ \left(O^{-2} - H^{+}\ \text{interactions}\right) + \Delta G\ (M^{+n} - H^{+}\ \text{interactions}) \tag{1.23}$$

The first two terms in Eq. (1.23) may be combined into a constant A′ because they do not depend on the nature of the metallic cation. Thus,

$$\Delta G = A' - \frac{2\, z_H^{+}\, z_M^{+n}}{\varepsilon[2r(O^{-2}) + r(M^{+n}) + r(H^{+})]} \tag{1.24}$$

where z is the charge on the proton $(z_H{}^{+})$ or on the metallic cation $(z_M{}^{+n})$, ε is the local dielectric constant, and r_i are the various ionic radii. With the proton radius negligible compared to $2r(O^{-2})$ + $r(M^{+n})$, Eqs. (1.22) and (1.24) combine to give:

$$pH_{pzc} = A + \frac{Bz_M^{+n}}{R} \tag{1.25}$$

where A is a constant,

$$B = \frac{2\, z_H^{+}}{2.303RT\ \varepsilon} = \text{const} \tag{1.26}$$

and:

$$R = 2r\left(O^{-2}\right) + r(M^{+n}) \tag{1.27}$$

Thus, a plot of the isoelectric point versus $z(M^{+n})/\left[2r\left(O^{-2}\right) + r(M^{+n})\right]$ is expected to yield a straight line. Figure 1.11 shows such a plot for various bulk oxides or oxide films of elemental metals taken from Table 1.1. Ionic radii are from Shannon and Prewitt [27]. There is considerable scatter in Fig. 1.11, but the approach allows estimation of unknown isoelectric points. For example, for Li_2O,

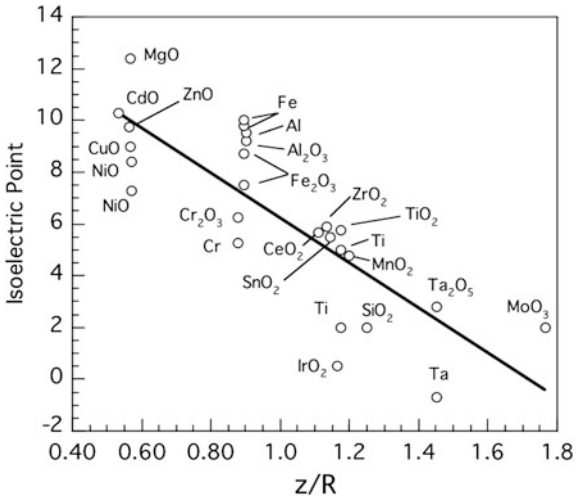

Fig. 1.11 A Parks-type plot of the isoelectric point of various oxides versus the quantity Z/R, where Z is the charge on the metal cation of the oxide and R is twice the radius of the oxygen anion plus the radius of the metal cation in the oxide. Isoelectric points are taken from Table 1.1

$z(Li^+)/\left[2r\left(O^{-2}\right) + r(Li^+)\right] = 0.282$, from which the isoelectric point of Li_2O is calculated to be 13.0.

XPS Correlation Method

Delamar [28] has shown that for metal oxides there is a direct correlation between XPS shifts and the isoelectric point of the oxide. The idea behind this correlation is that a lower binding energy for a surface species means that the species is able to release (i.e., donate) electrons more easily than for a higher binding energy species. Thus, a lower binding energy corresponds to a better Lewis base [29].

Delamar [28] defined the following quantity involving the XPS O 1s photopeak:

$$\Delta O = \text{O 1s binding energy} - 530 \tag{1.28}$$

Delamar noted that most basic oxides display an O 1s binding energy of approximately 530 eV, so that ΔO is a measure of the basicity (or acidity) of the surface oxide. Thus, when ΔO is small, the oxide is basic, and the isoelectric point, pH_{pzc}, should increase in numerical value.

Delamar also proposed that the acidities (or basicities) of metal cations can be compared by considering the chemical shift between the zero-valent metal and the cation. Delamar thus defined a second quantity:

$$\Delta M = \text{cation binding energy} - \text{metal binding energy} \tag{1.29}$$

as shown in Fig. 1.12.

Table 1.1 Isoelectric points of some oxides and oxide films

Oxide	Isoelectric point	References
Oxide film on Ta	−0.7	McCafferty and Wightman [17]
IrO_2	0.5	Ardizzone and Trasatti [40]
MoO_3	1.8–2.1	Compiled by Natishan [41]
SiO_2	1.8–2.2	Compiled by Natishan [41]
Ta_2O_5	2.8	Compiled by Natishan [41]
Oxide film on 304 stainless steel	3–4.8	Boulangé-Petermann [15]
Oxide film on 316 stainless steel	4.2–5.2	Kallay et al. [42]
MnO_2	4.7–4.8	Tamura et al. [43]
Oxide film on Ti	2	Kallay et al. [44]
	5.0	McCafferty et al. [31, 32]
	4.4	Roessler et al. [13]
Oxide film on Ti-6Al-4 V	4.4	Roessler et al. [13]
TiO_2	5.0–6.5	Ardizzone and Trasatti [40]
	5.5	Hu et al. [33]
SnO_2	5–6	Arai et al. [45]
Oxide film on Cr	5.2–5.3	McCafferty and Wightman [17]
CeO_2	5.2–6.1	Hsu et al. [46]
	6.7	Ozawa and Hattori [47]
ZrO_2	5.5–6.3	Compiled by Natishan [41]
	5.7–6.1	Mao et al. [48]
Oxidized Zr	6.7	Chvedov and Logan [23]
Cr_2O_3	6.2–6.3	Compiled by Natishan [41]
NiO	7.3	Moriwaki et al. [49]
	8.2–8.6	Kokarev et al. [50]
Fe_2O_3	7.5	Yates and Healy [51]
		Morowaki et al. [49]
	8.7	Smith and Salman [52]
Y_2O_3	8.3	Ozawa and Hattori [47]
CuO	8.5–9.5	Compiled by Kosmulski [53]
Oxidized Cu	9.3	Chvedov and Logan [23]
Al_2O_3	9.0–9.4	Compiled by Natishan [41]
Oxide film on Al	9.5	McCafferty and Wightman [17]
ZnO	9.2–10.3	Compiled by Natishan [41]
Oxidized Zn	9.3	Chvedov and Logan [23]
Oxide film on iron	9.8	Kurbatov [30]
	10.0	Simmons and Beard [24]
CdO	10.3	Janusz [54]
Oxide film on silver	10.4	Chau and Porter [16]
MgO	12.4	Compiled by Natishan [41]

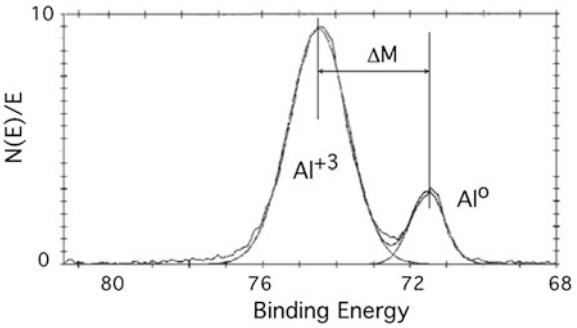

Fig. 1.12 XPS photopeak for Al $2p_{3/2}$ showing the quantity ΔM. From Ref. [17] by permission of Elsevier

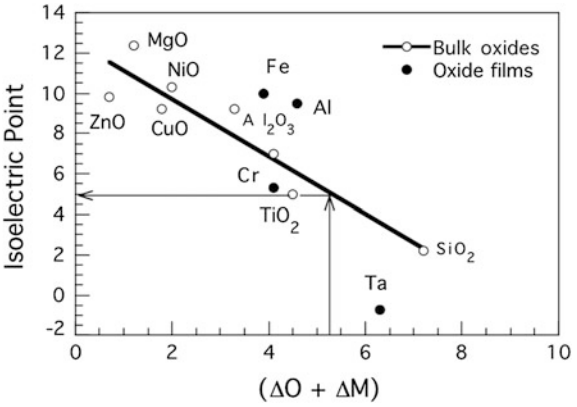

Fig. 1.13 Isoelectric points of several bulk oxides or oxide films as a function of the quantity (ΔO + ΔM) Reproduced from Ref. [31, 32] with permission of ECS—The Electrochemical Society

By arguments given above, small values of ΔM also correspond to Lewis bases. Delamar showed that there is linear correlation between the sum (ΔO + ΔM) and the isoelectric point pH_{pzc} of various bulk oxides. See Fig. 1.13. To the data for Delamar in Fig. 1.13 has been added data for several oxide-covered metals [17, 30]. The data for oxide-covered metals in Fig. 1.13 display some scatter around the data for bulk metal oxides, but the trend is the same for both bulk oxides and oxide films.

Thus, Fig. 1.13 can be used to estimate the isoelectric points of various oxide covered metals from XPS data. As an example, from a previous XPS study on metal oxide films [4, 31, 32], the quantity (ΔO + ΔM) has been determined to be 5.3 for oxide-covered titanium. Figure 1.13 gives the isoelectric point of the oxide film on titanium to be estimated as 5.0. This result is in excellent agreement with the value of 5.7 for bulk TiO_2 determined by Hu et al. [33] from measurements using the atomic force microscope and with the value of 5.6 for bulk TiO_2 determined by Larson et al. [34] from electrophoretic mobility measurements.

A correlation between the XPS quantity (ΔO + ΔM) and the isoelectric point of varous oxides has also been observed by Cattania et al. [35].

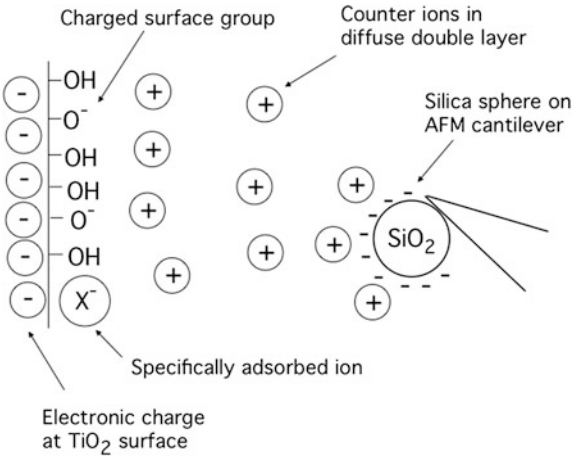

Fig. 1.14 Schematic representation of AFM force measurement between a negatively charged silica sphere and a TiO_2 substrate in an aqueous solution. Redrawn from Hu et al. [33] with the permission of the American Chemical Society

Measurement of Near-Surface Forces

A more recent method of determining the isoelectric point of an oxide or oxide film involves measurements with an atomic force microscope (AFM). Hu et al. [33] measured the force between a spherical probe placed at the end of an AFM cantilever and a flat TiO_2 substrate, as shown in Fig. 1.14. The charge within the diffuse double layer is calculated from the force between the electrode and the tip of the AFM cantilever. At the isoelectric point, the charge on the diffuse double layer is zero, and the net surface charge is zero. Similar studies have been carried out on TiO_2 [36], SiO_2 [37], Al_2O_3 [38], and oxide-covered tungsten [39].

Numerical Values of Isoelectric Points

Table 1.1 lists the isoelectric points for various bulk oxides and oxide films. The isoelectric point is a function of the identity of the individual cation in the M–OH bond. Oxides with an isoelectric point less than 7 are acidic oxides, and oxides with an isoelectric point greater than are basic oxides. It can be seen that there is a wide range in the values for oxide-covered metals. For instance, tantalum which is a passive metal has an oxide which is acidic, and aluminum, which is used in many applications in neutral solutions has an oxide which is basic. Much more data are available on bulk oxides than on intact oxide films, but in general, the isoelectric point of an oxide film is similar to that for the stand-alone bulk oxide.

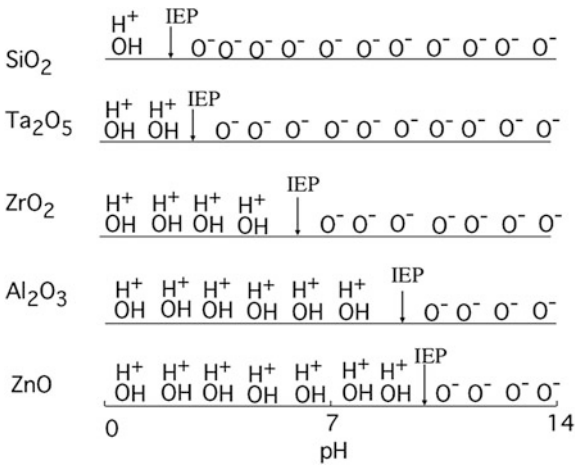

Fig. 1.15 Surface charge character of several oxide films. "IEP" refers to the isoelectric point of the oxide film

Surface Charge of Oxide Films

Figure 1.15 illustrates the surface charge character of several different oxides. As seen in Table 1.1, the isoelectric point of an oxide-covered aluminum surface is 9.5. Thus, in a solution of pH 7, the surface of aluminum oxide (and oxide-covered aluminum) consists of acidic groups (positively charged = $AlOH_2^+$). That is, in an aqueous solution of pH 7, the oxide film has a positively charged surface, as in Fig. 1.15 and Eq. (1.1). If the pH of the aqueous solution is greater than 9.5, then the oxide surface will be negatively charged, as per Fig. 1.15 and Eq. (1.2).

For some oxides in solutions of pH 7, such as tantalum oxide, the surface consists predominantly of basic groups (negatively charged TaO^-), as in Fig. 1.15. Oxide films on tantalum will have a positively charged surface only in acidic solutions where the pH is below the value of the isoelectric point.

Pitting of Aluminum

Most passive metals are subject to pitting corrosion. Pitting is a highly localized breakdown of the passive film caused by the presence of an "aggressive" anion in the electrolyte, usually Cl^- ions. However, pitting of various meals or alloys has also occurred in the presence of other anions, including Br^-, I^-, SO_4^{-2}, or NO_3^- [55].

The chloride ion has a special importance in pitting corrosion for several reasons. First of all, Cl^- ions are abundant, being constituents of seawater, brackish waters, de-icing salts, and of airborne salts. In addition, chlorides are found in the human body so they can cause the pitting of biomedical implants. Chlorides are also common contaminants in various electronic systems due to handling and processing.

The chloride ion is a strong Lewis base (electron donor) and tends to interact with Lewis acids (electron acceptors), such as metal cations. In addition, the chloride ion is a relatively small anion and has a high diffusivity.

Adsorption of Cl^- on Aluminum

The first step in the pitting process is the adsorption of chloride on the oxide-covered surface.

For an oxide-covered surface of aluminum immersed in a neutral solution, the aluminum oxide surface will be positively charged, as discussed above. This situation will favor the adsorption of the negatively charged Cl^- ions onto the positively charged oxide surface comprised predominantly of $= AlOH_2^+$ groups. The attractive forces which result when an anion, such as chloride, interacts with an ionic surface, such as an oxide, consist of (i) coulombic forces, (ii) induction of the adsorbent by the approaching ion, (iii) electrostatic polarization of the ion, and (iv) non-polar van der Waals forces [56].

Of these attractive forces, the largest are the first two interactions, which are ionic, as shown in Table 1.2. Thus, adsorption of chloride ions is most favored on a positively charged oxide surface for which the ion-ion forces are attractive in nature. When the oxide surface is negatively charged, ion-ion forces are not attractive in nature so that adsorption of Cl^- onto the negatively charged oxide surface is much less favored, but can proceed through the operation of van der Waals (dispersion) forces.

The above trends are also consistent with acid-base considerations. The negatively charged Cl^- anion is a Lewis base (electron donor) and the $= AlOH_2^+$ surface group is a Lewis acid (also a Bronsted acid), so interaction between these two reactants is favored. However, adsorption of the Lewis base Cl^- would not be favored on the Lewis base surface species, $= AlO^-$, which is the predominant surface species for pH values above the isoelectric point.

XPS studies have confirmed that the amount of chloride taken up by the passive film on aluminum varies with solution pH. Kolics et al. [57] observed that the minimum concentration of surface chloride occurred at a pH of about 9.5, i.e., at the isoelectric point, where the surface has a net charge of zero. Moreover, the amount

Table 1.2 Forces involved in the interaction of an anion with an oxide surface. From Ref. [56]

Type of interaction	Distance dependence of energy of interaction
Coulombic	$1/r$
Electrostatic induction of substrate by ion	$1/r^4$
van der Waals (dispersion)	$1/r^6$
Electrostatic polarization the ion	Usually small. Calculated from the polarizability of the ion and the electrostatic field of the adsorbent

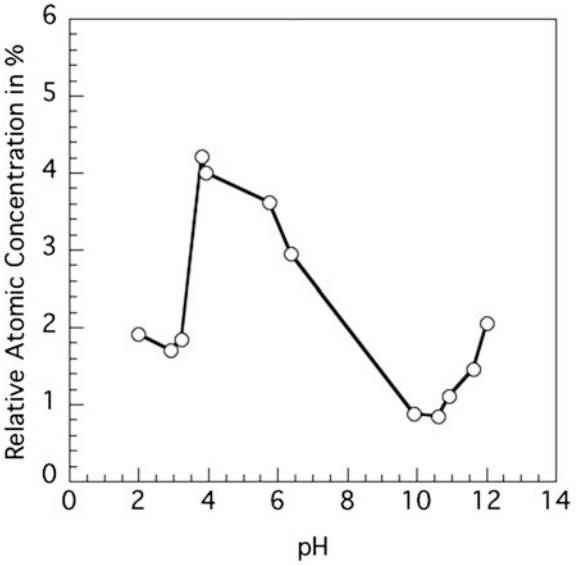

Fig. 1.16 Chloride content in the oxide film on aluminum as a function of pH after immersion in a 0.1 M solution of NaCl. Redrawn from Kolics et al. [57] with the permission of ECS—The Electrochemical Society

of adsorbed chloride increased with decreasing pH, in agreement with the above discussion. See Fig. 1.16. A similar observation has been reported for the adsorption of Cl^- on bulk aluminum oxide [58].

Electrode Kinetics of Pit Initiation on Aluminum

The first step in the pitting process of any metal in chloride-containing solutions is the adsorption of Cl^- ions on the oxide-covered metal surface.

In the case of aluminum, the isoelectric point of the oxide-covered aluminum surface is 9.5. Thus, when aluminum is used in neutral or nearly neutral solutions (the usual case), there is a positive charge on the oxide surface. This situation is favorable for adsorption of Cl^- ions on the oxide film on aluminum, as has been discussed above. Subsequent steps in the pitting process involve transport of chloride through the oxide film and local dissolution of aluminum atoms at the metal/oxide interface. See Fig. 1.17. Experimental evidence supporting this sequence of events has been given elsewhere [59], and more detail on the interaction of Cl^- ions with passive films is discussed later in this volume.

The following sequence of reactions [60] leading to pit initiation takes into account adsorption of chloride ions, transport of chloride ions through the oxide film by means of oxygen vacancies, and local dissolution of aluminum atoms at the metal/oxide interface in three consecutive one-electron transfer reactions:

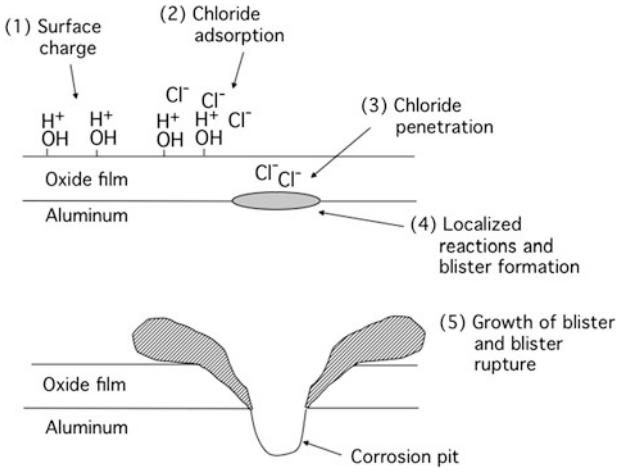

Fig. 1.17 Sequence of steps in the pitting of aluminum by chloride ions

$$\mathrm{Al(oxide)OH} + \mathrm{H^+} \underset{-1}{\overset{1}{\rightleftharpoons}} \mathrm{Al(oxide)OH_2^+} \tag{1.30}$$

$$\mathrm{Al(oxide)OH_2^+} + \mathrm{nCl^-} \underset{-2}{\overset{2}{\rightleftharpoons}} \mathrm{Al(oxide)OH_2{}^+Cl_n{}^{-n}} \tag{1.31}$$

$$\mathrm{Al(oxide)OH_2{}^+Cl_n{}^{-n}} + \mathrm{nV_{O^{\cdot}}} \underset{-3}{\overset{3}{\rightleftharpoons}} \mathrm{Al[(nCl_{O^{\cdot}})(oxide)]OH_2^+} \tag{1.32}$$

$$\mathrm{Al[(nCl_{O^{\cdot}})(oxide)]OH_2^+} \underset{-4}{\overset{4}{\rightleftharpoons}} \mathrm{Al^+[(nCl_{O^{\cdot}})(oxide)]OH_2^+ + e^-} \tag{1.33}$$

$$\mathrm{Al^+[(nCl_{O^{\cdot}})(oxide)]OH_2^+} \underset{-5}{\overset{5}{\rightleftharpoons}} \mathrm{Al^{++}[(nCl_{O^{\cdot}})(oxide)]OH_2^+ + e^-} \tag{1.34}$$

$$\mathrm{Al^{++}[(nCl_{O^{\cdot}})(oxide)]OH_2^+} \xrightarrow{6} \underset{\text{(at site of pit)}}{\mathrm{Al^{+++}[(mCl_{O^{\cdot}})(oxide)]OH_2^+}} + \mathrm{(n-m)Cl^-} + \mathrm{e^-} \tag{1.35}$$

In the notation Al(oxide)OH, Al refers to a substrate aluminum metal atom located immediately beneath the oxide film. "Oxide" refers to the oxide film covering that aluminum atom, Al, which will eventually undergo localized dissolution, i.e., pitting. Finally, in the notation Al(oxide)OH, OH refers to the outer layer of surface hydroxyl groups. In addition, $V_{O^{\cdot}}$ refers to an oxygen vacancy in the film, $Cl_{O^{\cdot}}$ is a chloride ion occupying an oxygen lattice site, and $Al[(nCl_{O^{\cdot}})(oxide)]OH_2^+$ refers to the oxide film on aluminum through which chloride ion transport is occurring. The symbol $Al[(nCl_{O^{\cdot}})(oxide)]OH_2^+$ represents zero valent aluminum metal existing prior to pit initiation in which the metal substrate is covered by its

chloride-containing oxide film. $Al^{+}[(nCl_{O^{\cdot}})(oxide)]OH_2^{+}$, $Al^{++}[(nCl_{O^{\cdot}})(oxide)]OH_2^{+}$, and $Al^{+++}[(mCl_{O^{\cdot}})(oxide)]OH_2^{+}$ respectively, refer to mono-, di-, and trivalent aluminum ions at the metal/oxide interface, i.e., at the site of the initiating pit.

As also discussed elsewhere [60], Eq. (1.31) allows that chloride clusters form on the oxide-covered surface and that the concentration of chloride ions in the oxide film decreases with the onset of pitting [61]. Thus, $0 < m < n$ in Eq. (1.35) allows that there is some expulsion of chloride from the film in the vicinity of the pit when pitting initiates. The electrolyte is provided by the presence of water in the passive film [62, 63].

The steady state solution for the anodic current density i_a due to Eqs. (1.30) through (1.35) is [60]:

$$\frac{i_a}{F} = 3\frac{k_2k_3k_4k_5k_6N_0[V_{O^{\cdot}}]^n}{k_{-2}k_{-3}k_{-4}k_{-5}}\left(\frac{[H^+]}{[H^+]+K_1}\right)[CI^-]^n \quad e^{5FE/2RT} \tag{1.36}$$

where F is the Faraday, k_i is the rate constant for the ith step, N_0 is the total number of surface sites (in moles/cm^2), $[V_O]$ is the concentration of oxygen vacancies in the film, $k_{-1}/k_1 = K_1$, the surface equilibrium constant in Eq. (1.30), and E is the electrode potential. The electrochemical transfer coefficient has been taken to be 1/2.

This expression, i.e., Equation (1.36), can be used to explain (i) the variation in pitting potential with pH (at fixed Cl^- concentration) and (ii) the variation in pitting potential with Cl^- concentration (at fixed pH).

Pitting Potential of Aluminum as a Function of PH

The pitting potential of aluminum is independent of pH for pH values between 4 and 8 [60, 64], as shown in Fig. 1.18. Over this pH range, the oxide-covered aluminum surface consists of $= AlOH_2^{+}$ groups, as discussed above, adsorption of Cl^- is favored, and pitting proceeds at the same critical electrode potential for each pH.

As also shown in Fig. 1.18, the pitting potential increases with pH for pH values at and above the isoelectric point (9.5). This is because Cl^- adsorption is less favored on either = AlOH, or $= AlO^-$ surface groups so that it is necessary to move the electrode potential to more positive values to first adsorb chloride ions and then to drive them into interior of the passive film [57, 59, 61, 65].

The experimental results shown in Fig. 1.18 can be explained by application of Eq. (1.36). Any small value of i_a above the background value for the passive film current (say $i_a = i_{crit}$) can be chosen to consistently mark the start of pitting. Thus, when $i_a = i_{crit}$, $E = E_{pit}$, the critical pitting potential.

For pH values well below the isoelectric point, $pH < pK_1$, $[H^+] > K_1$, so that $[H^+]/([H^+]+K_1) \cong 1$. Taking logarithms in Eq. (1.36) under these conditions and differentiating with respect to the pH at constant chloride concentration gives:

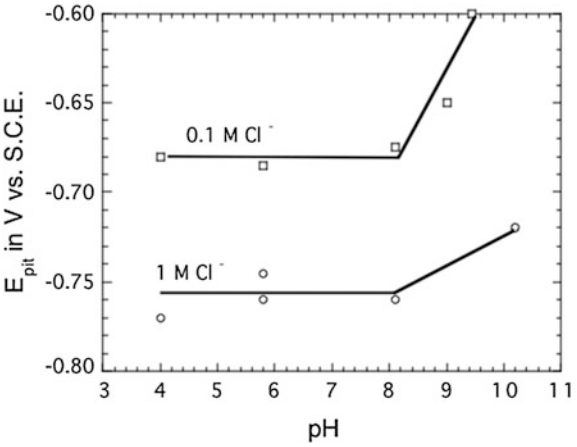

Fig. 1.18 Pitting potential of aluminum as a function of pH at two different fixed concentrations of chloride ion. From Ref. [60] by permission of Elsevier

$$\left(\frac{d\,E_{pit}}{d\,pH}\right)_{[Cl^-]} \cong 0 \tag{1.37}$$

in agreement with experiment.

For pH values above the isoelectric point, pH $>$ pK_1, $[H^+] < K_1$, so that $[H^+]/([H^+] + K_1) \cong ([H^+]/K_1$. Taking logarithms in Eq. (1.36) under these conditions and again differentiating with respect to the pH at constant chloride concentration now gives:

$$\left(\frac{d\,E_{pit}}{d\,pH}\right)_{[Cl^-]} = \frac{2}{5}\left(\frac{2.303\,RT}{F}\right) = \text{const} \tag{1.38}$$

Thus, above the isoelectric point, the pitting potential increases linearly with pH (at constant chloride ion concentration). Figure 1.18 shows that this predicted relationship holds, although Fig. 1.18 contains limited data points above the isoelectric point (due to the general corrosion of aluminum at higher pH values. The predicted value of dE_{pit}/dpH from Eq. (1.38) is 0.024 V, while experimental values from Fig. 1.18 are 0.053 V for 0.1 M Cl^- and 0.025 V for 1 M Cl^-.

Pitting Potential of Aluminum as a Function of Cl^- Concentration

Figure 1.19 shows experimentally determined pitting potentials for pure aluminum as a function of chloride ion activity (concentration) for chloride concentrations of 0.01–1.0 M [60]. It can be seen that the pitting potential varies linearly with the logarithm of the chloride concentration at constant pH.

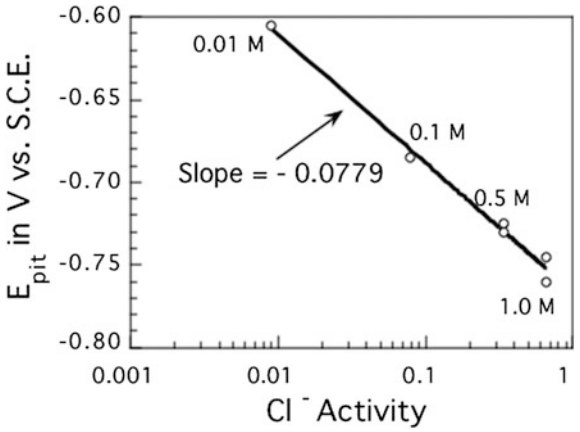

Fig. 1.19 Pitting potential of aluminum as a function of chloride ion concentrations at a fixed pH of 7. From Ref. [60] by permission of Elsevier

This behavior also follows from Eq. (1.36). Taking logarithms with respect to chloride ion concentration at constant pH gives:

$$\left(\frac{d\,E_{pit}}{d\log\left[Cl^{-}\right]}\right)_{pH} = -n\frac{2}{5}\left(\frac{2.303\,RT}{F}\right) = const' \tag{1.39}$$

The parameter n was evaluated from the variation in the steady-state anodic current at the pitting potential as a function of chloride ion concentration [60], with the result being n = 3.77. This average number of chloride ions n = 3.77 associated with a pitting site is within the range of values (2–8) as determined from induction times to pitting for aluminum and its alloys in various aqueous solutions [66, 67]. With n = 3.77, Eq. (1.39) becomes:

$$\left(\frac{d\,E_{pit}}{d\log\left[Cl^{-}\right]}\right)_{pH} = -0.0891 \tag{1.40}$$

in nominal agreement with the experimentally determined value of −0.0779, as shown in Fig. 1.19.

Experimental values for the variation in pitting potential of pure aluminum with the logarithm of the chloride concentration have been reported to range from −0.073 to −0.12 V [68–72], although Bockris and Minevski [73] report a much higher value of ca. −0.315 V. Equation (1.40) thus agrees with the experimental observation that the pitting potential varies linearly with the logarithm of the chloride concentration at constant pH. Variations in experimental values for $dE_{pit}/d\log[Cl^{-}]$ reported in the literature may be due to variations from system to system in the number n of chloride ions associated with a pit initiation site.

Thus, the dependence of the pitting potential on the chloride ion concentration or on the pH is described by the electrode kinetic mechanism considered here.

Acid-Base Interactions in Metal/Polymer Adhesion

Introduction

The adhesion properties of an organic coating and its corrosion performance are related. If corrosion occurs beneath the organic coating, a loss of adhesion of the coating will ensue. On the other hand, if the coating does not possess good adhesion to the metal substrate, then undermining of the coating will produce localized pockets of electrolyte which promote corrosion.

The relationship between adhesion and corrosion is seen schematically in Fig. 1.20.

Theories of Polymer Adhesion

There are several fundamental theories of metal/polymer adhesion. These are [74]:

1. The *adsorption theory* (physical and chemical adsorption), in which the adhesive bond depends on adsorption forces between the two interfaces being joined,
2. The *chemical reaction theory*, in which a chemical reaction occurs between the polymer and the metal,
3. The *mechanical interlocking theory*, in which adhesion is due to the mechanical interlocking or keying of the polymer into cavities and pores of the metal surface,

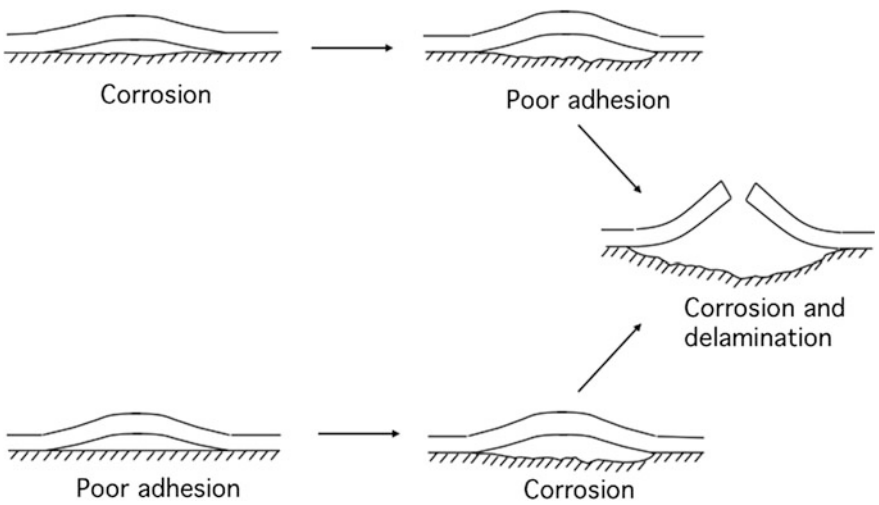

Fig. 1.20 Relationship between adhesion of an organic coating and corrosion of the metal substrate

4. The *electrostatic theory*, in which adhesion depends on the existence of an electrostatic charge between the two surfaces.

Each of these last three mechanisms can operate under certain conditions, but the most pervasive mechanism is the first, in which the polymer adheres to the metal substrate (or, more properly, to its oxide film) because of interatomic and intermolecular bonds which are formed. These adsorption forces that exist across all bonding interfaces include Lewis acid/Lewis base forces.

All metal surfaces to be coated with an organic polymer contain either the incipient air-formed oxide film or an oxide produced by a surface treatment (such as chromates or their replacements). Thus, it is appropriate to consider the interaction of organic polymers with oxide films.

Acid-Base Nature of Organic Polymers

As with oxide films, organic polymers can be also be classified as Lewis bases (electron donors) or Lewis acids (electron acceptors). For example, poly (methyl methacrylate) (PMMA) is a typical basic polymer, as can be reasoned from its molecular structure, as shown in Fig. 1.21. The carbonyl oxygens of esters are basic (electron-donating) sites, which can form acid/base bonds with electron-accepting sites of Lewis acids [75].

Poly(vinyl chloride) (PVC) is an example of a polymer which is a Lewis acid. For PVC, it is the partially positive -CH portion of the vinyl group which is the electron-accepting site and which can form acid/base bonds with electron-donating sites of Lewis bases [75]. See Fig. 1.22.

Fowkes and Mostafa [76] found that PMMA adsorbed strongly onto silica (an acidic oxide) but not onto calcium carbonate (a basic solid), whereas chlorinated-PVC (an acidic polymer) adsorbed onto calcium carbonate but not onto silica. Thus, Fowkes [77] reasoned that basic polymers adsorb only onto acidic solids and acidic polymers adsorb only onto basic solids. To carry this a step further, basic polymers should adsorb onto acidic oxide films and acidic polymers onto basic oxide films. In addition, the *practical* adhesion of basic polymers onto metals is expected to be the greatest on acidic oxide films. Similarly, the *practical* adhesion of acidic polymers

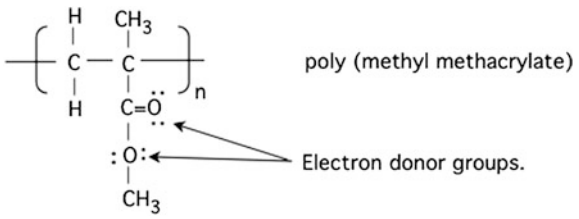

Fig. 1.21 An example of a basic polymer

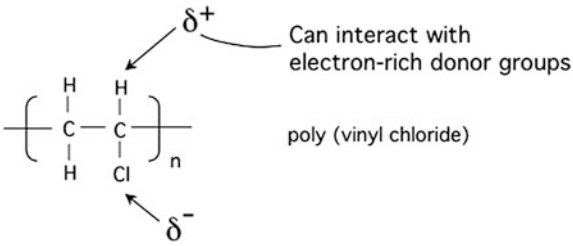

Fig. 1.22 An example of an acidic polymer

onto metals should be the greatest on basic oxide films. This is because a bond is formed in which electrons donated by the Lewis base are shared with the Lewis acid site.

Characterization of the Acid-Base Properties of Polymers

The acid-base properties of polymers can be determined by several techniques, including streaming potential measurements [78] (as in the case of oxide-covered metals), inverse gas chromatography [78, 79], and the contact angle method of van Oss and Good [80–83].

Inverse gas chromatography is a chromatographic technique in which the solid phase is of main interest rather than the gas phase, and hence the designation "inverse". This technique consists of measuring the retention times of various gases or vapors on a column packed with powders, fibers, or films of the polymer of interest. By using probing gases or vapors of known acid-base character, the acid-base nature of the polymer can be determined.

The contact angle method of van Oss and Good [80–83] uses various wetting liquids of various acid-base properties to probe the acid-base nature of the polymer to which they are applied.

This method extends the work of Fowkes [76], who wrote the surface free energy of a pure phase as the sum of several contributions:

$$\gamma = \gamma^{d} + \gamma^{i} + \gamma^{p} + \gamma^{h} + \cdots \tag{1.41}$$

where γ^{d} = van der Waals dispersion forces, γ^{i} = Debye induction forces (dipole-induced dipole), γ^{p} = Keesom dipole-dipole forces, and γ^{h} = the contribution due to hydrogen bonding. Equation (1.41) was rewritten by van Oss and Good [80–83] as:

$$\gamma = \gamma^{LW} + \gamma^{AB} \tag{1.42}$$

where $\gamma^{LW} = \gamma^{d} + \gamma^{i} + \gamma^{p}$ are called Lifshitz-van der Waals forces, and γ^{AB} are acid-base forces due to hydrogen bonding and all electron donor-electron acceptor

interactions. By using various combining rules across interfaces, van Oss and Good derived the expression:

$$(1+\cos\theta)\gamma_L = 2\sqrt{(\gamma_S^{LW}\gamma_L^{LW})} + 2\sqrt{(\gamma_S^{+}\gamma_L^{-})} + 2\sqrt{(\gamma_S^{-}\gamma_L^{+})} \tag{1.43}$$

where θ is the contact angle of a liquid on a solid surface, γ_L is the surface tension of the spreading liquid, and ${\gamma_L}^{LW}, {\gamma_L}^{+}$, and ${\gamma_L}^{-}$ are the Lifshitz-van der Waals, acid, and base contributions, respectively, to the total surface tension, γ_L. Similarly, ${\gamma_S}^{LW}, {\gamma_S}^{+}$, and ${\gamma_S}^{-}$ are the Lifshitz-van der Waals, acid, and base contributions, respectively, to the total surface free energy of the solid, γ_S. The quantities $\gamma_L, {\gamma_L}^{LW}, {\gamma_L}^{+}$, and ${\gamma_L}^{-}$ are known for a test set of standard wetting liquids. The terms ${\gamma_S}^{LW}, {\gamma_S}^{+}$, and ${\gamma_S}^{-}$ are the unknown quantities. Equation (1.43) is an equation in three unknowns: ${\gamma_S}^{LW}, {\gamma_S}^{+}$, and ${\gamma_S}^{-}$, as can be seen more clearly by rewriting Eq. (1.43) in matrix form:

$$\begin{bmatrix} (\gamma_{L1}^{LW})^{\frac{1}{2}} & (\gamma_{L1}^{-})^{\frac{1}{2}} & (\gamma_{L1}^{+})^{\frac{1}{2}} \\ (\gamma_{L2}^{LW})^{\frac{1}{2}} & (\gamma_{L2}^{-})^{\frac{1}{2}} & (\gamma_{L2}^{+})^{\frac{1}{2}} \\ (\gamma_{L3}^{LW})^{\frac{1}{2}} & (\gamma_{L3}^{-})^{\frac{1}{2}} & (\gamma_{L3}^{+})^{\frac{1}{2}} \end{bmatrix} \begin{bmatrix} (\gamma_S^{LW})^{\frac{1}{2}} \\ (\gamma_S^{+})^{\frac{1}{2}} \\ (\gamma_S^{-})^{\frac{1}{2}} \end{bmatrix} = \frac{1}{2} \begin{bmatrix} \gamma_{L1}(1+\cos\theta_1) \\ \gamma_{L2}(1+\cos\theta_2) \\ \gamma_{L3}(1+\cos\theta_3) \end{bmatrix} \tag{1.44}$$

where the numerical subscripts refer to the wetting liquid. Equation (1.44) can be written as:

$$AX = b \tag{1.45}$$

where A is the matrix containing the various surface tension parameters.

The first of the unknowns in Eq. (1.44), ${\gamma_S}^{LW}$, is determined by using a nonpolar liquid, such as methylene iodide, for which both ${\gamma_S}^{+}$ and ${\gamma_S}^{-}$ are zero and ${\gamma_L}^{LW} = \gamma_L$. Under these conditions, Eq. (1.44) reduces to:

$$\gamma_S^{LW} = \gamma_L \frac{(1+\cos\theta)^2}{4} \tag{1.46}$$

which allows evaluation of the parameter ${\gamma_S}^{LW}$ from the surface tension γ_L of methylene iodide and from the contact angle θ.

After this step, Eq. (1.44) then contains two unknowns ${\gamma_S}^{+}$ and ${\gamma_S}^{-}$. These unknowns are determined by using two different polar liquids and solving the resulting two equations simultaneously. One of the polar wetting liquids used is water and is taken pairwise in turn with formamide, ethylene glycol, or glycerol. These combinations of wetting liquids (plus methylene iodide) gave the best conditioned matrices A in Eq. (1.45). A matrix A is ill-conditioned if relatively small changes in the entries of A can cause relatively large changes in the solutions to Ax = b. The smaller the condition number, the more well-conditioned is the matrix. More detail has been given elsewhere [18].

The method of van Oss and Good has been used to determine the acid/base nature of the following polymers: poly(vinylchloride), poly(methylmethacrylate), poly(vinylacetate), and a commercial pressure sensitive adhesive (adhesive side). Table 1.3 lists the contact angle data and the resulting values of γ_S^{LW}, γ_S^+, and γ_S^- for the various polymers.

For any given polymer, there is some variation in the values of γ_S^+, andγ_S^-. As noted by Good and van Oss [82, 83], none of the solid surfaces display high values of γ_S^+, but the acidic polymer surfaces have higher values of γ_S^+ than do the basic polymer surfaces. The basic surfaces clearly have higher values of γ_S^- than do the acidic surfaces.

Comparison of the values of γ_S^+, and γ_S^- for the pressure sensitive adhesive with those for the acidic and basic polymers shows that pressure sensitive adhesive has an acidic surface.

A compilation of some acidic and basic polymers is given in Table 1.4.

Table 1.3 Surface free energy components (in mJ/m^2) for various polymers as determined by the method of van Oss and Good [18]

Water plus					
Polymer	Wetting liquid	θ	γ_S^{LW}	γ_S^+	γ_S^-
Poly(vinyl chloride) (Acidic)	Methylene iodide	38.8 ± 2.6	40.2	–	–
	Water	87.8 ± 4.2		–	–
	Formamide	69.2 ± 2.9		0.33	4.8
	Ethylene gylcol	64.7 ± 2.6		0.15	4.1
	Glycerol	84.2 ± 0.9		0.78	6.3
				0.42	5.1
Poly(methyl methacrylate) (Basic)	Methylene iodide	23.9 ± 0.8	46.5	–	–
	Water	64.3 ± 1.8		–	–
	Formamide	47.0 ± 1.8		0.00040	16.1
	Ethylene gylcol	47.1 ± 0.8		0.13	19.3
	Glycerol	64.3 ± 2.2		0.11	19.0
				0.080	18.1
Poly(vinyl acetate) (Basic)	Methylene iodide	33.8 ± 3.6	42.6	–	–
	Water	60.6 ± 2.9		–	–
	Formamide	46.2 ± 3.8		0.064	19.9
	Ethylene gylcol	47.1 ± 1.9		0.059	24.6
	Glycerol	61.6 ± 2.9		0.00082	22.5
				0.041	22.3
Pressure sensitive adhesive (Acidic)	Methylene iodide	90.2 ± 3.9	12.6	–	–
	Water	97.7 ± 5.3		–	–
	Formamide	97.6 ± 4.8		0.096	10.7
	Ethylene gylcol	82.3 ± 5.7		0.53	5.0
	Glycerol	108.0 ± 6.2		0.63	14.1
				0.42	9.9

Table 1.4 Some examples of acid, basic, or amphoteric polymers

Acidic polymers
Poly(vinyl chloride) [75]
Poly(vinyl fluoride) [75]
Poly(vinylidene fluoride) [75, 82]
Poly(vinyl butyral) [75]
Chlorosulfonated polyethylene [84]
Pressure sensitive adhesive composed of poly (acrylate-co-acrylic acid) [18, 85]
Polypropylene treated in an O_2 plasma [86]
Polycarboxylic acids [87]
Basic polymers
Poly (methyl methacrylate) [75, 82]
Poly (vinyl acetate) [18]
Polyethylene oxide [82]
Polyisoprene [84]
Polybutadiene [84]
Poly (styrene) [88]
Cellulose acetate [82]
Polypropylene treated in a N_2 plasma [86]
Poly (2-vinylpyridine) [87]
Amphoteric polymers
Rubber surfaces [84]
Poly (acrylic acid) [89]
Adhesive protein of common blue mussel [90]

Metal/Polymer Adhesion Tests

There have been but a few studies which show clearly the relationship between metal/polymer adhesion and the acid-base properties of the system. An experimental study by the author which involves two of the polymers characterized above is be discussed here [18, 91].

The adhesion of the pressure-sensitive adhesive (PSA) to various oxide-covered metal substrates was determined by measuring the peel force, as shown in Fig. 1.23. To minimize viscoelastic processes and to compare the interfacial adhesion for the various metal substrates, a moderately slow peel rate of 1.2 cm/min was used. The peel force was measured for a 1.91 cm (3/4 inch) wide strip of the pressure-sensitive adhesive on aluminum, chromium, tantalum, and zirconium for various contact times before the peel measurement. In each case, the metal sample was first cleaned in an argon plasma prior to application of the pressure-sensitive adhesive, which was rolled in place using a 5 pound (2.27 kg) cylindrical roller.

Figure 1.24 shows the peel force measured at 27 °C for the pressure-sensitive adhesive on various metal surfaces as a function of the surface isoelectric point of

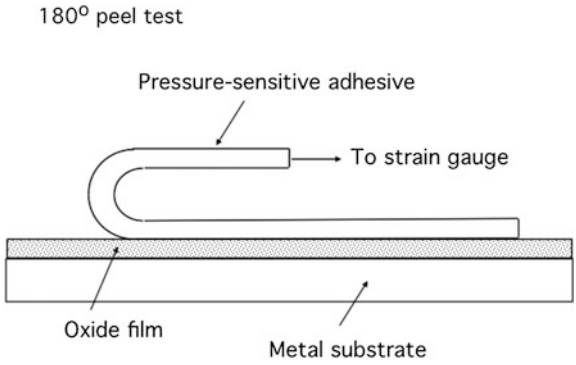

Fig. 1.23 Schematic diagram showing a 180° peel test for polymer adhesion

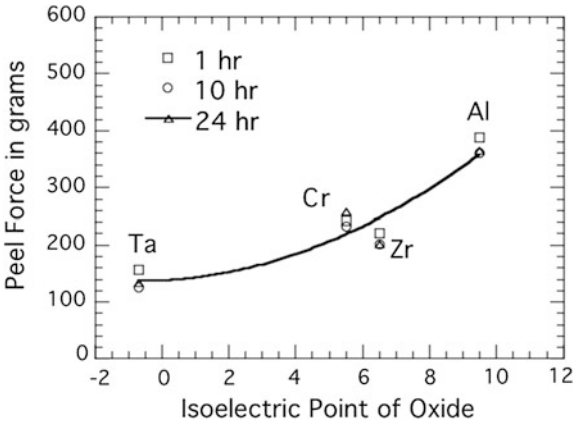

Fig. 1.24 Measured peel force for a pressure-sensitive adhesive (an acidic polymer) versus the isoelectric point of the oxide film. The peel force is shown for various contact times prior to the peel measurement [3, 18]. Reproduced by permission of Taylor and Francis

the oxide film. Figure 1.24 shows that the peel force for the acidic PSA increases with increasing basicity of the oxide film and is clearly the highest for the most basic oxide film, i.e., the oxide film on aluminum. This means that there is a greater ability for this basic oxide film to donate electrons to the acidic polymer. This increased acid-base interaction leads in turn to an increased practical adhesion.

The adhesion of a basic polymer, poly(methyl methacrylate), was measured by measuring the pull-off force from oxide-covered substrates of silicon, chromium, and aluminum. Experimental details have been given elsewhere [91], but in brief, metal samples were first solvent cleaned, films of poly(methyl methacrylate) were spin cast from chlorobenzene solutions to a thickness of nominally 1 μm in thickness, and 7.2 mm diameter aluminum studs were attached to the surface of the poly(methyl methacrylate) film using a commercial epoxy which was allowed to

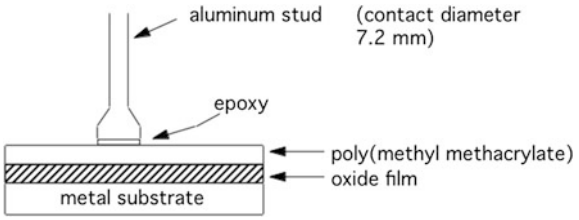

Fig. 1.25 Diagram of a pull-off test specimen showing an aluminum stud attached to a poly (methyl methacrylate) coating on an oxide-covered metal substrate [91]

cure for 2–3 days. Pull-off measurements were then made using a Romulus III stud pull tester at a loading rate of 1.5 N/s. The tester pulls the stud normal to the surface until the poly(methyl methacrylate) film is removed from the metal substrate at a critical force. See Fig. 1.25.

Figure 1.26 shows the measured pull-off force per unit area for the basic polymer PMMA for three different oxide-covered metal surfaces.

The measured pull-off force includes both interfacial and viscoelastic contributions, but because the polymer is the same for each metal surface, the viscoelastic contributions may be taken to be the same in each case. Thus, differences in the measured pull-off force may be ascribed to differences in interfacial adhesion. As seen in Fig. 1.26, the pull-off force for the basic polymer PMMA is highest for the most acidic oxide film. This means that there is a greater ability for this acidic oxide film to accept electrons from the electron-donating basic polymer. This increased acid-base interaction leads in turn to an increased practical adhesion.

In other related work, Chvedov and Logan [23] observed that the adhesion strength of two basic polymers on commercial grade aluminum decreased with the isoelectric point (i.e., with increasing basicity of the aluminum surfaces. The aluminum was given chromate-free pretreatments, which varied the isoelectric point. The adhesion strength was measured using a pull-tab test.

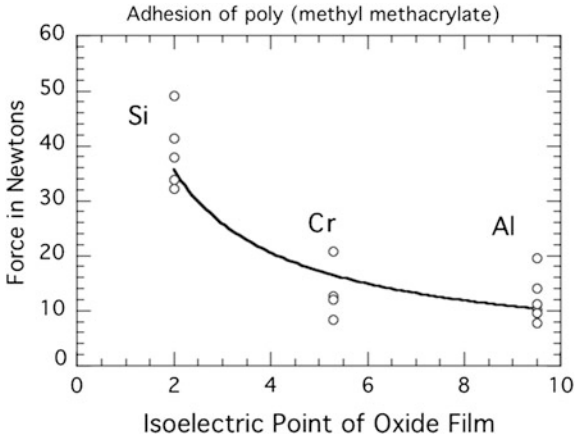

Fig. 1.26 Measured pull-off force for poly(methyl methacrylate (a basic polymer) versus the isoelectric point of the oxide film [3, 91]. Reproduced by permission of Taylor and Francis

Starostina et al. [92] found that the adhesion of an amine-modified polystyrene polymer increased with the relative acidity of the underlying oxide film on the metal substrate. The extent of adhesion was measured from cathodic delamination experiments in which the diameter of the delaminated defect was measured.

Thus, experimental results with either basic or acidic polymers on oxidized metals having various acid-base properties provide direct experimental evidence as to the importance of Lewis acid-Lewis base effects in the adhesion of polymers to oxide-covered metal surfaces.

Wet Adhesion

The situation becomes more complicated when water molecules accumulate beneath the organic coating because water interferes with the adhesion between the organic coating and the metal substrate. The extent of adhesion in the presence of a liquid (usually water) is referred to as *wet adhesion* and is considered by Funke [93] to be the most important property of the organic coating. Two different reasons have been proposed for the loss of adhesion in the presence of water [94, 95]. These are:

1. Chemical disbonding due to the interaction of water molecules with covalent, hydrogen, or polar bonds between the organic polymer and the oxide film,
2. Mechanical disbonding due to forces caused by accumulation of water and osmotic pressure.

At present the mechanisms of wet adhesion (and its loss) are not completely understood.

Acid-Base Effects in Corrosion Inhibition

In keeping with the theme of this chapter, corrosion inhibition will be considered for nearly neutral or basic aqueous solutions, in which the metal surface is covered with an oxide film. Acid solutions will not be considered because in acid solutions the metal surface generally does not contain an oxide film; and the inhibitor interacts with the metal surface without the intervening effect of the oxide film.

General Effect of Oxide Films

It is well known that organic inhibitors can adsorb strongly onto bare metal (i.e., oxide-free) surfaces, but corrosion inhibitors can also interact strongly with oxide films. Table 1.5 compares the heats of adsorption ΔH_{ads} for several small organic molecules onto the surfaces of metals, oxides, or oxide films. The heats of

Table 1.5 Heats of adsorption from the vapor phase at near-zero coverages for various small organic molecules or water on metals, oxides, or oxide-covered metal surfaces

Adsorbate	ΔH_{ads} on metal (kJ/mole)	ΔH_{ads} on metal oxide or oxide film (kJ/mole)	References
n-$C_3H_7NH_2$	−226 (on nickel)	−84 (on oxidized nickel)	Yu et al. [96]
	−105 (on copper)	−96 (on oxidized copper)	
n-C_3H_7OH	−347 (on nickel)	−138 (on oxidized nickel)	Yu et al. [96]
	−105 (on copper)	−67 (on oxidized copper)	
	–	−200 (on Al_2O_3)	Rossi et al. [97]
n-$C_3H_7NH_2$	−138 (on iron)	−188 (on oxidized iron)	Yu Yao [98]
n-$C_4H_9NH_2$	−144 (on iron)	−186 (on oxidized iron)	
n-$C_5H_{11}NH_2$	−165 (on iron)	−192 (on oxidized iron)	
n-$C_6H_{13}NH_2$	−172 (on iron)	−213 (on oxidized iron)	
(n-$C_3H_7)_2NH$	−128 (on iron)	−183 (on oxidized iron)	
$(C_2H_5)_3N$	−156 (on iron)	−207 (on oxidized iron)	
ϕ-CH_3*	–	−69 to −77 (on ZnO)	Nakazawa [99]
		−83 (on FeO)	
ϕ-OH*	–	−131 (on ZnO	Nakazawa [99]
		−140 (on FeO)	
H_2O		−113 (on oxidized iron)	Yu Yao [98, 100]
		−134 (on α-Fe_2O_3)	
		−134 (on α-Al_2O_3)	
		−80 to −90 (on NiO)	Matsuda [101]
D_2O		−89 (on ZnO)	Nakazawa [99]
		−65 (on FeO)	

*The symbol ϕ denotes the benzene ring

adsorption are from the vapor phase, so as to consider the energy of interaction between the adsorbate and the surface without the complicating effect of the solvent. The heats of adsorption in Table 1.5 are for near-zero coverages, so that values of ΔH_{ads} are those which pertain before ΔH_{ads} begins to decrease with increasing coverage. It can be seen that in some cases, the heats of adsorption onto the oxide or oxide-covered surface are well within the range expected for a chemisorptive process. This strong interaction is due to interaction of dipoles in the organic molecule with cations or anions present in the oxide surface. In addition, π-bonding is also possible between benzene rings and the metal oxide.

Because the metal surface is oxide-covered, the role of the inhibitor in neutral solutions is to make oxide films protective and to keep them so. Oxidizing inhibitors, like chromates, react with the oxide-covered surface and are incorporated into the passive film. With non-oxidizing inhibitors, however, such chemical reactions do not occur. Phosphates, for example, are incorporated into the passive film by exchange with surface oxide or hydroxide ions [102]. Other inhibitors, such as

sodium azelate are not taken up as uniformly, but instead function by repairing pores in oxide films by reacting there with dissolved cations to form insoluble local precipitates [103].

Mechanisms of Interaction with Oxide Films

There are two predominant mechanisms by which inhibitors can interact with oxide films. Both of these mechanisms involve Lewis acid-Lewis base effects:

1. Inhibitor molecules can react with hydroxylated species at the oxide surface, i.e., with $-MOH_{surf}$ at the isoelectric point, with $-MOH_2{}^{+}{}_{surf}$ below the isoelectric point, or with $-MO^{-}{}_{surf}$ above the isoelectric point.
2. The inhibitor can interact with metal cations M^{+n} located in the surface of the oxide film to form surface chelates, with the metal cation being the central ion of the chelate. Each cases is considered below.

Interaction of Inhibitors with Hydroxylated Oxide Films

The effect of the surface charge of the oxide film on corrosion inhibition can be illustrated by various examples.

The corrosion rate of zinc pigments in aqueous solutions containing phenolates inhibitors is higher at pH 10 than at pH 8 [104]. The authors attribute this difference to surface charge effects related to the isoelectric point of the oxide film on zinc surfaces. At pH values less than the isoelectric point of ZnO ($pH_{pzc} \approx 9$), the ZnO surface is positively charged so that more negatively charged phenolates can be adsorbed, lowering the corrosion rate. Above the isoelectric point of ZnO, the ZnO surface is negatively charged, and adsorption of phenolate ions is not favored. Similar results have been obtained [105] for the inhibition of aluminum by polymers with carboxyl groups, which are Lewis bases, i.e., electron donors. This effect is illustrated schematically in Fig. 1.27.

The interaction of oxide films with an aggressive ion, i.e., Cl^{-}, as a function of pH has been considered previously in this chapter.

Chelating Compounds as Corrosion Inhibitors

Chelating compounds are organic molecules with at least two polar functional groups capable of ring closure with a metal cation. The functional groups may either be basic groups, such as $-NH_2$, which can form bonds by electron donation,

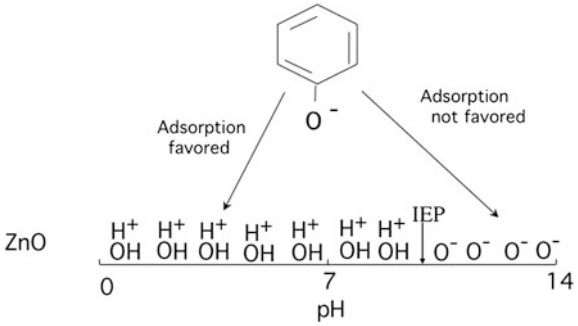

Fig. 1.27 Schematic representation of the adsorption of a negatively charged corrosion inhibitor as a function of the surface charge character of an oxide film

or acidic groups, such as −COOH, which can coordinate after the loss of a proton. An example of a surface chelate is shown in Fig. 1.28. The chelating molecule may interact with metal ions which exist in the oxide film, or they react with metal cations which are first produced by metallic dissolution. In the latter case, a complex of high molecular weight and low solubility is precipitated near the metal surface, and a barrier film is formed. Other chelating agents include mercaptoacetic acids, ethyene diaminetetraacetic acid, and catechols. See Fig. 1.29. In each case, surface chelates are formed involving bonding between a surface cation and an oxygen, sulfur, or nitrogen atom in the chelating molecule.

It is well known that in bulk solutions, 5-membered chelate rings are the most stable [106], and it appears that this effect carries over to surface chelates as well. There are steric requirements for surface chelates so that not all compounds which are capable of forming chelates in the bulk solution are effective corrosion inhibitors.

Chelating compounds have been studied as corrosion inhibitors for steel in industrial cooling waters [107, 108], and for zinc [109, 110] and aluminum [111, 112]

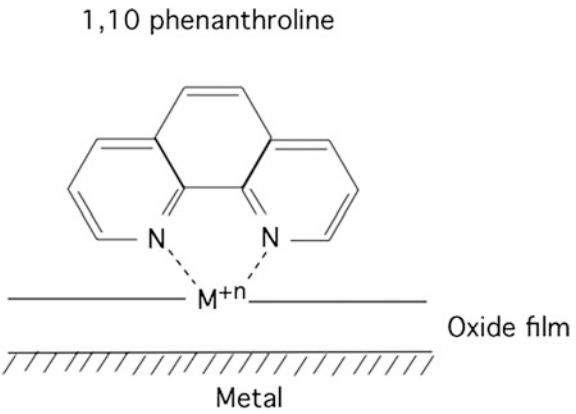

Fig. 1.28 A surface chelate formed between 1, 10 phenanthroline and the oxide film on a metal [107]

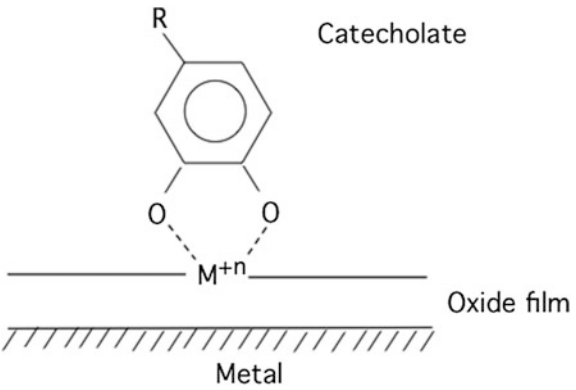

Fig. 1.29 A surface chelate formed between a catecholate and the oxide film on a metal

in various environments. The inhibition of the pitting of aluminum in chloride solutions was studied using substituted catechols [90]. A current interest in chelate inhibitors has been prompted by the search to replace chromate inhibitors with compounds which are less toxic and less polluting.

Hard and Soft Acids and Bases

Aramaki [7, 113–117] has given considerable attention to the study of corrosion inhibition in terms of hard and soft acids and bases. Hard and soft acids and bases (HSAB) are sub-sets of Lewis acids and bases. The designation "hard" refers to the situation where the valence electrons of a molecule or ion are attracted by the nucleus, and "soft" refers to the situation where the valence electrons are weakly attracted to the nucleus. See Table 1.6 for properties of hard and soft acids and bases and Table 1.7 for examples of common hard and soft acids and bases.

Aramaki [114, 117] explained passive film breakdown and repair by the HSAB principle. Aramaki noted that Fe^{+3} is a hard acid (Table 1.7) so that passive films containing Fe^{+3} ions are damaged by interaction with hard bases, such as Cl^-. The halide ions Br^- (a base of intermediate hardness) and l^- (a soft base) would be less

Table 1.6 Classification of hard and soft acids and bases

	Acid	Base
Hard	Electron cloud non-polarizable	Electron cloud non-polarizable
	Small size	Small size
	High positive charge	
Soft	Electron cloud more polarizable	Electron cloud more polarizable
	Large size	Large size
	Low positive charge	

Table 1.7 Examples of hard and soft acids and bases [118]

	Acids	Bases
Hard	H^+, Li^+, Na^+, K^+, Be^{+2}, Mg^{+2}, Ca^{+2}, Sr^{+2}, Mn^{+2}, Al^{+3}, Ga^{+3}, In^{+3}, La^{+3}, Cr^{+3}, Co^{+3}, Fe^{+3}, Si^{+4}, Ti^{+4}, Zr^{+4}, Th^{+4}, U^{+4}, $AlCl_3$, Cr^{+6}	H_2O, OH^-, F^-, $CH_3CO_2^-$, PO_4^{-3}, SO_4^{-2}, Cl^-, CO_3^{-2}, ClO_4^-, NO_3^-, ROH, RO^-, R_2O, NH_3, RH_2
Soft	Cu^+, Ag^+, Au^+, Tl^+, Hg^+, Pd^{+2}, Cd^{+2}, Pt^{+2}, Tl^{+3}, $GaCl_3$, I_2, Br_2, trinitrobenzene, quinones, CH_2, M^o (metal atoms)	R_2S, RSH, RS^-, I^-, SCN^-, $S_2O_3^{-2}$, CN^-, RNC, C_2H_4, C_6H_6
Intermediate	Fe^{+2}, Co^{+2}, Ni^{+2}, Cu^{+2}, Zn^{+2}, Pb^{+2}, Sn^{+2}, Sb^{+3}, Bi^{+3}, Rh^{+3}, Ir^{+3}, Ru^{+2}, Os^{+2}	$C_6H_5NH_2$, C_5H_5N, Br^-, NO_2^-, SO_3^{-2}

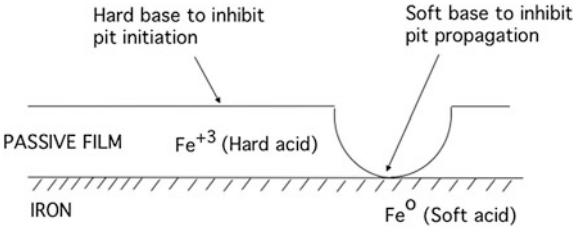

Fig. 1.30 Schematic representation of the inhibition of pit initiation or the its propagation according to the hard and soft acids and bases concept [113–117]

effective in causing film breakdown (although Br^- and I^- ions are larger than the Cl^- ion and thus have more difficulty in penetrating the passive film).

Aramaki reasoned that effective corrosion inhibitors of passive film breakdown should be Lewis bases whose hardness is greater that that of Cl^-. See Fig. 1.30. The following hard bases were found to be effective in increasing the pitting potential in a borate buffer containing 0.05 M Cl^-:

OTP^- (octyl thiopropionic acid) $C_8H_{17}S(CH_2)_2CO_2^-$
DS^- (N-dodecanoyl sarcosinate ion) $C_{11}H_{23}CON(CH_3)CH_2CO_2^-$
Ol^- (oleic acid ion) $C_{17}H_{33}CO_2^-$
Bz^- (benzoic acid) $C_6H_5CO_2^-$

See Fig. 1.31 which shows a typical anodic polarization curve marking the initiation of pits at the pitting potential E_{pit} and pit repassivation at the potential E_{rep}.

To inhibit the propagation of pits, i.e., pit growth, Aramakii reasoned that soft base inhibitors were required by the HSAB principle to interact with the underlying metal, Fe^o, which is a soft base, according to Table 1.7. See Fig. 1.30. Aramaki and coworkers [114, 117] investigated pit repassivation by measuring polarization curves in simulated pit environments (high in Cl^- ion concentration and low in pH

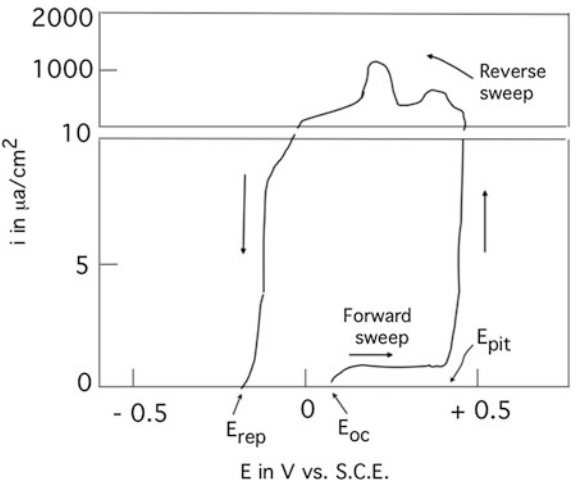

Fig. 1.31 Schematic representation of an anodic polarization curve marking the initiation of pits at the pitting potential E_{pit} and pit repassivation at the potential E_{rep}. E_{oc} refers to the open circuit (corrosion) potential. Redrawn from Fujioka et al. [117] by permission of Elsevier

values) or by measuring the repassivation potential, shown schematically in Fig. 1.31. Soft bases which were observed to be effective against pit propagation were:

TU	(thiourea) $CS(NH_2)_2$
PTU	(1-phenyl-2-thiourea) $C_6H_5NHSCNH_2$
DPTU	(1, 3-diphenyl-2-thiourea) $(C_6H_5NH)_2CS$
DBTU	(1, 3-dibutyl-2-thiourea) $(C_4H_9NH)_2CS$
Br^-	bromide ion
I^-	iodide ion

To inhibit both pit initiation and pit propagation Aramaki and coworkers [114, 117] tried various combinations of hard and soft bases. Not all combinations were successful, but the following combinations inhibited both pit initiation and pit propagation:

$$OTP^- + I^-$$
$$OTP^- + DBTU$$
$$Bz^- + DBTU \text{ (one combination)}$$

Some of these effects are shown in Fig. 1.32. Other combinations raised E_{pit} only but not E_{rep}, as is also shown in Fig. 1.31.

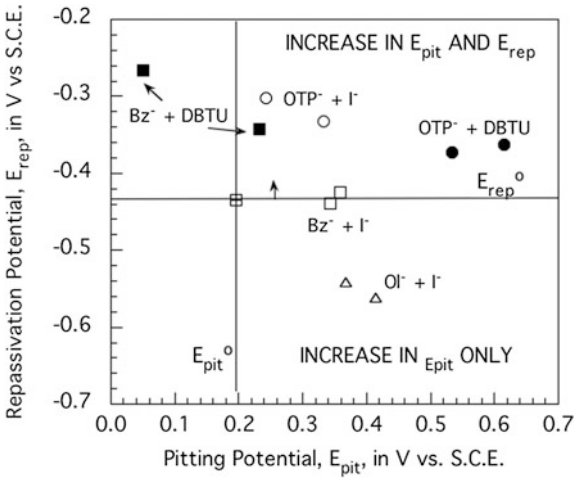

Fig. 1.32 Relationship between the pitting potential E_{pit} and the repassivation potential E_{rep} for iron in Cl^- containing borate buffer in the presence of various mixtures of hard and soft base inhibitors. See the text for the key to abbreviations. Redrawn from Aramaki et al. [114, 117] by permission of Elsevier

Interaction of Cations with Oxide Films

Because Cl^- anions interact with an $= AlOH_2^+$ surface at pH 7, then by the same reasoning aqueous cations, e.g. Na^+, should interact with an $= AlO^-$ surface at basic pH values. This interaction would produce a positively charged surface consisting of $= AlO^-Na^+$ groups, which in turn would attract Cl^- anions, so that pitting would easily occur at pH values above the isoelectric point. However, as mentioned earlier, the pitting potential of aluminum increases above the isoelectric point, so that a sequence of events involving an $= AlO^-Na^+Cl^-$ surface species does not occur.

Instead, it is known that various cations are inhibitors for the corrosion of aluminum and other metals [119–122]. In particular, cerium salts are effective corrosion inhibitors for aluminum and its alloys.

Aramaki [115, 116] has pointed out that if an alkaline solution contains metallic cations, the solubility product K_{sp} of the hydroxide (generally a small value) is easily exceeded. Thus, a hydroxide is precipitated onto the existent oxide film and this hydroxide interferes with the oxygen reduction reaction. In addition, the hydroxide changes gradually to an oxide. For example, if a basic solution contains dissolved Ce^{+3} ions:

$$Ce^{+3} + 3\,OH^- \rightarrow Ce(OH)_3 (K_{sp} = 1.6 \times 10^{-20}) \tag{1.47}$$

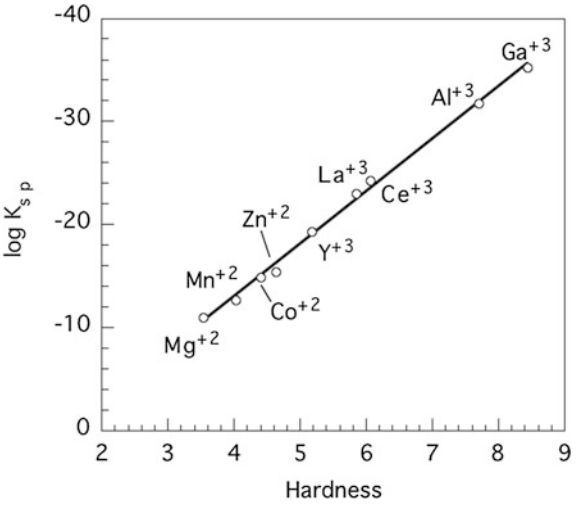

Fig. 1.33 The solubility product of various hydroxides as a function of the hardness index of the cation. Plotted from data of Aramaki [113, 115]

and then:

$$Ce(OH)_3 \rightarrow CeO_2 + H_2O + H^+ + e^- \tag{1.48}$$

Evidence that the prevailing oxidation state of precipitated cerium in alkaline aerated solutions is +4 has been given by Aldykewicz et al. [123].

Aramaki [113, 115] has treated the precipitation reaction, Eq. (1.47), in terms of Hard and Soft Acids and Bases (HSAB). For instance, inhibition of aluminum by cerum salts [120, 121] can be explained by the HSAB principle. The cation Ce^{+3} is classified as a hard acid [7] and the anion OH^- as a hard base, so by the HSAB principle, the precipitation reaction in Eq. (1.47) is favored. Aramaki [113, 115] has shown that the logarithm of the solubility product for many hydroxides is a linear function of the hardness index of the cation. See Fig. 1.33. Thus, the first step in the formation of a precipitated oxide is also subject to Lewis acid-Lewis base considerations.

Relationship Between the Isoelectric Point (pH_{pzc}) and the Potential of Zero Charge (E_{pzc}) for Passive Metals

General Remarks

The surface charge on passive oxide films can be varied in two different ways: first by changing the electrode potential, and second by changing the pH of the aqueous solution, as shown schematically in Fig. 1.34.

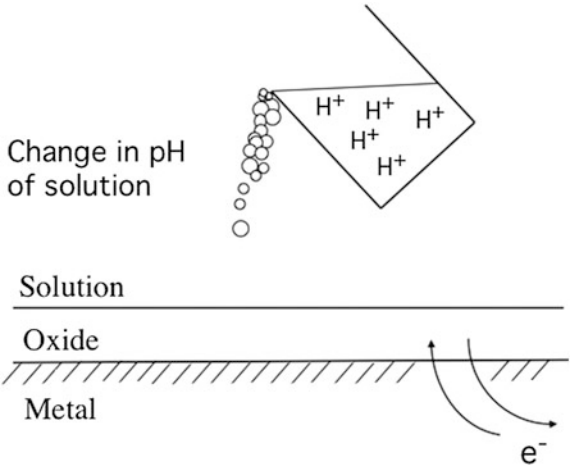

Fig. 1.34 Schematic illustration as to two different approaches to change the surface charge on a passive oxide film

The isoelectric point of the oxide film (pH_{pzc}) reflects how the charge on an oxide film responds to changes in pH of the solution, whereas the potential of zero charge (E_{pzc}) determines how the charge on an oxide film responds to changes in electrode potential of the oxide-covered metal. The relationship between these two important parameters has been examined recently [124] and is considered below. So far in this communication, we have considered isoelectric points but have not considered potentials of zero charge for passive metals.

It should be noted that the general term "point of zero charge" is imprecise and requires definition. This term is often used by colloid chemists to denote the pH value of the aqueous solution in which a surface (usually an oxide) attains a net zero charge, as described earlier (i.e., the isoelectric point).

Electrochemists, however, usually consider the "point of zero charge" to be the *potential* of zero charge (E_{pzc}), i.e., the electrode potential at which a metal/solution interface displays a net zero charge. Thus, the term "potential of zero charge" by convention refers to the bare (oxide-free) metal surface; and approaches such as scraping, abrasion, laser ablation, or judicious choice of electrolyte are employed to ensure that the metal surface is oxide-free. Indeed, the presence of an oxide film on the metal surface, is sometimes considered to be a bane and the experiment is thought to be compromised if the metal is oxide-covered. However, it is precisely the condition of an oxide-covered metal that is of interest in the study of passivity.

The isoelectric point (pH_{pzc}) and the potential of zero charge (E_{pzc}) of oxide-covered metals have the following properties:

1. The potential of zero charge (E_{pzc} or E_{fb}) is not a single quantity but varies with the pH according to [125, 126]:

$$E - E_{pzc} = -0.0591(pH - pH_{pzc}) \tag{1.49}$$

2. The electrode potential at the isoelectric point of the oxide-covered surface (pH_{pzc}) is the potential of zero charge (E_{pzc}) of the oxide-covered surface:

$$E_{pzc} = E \text{ at } pH = pH_{pzc} \tag{1.50}$$

Measurement of Potentials of Zero Charge for Passive Metals

Potentials of zero charge of oxide-covered metals can be determined from their semiconductor properties. A useful measure of the potential of zero charge of an oxide-covered metal surface is the flatband potential, E_{fb}. At the flatband potential there is no band bending due to surface charges, so that this potential is also the potential of zero charge. That is, $E_{fb} = E_{pzc}$ for oxide-covered metals.

The flatband potential can be measured from impedance analysis or from photoelectrochemical experiments. In impedance measurements, the flatband potential follows from Mott-Schottky plots [127]:

$$\frac{1}{C_{sc}^2} = \frac{8\pi}{\varepsilon e N_{sc}}\left[E - E_{fb} - \frac{kT}{e}\right] \tag{1.51}$$

where C_{SC} is the capacitance of the space charge region, N_{SC} is the carrier density, and the other symbols have their usual meanings, A plot of $1/C^2$ versus E gives a straight line, which extrapolated to $1/C^2 = 0$ gives $E_{fb} + kT/e$, and hence F_{fb}.

A second method of determining E_{fb} is from photoelectrochemical experiments, in which no photocurrent is generated at the flatband potential [127]. Thus, the photocurrent changes sign in passing through the flatband potential.

Potential Drop in the Metal/Oxide/Electrolyte System

The system under consideration is shown in Fig. 1.35. The electrode potential E versus some reference electrode of an oxide-covered metal immersed in an electrolyte is related to the inner potentials across the various phases or at interfaces. That is [126, 128, 129]:

$$E = \Delta\phi_{SC} + \Delta\phi_{H} + \Delta\phi_{GC} + \text{constant} \tag{1.52}$$

where ϕ_{SC} refers to the space charge region of the oxide semiconductor, ϕ_H is the inner potential in solution within the Helmholtz plane, and ϕ_{GC} is the inner potential at the juncture of the outer Helmholtz plane and the beginning of the Gouy-Chapman (diffuse region) of the electrical double layer. The term "constant" includes terms which are not pH-dependent, such as the potential drop at the juncture of the metal and its oxide film and the potential drop across the interior of the oxide film.

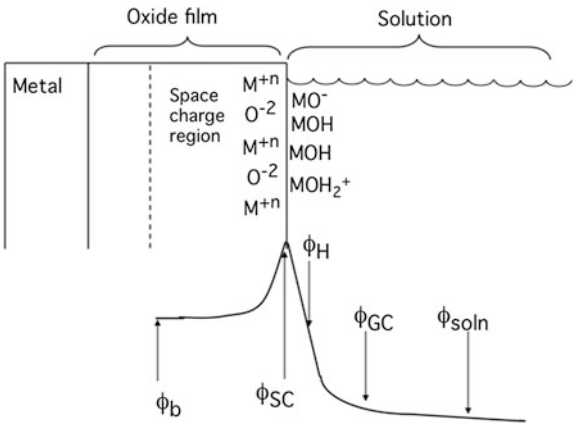

Fig. 1.35 Various interfaces present in the system: metal/oxide/solution. ϕ_{SC} refers to the innner potential at the outermost space charge region, ϕ_H is the inner Helmholtz potential, ϕ_{GC} the inner potential in the Gouy-Chapman diffuse double layer, and ϕ_{soln} the inner potential in the bulk of the aqueous solution. Adapted from Memming and Schwandt [129]

We are interested in the variation of each term in Eq. (1.52) with the pH of the aqueous solution. Thus,

$$\frac{\partial E}{\partial pH} = \frac{\partial \Delta\phi_{SC}}{\partial pH} + \frac{\partial \Delta\phi_{H}}{\partial pH} + \frac{\partial \Delta\phi_{GC}}{\partial pH} \tag{1.53}$$

It has been shown previously [124] that the last term in Eq. (1.53) is small and can be neglected. At the isoelectric point, $pH = pH_{pzc}$ and the electrode potential E is the potential of zero charge, E_{pzc}. Thus, Eq. (1.53) becomes:

$$\frac{\partial E_{pzc}}{\partial pH_{pzc}} = \frac{\partial \Delta\phi_{SC}}{\partial pH_{pzc}} + \frac{\partial \Delta\phi_{H}}{\partial pH_{pzc}} \tag{1.54}$$

Thus, there are two sets of surface reactions which must be considered. The first set of reactions involves the space charge side of the oxide/solution interface and the formation and/or maintenance of the surface hydroxyl groups. The second set of surface reactions involves the fate of the surface hydroxyl groups at the solution side of the oxide/solution interface in terms of their association or dissociation.

Space Charge Side of the Oxide/Solution Interface

Both metallic cations M^{+n} (solid) and oxide anions O^{-2} (solid) exist inside the space charge layer of the oxide at the oxide/solution interface and can interact with

aqueous species (H^+ or OH^-) to form or maintain the outermost layer of surface hydroxyl ions, as mentioned earlier. Although, the space charge region extends inward into the bulk of the oxide semiconductor, metallic cations or oxide anions in the bulk of the space charge region cannot interact with aqueous H^+ or OH^- ions. Thus, only that portion of the space charge region located near the oxide/solution interface will contribute to the pH-dependence of ϕ_{SC}. That is,

$$\frac{\partial \Delta\phi_{SC}}{\partial pH} = \frac{\partial(\phi_{SC} - \phi_b)}{\partial pH} = \frac{\partial \phi_{SC}}{\partial pH} \tag{1.55}$$

where ϕ_b is defined in Fig. 1.35.

Reactions of H^+ or OH^- ions with M^{+n} or O^{-2} in the space charge region near the oxide/solution interface can be written for either p-type or n-type oxides. We first consider p-type oxides. For the interaction of H^+ ions with oxide anions:

$$O^{-2}{}_s + H^+{}_{aq} + h^+{}_s \quad \rightarrow \quad OH_{surf} \tag{1.56}$$

where the subscripts s, aq, and surf refer to the solid, aqueous and surface phases, respectively, and h^+ refers to a hole. This reaction is shown schematically in Fig. 1.36.

The condition for equilibrium in Eq. (1.56) is:

$$\bar{\mu}(O_s^{-2}) + \bar{\mu}(H_{aq}^+) + \bar{\mu}(h_s^+) = \bar{\mu}(OH_{surf}) \tag{1.57}$$

where $\bar{\mu}_i$ is the electrochemical potential given by:

$$\bar{\mu}_i = \mu_i^O + RT \ln a_i + zF\phi \tag{1.58}$$

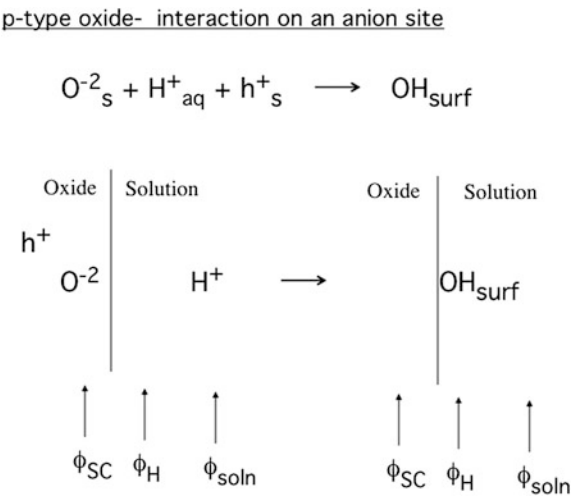

Fig. 1.36 Surface reaction on a p-type oxide between a hydrogen ion in solution and an oxide site

Table 1.8 Types of interactions between an oxide semiconductor and solution species

Type oxide	Interaction on	Example
p-type	Anion site	$O^{-2}{}_s + H^+{}_{aq} + h^+{}_s \rightarrow OH_{surf}$
p-type	Cation site	$Ni^{+2}{}_s + OH^-{}_{aq} + h^+{}_s \rightarrow Ni^{+2}{}_s + OH_{surf}$
n-type	Anion site	$O^{-2}{}_s + H^+{}_{aq} \rightarrow OH_{surf} + e^-{}_s$
n-type	Cation site	$Zn^{+2}{}_s + OH^-{}_{aq} \rightarrow Zn^{+2}{}_s + OH_{surf} + e^-{}_s$

The subscripts "s", and "aq" refer to solid and aqueous phases, and "surf" refers to the surface

where μ_i^o is the standard chemical potential, a_i is the activity, and z is the charge for charged surface species or ions located outside the Helmholtz plane (with z = 0 for uncharged particles). The term ϕ is the inner potential in the appropriate region. Taking care to use the proper inner potential for each species, as in Fig. 1.36, leads to:

$$\text{constant} + 2.303\ RT \log[H^+{}_{aq}] = F(\phi_{sc} - \phi_{soln}) \tag{1.59}$$

or:

$$\left(\frac{\partial \Delta\phi_{sc}}{\partial pH}\right) = -\frac{2.303RT}{F} \tag{1.60}$$

where $\Delta\phi_{sc} = \phi_{sc}^- - \phi_{soln}$ is the electrostatic potential in the space charge region relative to the bulk solution.

There are three other cases to consider, and these are listed in Table 1.8. Each of these three additional cases gives the same result as in Eq. (1.60) [124]. These surface reactions are modifications of those proposed by Matsumoto et al. [130, 131].

Solution Side of the Oxide/Solution Interface

The behavior of surface hydroxyl groups has been discussed earlier in this communication. The condition for equilibrium in Eq. (1.1) is:

$$\bar{\mu}(MOH_{surf}) + \bar{\mu}(H^+_{aq}) = \bar{\mu}(MOH^+_{2\,surf}) \tag{1.61}$$

and for Eq. (1.2)

$$\bar{\mu}(MOH_{surf}) = \bar{\mu}(MO^-{}_{surf} + \bar{\mu}(H^+_{aq}) \tag{1.62}$$

Use of Eq. (1.58) in Eq. (1.61) gives:

$$F(\phi_H - \phi_{soln}) = [\mu^o(MOH_{surf}) + \mu^o(H^+_{aq}) - \mu^o(MOH)^+_{2\,surf}] + RT\{\ln[MOH_{surf}] + \ln[H^+_{aq}] - \ln[MOH^+_{2\,surf}]\} \quad (1.63)$$

where concentrations (surface or bulk) are used in place of activities, ϕ_H is the inner potential in the Helmholtz layer, and ϕ_{soln} is the inner potential in the bulk of the solution. But $\phi_H - \phi_{soln} = \Delta\phi_H$, the potential drop across the Helmholtz layer relative to the bulk of solution. In addition:

$$\mu^o(MOH_{surf} + \mu^o(H^+_{aq}) - \mu^o(MOH)^+_{2\,surf}) = \Delta G^\circ_{-1} = -RT\ln K_{-1} \quad (1.64)$$

where K_{-1} is the acid dissociation constant for the reverse direction in Eq. (1.1).

Thus, Eq. (1.63) reduces to:

$$F\Delta\phi_H = -RT\ln K_{-1} + RT\ln\frac{[MOH_{surf}][H^+_{aq}]}{[MOH_2{}^+{}_{surf}]} \quad (1.65)$$

Similar considerations applied to Eq. (1.62) yield the result:

$$-F\Delta\phi_H = RT\ln K_2 - RT\ln\frac{[MOH^-_{surf}][H^+_{aq}]}{[MOH_{surf}]} \quad (1.66)$$

where K_2 is the acid dissociation constant for the forward direction in Eq. (1.2). Simultaneous solution of Eqs. (1.65) and (1.66) by elimination of the term $[MOH_{surf}]$ gives [132, 133]:

$$\frac{-2F\Delta\phi_H}{2.303\,RT} = \log(K_{-1}K_2) + \log\frac{[MOH_2{}^+{}_{surf}]}{[MO^-{}_{surf}]} + 2\,pH \quad (1.67)$$

At the isoelectric point when $\sigma_{surf} = 0$, $[MOH_2{}^+{}_{surf}] = [MO^-{}_{surf}]$, the pH is the isoelectric point pH_{pzc}, and the quantity $\Delta\phi_H$ at the isoelectric point can be denoted by $\Delta\phi^\circ_H$. Thus, Eq. (1.67) becomes:

$$\Delta\phi^O_H = -\frac{2.303\,RT}{2\,F}\log(K_{-1}K_2) - \frac{2.303\,RT}{F}pH_{pzc} \quad (1.68)$$

and:

$$\left(\frac{\partial\Delta\phi_H}{\partial pH}\right)_{pzc} = \frac{\partial\Delta\phi^O_H}{\partial pH_{pzc}} = -\frac{2.303\,RT}{F} \quad (1.69)$$

Table 1.9 Values of the isoelectric point of oxides or oxide films and of the potential of zero charge of oxide-covered metals which have n-type semiconductor oxides

Passive metal	Isoelectric point (pH_{pzc})	Measured E_{pzc} (V SCE)	pH of measurement	Method of measurement of E_{pzc}*	E_{pzc} at pH_{pzc} (V SCE)
Tungsten	2.5 [134] (bulk oxide) ~3 [135] (2.8 avg)	0.30 [136]	1.3	M-S	0.21
		0.57 [137]	0.3	M-S	0.42
		0.25 [138]	1.0	M-S	0.14
					(0.26 avg)
Platinum	3.3 [44] (passive film)	0.12 [139]	3.3	Capacitance minimum	0.12
Fe-20Cr Fe-12Cr	3–4.8 (3.9 avg) [15] (passive film)	−0.44 [140]	9.2	M-S	−0.13
		−0.32 [141]	8.4	M-S	−0.05
					(−0.09 avg)
Niobium	4.1 [53] (bulk oxide)	−0.16 [142]	4	M-S	−0.16
		0.2 [143]	0.6	PE	−0.01
					(−0.09 avg)
316 stainless steel	4.4–5.2 (4.7 avg) [42] (passive film)	−0.5 [144]	7.8	M-S	−0.32
		−0.43 [145]	8.35	M-S	−0.21
					(–0.27 avg)
Titanium	5.0 [31, 32] (passive film)	−0.24 [146]	0	M-S	−0.54
		−0.23 [142]	5	M-S	−0.23
		−0.83 [147]	14	PE	−0.30
		−0.31 [148]	1.0	M-S	−0.55
		−0.10 [149]	0	M-S	−0.40
		−0.20 [150]	0	M-S	−0.50
		−1.13 [151]	14.7	M-S	−0.56
		−0.3 [152]	7	PE	−0.18
		0.53 [153]	7	PE	−0.41
					(−0.41 avg)
Tin	5–6 (5.5 avg) [45] (bulk oxide)	−0.25 [154]	8.5	M-S	−0.073
		−0.19 [155]	6.0	M-S	−0.16
					(−0.12 avg)
Zirconium	5.9 avg of values compiled by Natishan [41] (bulk oxide)	−1.10 [156]	5.9	PE	−1.10
		−1.25 [157]	8.5	PE	−1.10
		−1.13 [147]	14	PE	−0.65
		−0.83 [147]	0.3	PE	−0.83
		−0.6 [158]	8.5	PE	−0.45
		−1.7 [159]	13	MS	−1.20
					(−0.96 avg)
Hafnium	7.1 [53] (bulk oxide)	0.0 [160]	0.0	PE	−0.42
Cobalt	7.8 [161] (bulk oxide)	−0.64 [162]	8.3	Capacitance minimum	−0.58

(continued)

Table 1.9 (continued)

Passive metal	Isoelectric point (pH_{pzc})	Measured E_{pzc} (V SCE)	pH of measurement	Method of measurement of E_{pzc}*	E_{pzc} at pH_{pzc} (V SCE)
Aluminum	9.5 [17] (passive film)	−0.80 [163]	7	M-S	−0.94
		−0.92 [164]	8.4	M-S	−0.98
		−0.81 [165]	7	PE	−0.96
		−1.40 [166]	7	M-S	−1.54
					(−1.11 avg)
Iron	9.9 [24, 30] (passive film)	−0.40 [167]	8.4	PE	−0.49
		−0.63 [147]	14	PE	−0.38
		−0.37 [168]	9.9	M-S	−0.37
		−0.35 [169]	8.4	M-S	−0.44
		−0.5 [170]	9.2	M-S	−0.54
		−0.35 [171]	8.3	M-S	−0.44
		−0.32 [172]	8.4	M-S	−0.41
		−0.46 [173]	9.4	M-S	−0.49
		−0.44 [174]	9.2	M-S	−0.48
					(−0.45 avg)
Zinc	9.3 [23] (passive film) 8.7 [175] (bulk oxide) (9.0 avg)	−0.6 [176]	10	M-S	−0.54
		−1.13 [177]	5	M-S	−1.37
		−0.61 [178]	8.9	M-S	−0.62
		−1.13 [147]	13	PE	−0.73
		−0.80 [179]	−0.8	PE	−0.92
					(−0.84 avg)
Lead	11.3 [180] (bulk oxide)	−1.27 [181]	13	M-S	−1.17
		−0.58 [182, 183]	0	M-S	−1.25
					(−1.21 avg)

* *M-S* Mott-Schottky, *PE* photoelectrochemistry

Thus, use of Eqs. (1.69) and (1.60) in:

$$\frac{\partial E_{pzc}}{\partial pH_{pzc}} = \frac{\partial \Delta\phi_{SC}}{\partial pH_{pzc}} + \frac{\partial \Delta\phi_{H}}{\partial pH_{pzc}} \tag{1.54}$$

gives:

$$\frac{\partial E_{pzc}}{\partial pH_{pzc}} = -\frac{2.303\,RT}{F} - \frac{2.303\,RT}{F} = -0.120\,V \tag{1.70}$$

Table 1.10 Values of the isoelectric point of oxides or oxide films and of the potential of zero charge of oxide-covered metals which have p-type semiconductor oxides

Passive metal	Isoelectric point (pH_{pzc})	Measured E_{pzc} (V SCE)	pH of measurement	Method of measurement of E_{pzc}*	E_{pzc} at pH_{pzc} (V SCE)
Chromium	5.3 [17] (passive film)	0.50 [182, 183]	5.3	M-S	0.50
		0.67 [182, 183]	5.3	M-S	0.67
		0.35 [184]	8.4	M-S	0.53
		0.5 [185]	9.2	M-S	0.74
		0.70 [186]	8.5	M-S	0.89
		0.46 [187]	9.2	M-S	0.70
		0.39 [174]	9.2	M-S	0.62
					(0.66 avg)
Nickel	8.4 [188] (bulk oxide)	0.3 [189]	8.4	PE	0.3
		0.4 [190]	8.4	M-S	0.4
		−0.14 [191]	14.5	M-S	0.22
		0.12 [192]	14.8	M-S	0.49
		0.72 [174]	9.2	M-S	0.76
		0.10 [148]	14	M-S	0.43
					(0.43 avg)
Copper	9.1 [23] 9.8 [193] (9.5 avg) (passive film)	−0.02 [147]	14	PE	0.24
		0.01 [194]	13	PE	0.22
		0.16 [195]	9.8	PE	0.12
		−0.275 [196]	12.85	PE	−0.07
					(0.13 avg)

* *M-S* Mott-Schottky; *PE* photoelectrochemistry

Numerical Evaluation

Tables 1.9 and 1.10 list literature values for the isoelectric point pH_{pzc} for oxide films on various passive metals or bulk oxides. Tables 1.9 and 1.10 also list values for the flatband potential ($E_{fb} = E_{pzc}$) for various semiconductor oxide films. These values were taken mostly from Mott-Schottky plots or from photoelectrochemical measurements. The value of E_{pzc} at the pH of measurement was converted to the pH of the isoelectric point, pH_{pzc}, by Eq. (1.49).

Figure 1.37 is a plot of E_{pzc} at the isoelectric point versus the value of the isoelectric point, pH_{pzc} for various metals having passive films which are oxide semiconductors. It can be seen that there is considerable scatter in the data, but that the relationship is linear, with $dE_{pzc}/dpH_{pzc} = -0.142$ V for n-type oxides and −0.115 V for p-type oxides. Both values are in nominal agreement with the value −0.120 V, as predicted by Eq. (1.70).

Reasons for the scatter in Fig. 1.37 are due to difficulties in either measurement or modeling and have been discussed in detail elsewhere [124]. The correlation

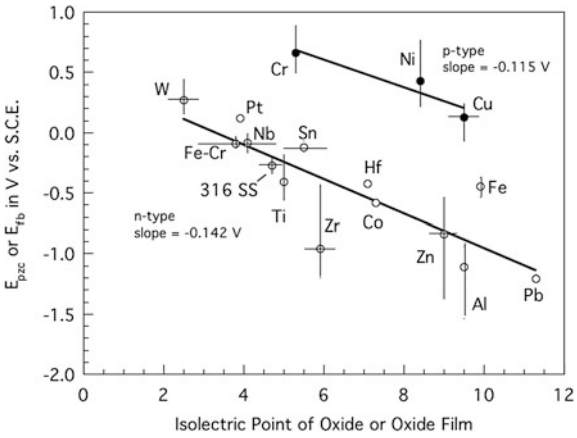

Fig. 1.37 Relationship between the isoelectric point (pH_{pzc}) and the potential of zero charge (E_{pzc} or E_{fb}) for various passive metals. The *open circles* are the average values of E_{fb} for n-type oxide films from Table 1.9. The *closed circles* are average values of E_{fb} for p-type oxide films from Table 1.10. The range of values for E_{fb} is also shown for each passive metal. Reproduced from Ref. [124] by permission of Elsevier

coefficient for the linear fit is fairly large (r = 0.84 for n-type oxides and r = 0.94 for p-type oxides. The observed slopes of E_{pzc} versus pH_{pzc} in Fig. 1.37 of −0.142 V for n-type oxides and −0.115 V for p-type oxides are in nominal agreement with the theoretical value −0.120 V.

Summary

The acid-base properties of oxide films on metal surfaces determine the surface charge character of the passive film. The surface charge character, in turn, is important in the surface phenomena of pitting, adhesion of polymers, corrosion inhibition, and the adsorption of inhibitive or aggressive ions from solution. Several illustrative examples have been given. The relationship between the isoelectric point and the potential of zero charge for passive films has also been considered.

References

1. E. McCafferty, A.C. Zettlemoyer, Disc. Faraday Soc. **52**, 239 (1971)
2. W. Stumm, *Chemistry of the Solid-Water Interface* (Wiley, New York, 1992)
3. E. McCafferty, J. Electrochem. Soc. **150**, B342 (2003)
4. E. McCafferty, J.P. Wightman, Surf. Interface Anal. **26**, 549 (1998)
5. W.F. Luder, Chem. Revs. **27**, 547 (1940)

6. G.N. Lewis, J. Franklin Inst. **226**, 293 (1938)
7. K. Aramaki, Corrosion Engineering **45**, 733 (1996)
8. T. Yamanaka, K. Tanabe, J. Phys. Chem. **80**, 1723 (1976)
9. M. Kaltchev, W.T. Tysoe, Surf. Sci. **430**, 29 (1999)
10. H. Ma, Y. Berthier, P. Marcus, Corros. Sci. **44**, 171 (2002)
11. D. Fairhurst, V. Ribitsch, Particle Size Distribution II. in ed. by T. Provder, ACS Symposium Series No, 472, p. 337, (American Chemical Society, Washington, DC, 1991)
12. C. Bellmann, A. Opfermann, H.-J. Jacobasch, H.-J. Adler, Fresnius. J. Anal. Chem. **358**, 255 (1997)
13. S. Roessler, R. Zimmerman, D. Scharnweber, C. Werner, H. Worch, Colloids Surf. B, Biointerfaces **26**, 387 (2002)
14. B.R. Strohmeier, Surf. Interface Anal. **15**, 51 (1990)
15. L. Boulangé-Petermann, A. Doren, B. Baroux, M.-N. Bellon-Fontaine, J. Colloid Interface Sci. **171**, 179 (1995)
16. L.-K. Chau, M.D. Porter, J. Colloid Interface Sci. **145**, 283 (1995)
17. E. McCafferty, J.P. Wightman, J. Colloid Interface Sci. **194**, 344 (1997)
18. E. McCafferty, J.P. Wightman, J. Adhe. Sci. Technol. **13**, 1415 (1999)
19. E. McCafferty, J. Electrochem. Soc. **146**, 2863 (1999)
20. W.A. Adamson, *Physical Chemistry of Surfaces*, 5th edn. (Wiley, New York, 1990). 386
21. P. Atkins, *Physical chemistry* (W. H. Freeman and Co., New York, NY, 1998). 161
22. S. Scotto-Sheriff, E. Darque-Ceretti, G. Plassart, M. Aucouturier, J. Mater. Sci. **34**, 5081 (1999)
23. D. Chvedov, E.L.B. Logan, Colloids Surf. A **240**, 211 (2004)
24. G.W. Simmons, B.C. Beard, J. Phys. Chem. **91**, 1143 (1987)
25. J.F. Watts, E.M. Gibson, Int. J. Adhes. Adhe. **11**, 105 (1991)
26. G.A. Parks, Chem. Revs. **65**, 177 (1965)
27. R.D. Shannon, C.T. Prewitt, Acta Cryst. **B25**, 925 (1969)
28. M. Delamar, J. Electron. Spectr. Rel. Phenom. **53**, c11 (1990)
29. C. Sun, J.C. Berg, Adv. Colloid Interface Sci. **105**, 151 (2003)
30. G. Kurbatov, E. Darque-Ceretti, M. Aucouturier, Surf. Interface Anal. **18**, 811 (1992)
31. E. McCafferty, J.P. Wightman, Appl. Surf. Sci. **143**, 92 (1999)
32. E. McCafferty, J.P. Wightman, T. Frank, Cromer. J. Electrochem. Soc. **146**, 2849 (1999)
33. K. Hu, F-R. F. Fan, A.J. Bard, A.C. Hillier J. Phys. Chem. B. **101**, 8298 (1997)
34. I. Larson, C.J. Drummond, D.Y.C. Chan, F. Grieser, J. Am. Chem. Soc. **115**, 11885 (1993)
35. M.G. Cattania, S. Ardizzone, C.L. Bianchi, S. Carella, Colloids Surf. A **76**, 233 (1993)
36. C.E. McNamee, Y. Tsujii, M. Matsumoto, Langmuir **21**, 11283 (2005)
37. P.G. Hartley, I. Larson, P.J. Scales, Langmuir **13**, 2207 (1997)
38. S. Veeramasuneni, M.R. Yalamanchili, J.D. Miller, J. Colloid Interface Sci. **184**, 594 (1996)
39. M.S. Lim, S.S. Perry, H.C. Galloway, D.C. Koeck, J. Vac. Sci. Technol. B **20**, 575 (2002)
40. S. Ardizzone, S. Trasatti, Adv. Colloid Interface Sci. **64**, 173 (1996)
41. P.M. Natishan, E. McCafferty, G.K. Hubler, J. Electrochem. Soc. **135**, 321 (1988)
42. N. Kallay, D. Kovacevic, I. Dedic, V. Tomasic, Corrosion **50**, 598 (1994)
43. H. Tamura, T. Oda, M. Nagayama, R. Furuichi, J. Electrochem. Soc. **136**, 2782 (1989)
44. N. Kallay, Z. Torbic, M. Golic, E. Matijevic, J. Phys. Chem. **95**, 7028 (1991)
45. T. Arai, D. Aoki, Y. Okaba, M. Fujihara, Thin Solid Films **273**, 322 (1996)
46. W.P. Hsu, L. Rönnquist, E. Matijevic, Langmuir **4**, 31 (1988)
47. M. Ozawa, M. Hattori, J. Alloys Compd. **408–412**, 560 (2006)
48. M. Mao, D. Fornasiero, J. Ralston, R. St. C. Smart, S. Sobieraj, Colloids Surf. A, **85**, 37 (1994)
49. H. Moriwaki, Y. Yoshikawa, T. Morimoto, Langmuir **6**, 847 (1990)
50. G.A. Kokarev, V.A. Kolesnikov, A.F. Gubin, A.A. Korabonav, Soviet Electrochem. **18**, 407 (1982)
51. D.E. Yates, T.W. Healy, J. Colloid Interface Sci. **52**, 222 (1975)
52. G.W. Smith, T. Salman, Canadian Met. Quart. **5**(2), 93 (1966)

53. M. Kosmulski, Langmuir **13**, 1615 (1997)
54. W. Janusz, J. Colloid Interface Sci. **145**, 119 (1991)
55. J.R. Galvele, in *Passivity of Metals*. ed by R.P. Frankenthal, J. Kruger (The Electrochemical Society Princeton, NJ 1978), p. 285
56. J.H. de Boer, H. Verwey in *Advances in Colloid Science*, ed. by Mark, E.J.W. (Interscience Publishers, New York, 1950) Vol. III, Chapter 1, p. 1
57. A. Kolics, A.S. Besing, P. Baradlai, R. Haasch, A. Weickowski, J. Electrochem. Soc. **148**, B251 (2001)
58. M. Kosmulski, Colloids Surf. A **83**, 237 (1994)
59. E. McCafferty, Corros. Sci. **45**, 1421 (2003)
60. E. McCafferty, Corros. Sci. **37**, 481 (1995)
61. L. Tomcsanyi, K. Varga, I. Bartik, G. Horanyi, E. Maleczki, Electrochim. Acta **34**, 855 (1989)
62. G. Okamato, T. Shibata, in Proceedings of the Third International Congress on Metallic Corrosion. Vol. 1, p. 396, Moscow (1969)
63. O.J. Murphy, J.O'M. Bockris, T.E. Pou, D.L. Cocke, G. Sparrow, J. Electrochem. Soc. **129**, 2149 (1982)
64. W.M. Carroll, C.B. Breslin, Br. Corros. J. **26**, 255 (1991)
65. P.M. Natishan, W.E. O'Grady, E. McCafferty, D.E. Ramaker, K. Pandya, A. Russell, J. Electrochem. Soc. **146**, 1737 (1999)
66. F.D. Bogar, R.T. Foley, J. Electrochem. Soc. **119**, 462 (1972)
67. S. Dallek, R.T. Foley, J. Electrochem. Soc. **123**, 1775 (1976)
68. J.R. Galvele, S.M. de De, Michele. Corros. Sci. **10**, 795 (1970)
69. B.N. Stirrup, N.A. Hampson, I.S. Midgley, J. Appl. Electrochem. **5**, 229 (1975)
70. H. Bohni, H.H. Uhlig, J. Electrochem. Soc. **116**, 906 (1969)
71. H. Kaesche, Z. Physik Chem. N. F. **34**, 87 (1962)
72. Z.A. Foroulis, M.J. Thubrikar, Werkstoffe u. Korros. **26**, 350 (1975)
73. J. O'M. Bockris and Lj. V. Minevski, J. Electroanal. Chem. **349**, 375 (1993)
74. J. Schultz, M. Nardin in *Adhesion Promotion Techniques*. ed. by K.L. Mittal, A. Pizzi (Marcel Dekker, New York 1999), p. 1
75. F.M. Fowkes, D.O. Tischler, J.A. Wolfe, L.A. Lannigan, C.M. Ademu-John, M.J. Halliwell, J. Polymer Sci. Polymer Chem. Edition, **22**, 547 (1984)
76. F.M. Fowkes, M.A. Mostafa, Ind. Eng. Chem. Prod. Res. Dev. **17**, 3 (1978)
77. F.M. Fowkes in *Encyclopedia of polymer science and engineering*. Supplement Volume (Wiley Interscience, New York 1989), p. 1
78. H.-J. Jacobasch, K. Grundke, S. Schneider, F. Simon, J. Adhes. **48**, 57 (1995)
79. M.A. Tshabalala, J. Appl. Polym. Sci. **65**, 1013 (1997)
80. C.J. van Oss, M. Chaudhury, R.J. Good, Chem. Rev. **88**, 927 (1988)
81. C.J. van Oss, R.J. Good, J. Macromol. Sci.-Chem. A, **26**, 1183 (1989)
82. R.J. Good, C.J. van Oss in *Modern approaches to wettability*. ed. by Schrader, M.E. Loeb, G. I (Plenum Press, New York 1992), p. 1
83. R.J. Good, J. Adhes. Sci. Technol. **6**, 1269 (1992)
84. A.D. Roberts, Langmuir **8**, 1479 (1992)
85. J.W. Chin, J.P. Wightman, J. Adhes. **41**, 23 (1993)
86. F. Bodino, N. Compiègne, L. Köhler, J.J. Pireaux, R. Caudano in Proceedings of the 20th Annual Meeting of the Adhesion Society. (ed. by L.T. Drzal, H.P. Schreiber) p. 41 (1997)
87. Y. Liu, S.H. Goh, S.Y. Lee, C.H.A. Huan, J. Polymer Sci. B Polymer Phys. **38**, 501 (2000)
88. J.F. Watts, M.M. Chehimi, E.M. Gibson, J. Adhesion **39**, 145 (1992)
89. S.R. Leadly, J.F. Watts, J. Electron Spectr. Related Phenom. **85**, 107 (1997)
90. D.C. Hansen, E. McCafferty, J. Electrochem. Soc. **143**, 114 (1996)
91. E. McCafferty, J. Adhes. Sci. Technol. **16**, 239 (2002)
92. I.A. Starostina, R.R. Khasbiullin, O.V. Stoyanov, A.E. Chalykh, Russian J. Appl. Chem. **74**, 1920 (2001)
93. W. Funke, Prog. Org. Coat. **31**, 5 (1997)

94. J.H. W. de Wit in Corrosion mechanisms in theory and practice. ed. by P. Marcus, J. Oudar (Marcel Dekker, New York 1995), p. 581
95. H. Leidheiser, Jr. W. Funke, J. Oil Col. Chem. Assoc. **70**(5), 121 (1987)
96. Y.-F. Yu, J.J. Chessick, A.C. Zettlemoyer, J. Phys. Chem. **63**, 1626 (1959)
97. P.F. Rossi, M. Bassoli, G. Olivera, F. Guzzo, J. Thermal Anal. **41**, 1227 (1994)
98. Y.-F. Yu Yao, J. Phys. Chem. **67**, 2055 (1963)
99. M. Nakazawa, G.A. Somorjai, Appl. Surf. Sci. **84**, 309 (1995)
100. Y.-F. Yu Yao, J. Phys. Chem. **69**, 3930 (1965)
101. T. Matsuda, T. Taguchi, M. Nagao, J. Thermal Anal. **38**, 183 (1992)
102. J.G.N. Thomas, Br. Corros. J. **5**, 41 (1970)
103. J.E.O. Mayne, C.L. Page, Br. Corros. J. **7**, 115 (1972)
104. B. Müller, W. Kläger, Corros. Sci. **38**, 1869 (1996)
105. B. Müller, React. Funct. Polym. **39**, 165 (1999)
106. F.P. Dwyer, D.D. Mellor, *Chelating agents and metal chelates* (Academic Press, New York, NY, 1964)
107. A. Weisstuch, D.A. Carter, C.C. Nathan, Mater. Prot. Perf. **10**(4), 11 (1971)
108. D.C. Zecher, Mater. Perf. **15**(4), 33 (1976)
109. R.L. LeRoy, Corrosion **34**, 98 (1978)
110. B. Müller, W. Kläger, G. Kubitzki, Corros. Sci. **39**, 1481 (1997)
111. F. Tirbonod, C. Fiaud, Corros. Sci. **18**, 139 (1978)
112. Y.I. Kuznetsov, T.I. Bardasheva, Russ. J. Appl. Chem. **66**, 905 (1993)
113. K. Aramaki, Corr. Eng. **46**, 389 (1997)
114. K. Aramaki, Corr. Eng. **46**, 913 (1997)
115. K. Aramaki, Corrosion **55**, 157 (1999)
116. K. Aramaki, Corros. Sci. **43**, 1573 (2001)
117. E. Fujioka, H. Nishihara, K. Aramaki, Corros. Sci. **38**, 1669 (1996)
118. R.G. Pearson, J. Chem. Ed. **45**, 581 (1968)
119. W.R. Buck III, H. Leidheiser Jr, Corrosion **14**, 308t (1958)
120. B.R.W. Hinton, D.R. Arnott, N.E. Ryan, Met. Forum **7**(4), 211 (1984)
121. D.R. Arnott, B.R.W. Hinton, N.E. Ryan, Mater. Prot. **26**(8), 42 (1987)
122. M.G.A. Khedr, A.M.S. Lashien, Corros. Sci. **33**, 137 (1992)
123. A.J. Aldykewicz, A.J. Davenport, H.S. Isaacs, J. Electrochem. Soc. **143**, 147 (1996)
124. E. McCafferty, Electrochim. Acta **55**, 1630 (2010)
125. H. Gerischer, Electrochim. Acta **34**, 1005 (1989)
126. S.R. Morrison, in *Electrochemistry at semiconductor and oxidized metal electrodes*. (Plenum Press, New York 1980), p. 56–62
127. J.O'M. Bockris, S.U.M. Khan, *Surf. Electrochem.* (Plenum Press, New York, 1993), pp. 179–182
128. J.O'M. Bockris, A.K.N. Reddy, *Modern electrochemistry*. Vol. 2 (Plenum Press, New York 1977), p. 673
129. R. Memming, G. Schwandt, Angew. Chem. Internat. Ed. **6**, 851 (1967)
130. Y. Matsumoto, T. Yoshikawa, E. Sato, J. Electrochem. Soc. **136**, 1389 (1989)
131. Y. Matsumoto, K. Sugiyama, E. Sato, J. Electrochem. Soc. **135**, 98 (1988)
132. S. Levine, A.L. Smith, Disc. Faraday Soc. **52**, 290 (1971)
133. D.E. Yates, S. Levine, T.W. Healey, J. Chem. Soc. Faraday Trans. I **70**, 1807 (1974)
134. M. Anik, T. Consizoglu, J. Appl. Electrochem. **36**, 603 (2006)
135. M. Anik, K. Osseo-Asare, J. Electrochem. Soc. **149**, B224 (2002)
136. S.R. Biaggio, R.C. Rocha-Filho, J.R. Vilche, F.E. Varela, L.M. Gassa, Electrochim. Acta **42**, 1751 (1997)
137. F. Di Quarto, A. Di Paola, C. Sunseri, Electrochim. Acta **26**, 1177 (1981)
138. G. Vazquez, I. Gonzalez, J. Electrochem. Soc. **154**, C702 (2007)
139. E. Gileadi, S.D. Argade, J.O'M. Bockris. J. Phys. Chem. **70**, 2044 (1966)
140. J.-B. Lee, S.-W. Kim, Materials. Chem. Phys. **104**, 98 (2007)
141. E.B. Castro, J.R. Vilche, Electrochim. Acta **38**(1567), 775 (1993)

142. K.E. Heusler, K.S. Yun, Electrochim. Acta **22**, 977 (1977)
143. M. Arita, Y. Hayashi, Mat Trans JIM **35**, 233 (1994)
144. M. Da Cunha Belo, B. Rondot, C. Compere, M.F. Montemor, A.M. Simoes, M.G.S. Ferreira, Corros. Sci. **40**, 491 (1998)
145. I. Nicic, D.D. Macdonald, J. Nuclear Mater. **379**, 54 (2008)
146. J.W. Schultze, U, Stimming, J. Weise, Ber. Bunsenges. Phys. Chem. **86**, 276 (1982)
147. T.D. Burleigh, Corrosion **45**, 464 (1989)
148. S.P. Harrington, T.M. Devine, J. Electrochem. Soc. **155**, C381 (2008)
149. A.S. Bondarenko, G.A. Ragoisha, J. Solid State Electrochem. **9**, 845 (2005)
150. D.-S. Kong and J.-X, Wu, J. Electrochem. Soc. **155**, C32 (2008)
151. S.U.M. Khan, J. Akikusa, J. Electrochem. Soc. **145**, 89 (1998)
152. T. Bachmann, W. Vonau, P. John, Anal. Bioanal. Chem. **374**, 715 (2002)
153. P. Clechet, J.-R. Martin, R. Olier, C. Vallouy, C. R. Acad. Sci. Ser. C **887** (1976)
154. S. Kapusta, N. Hackerman, Electrochim. Acta **25**, 949 (1980)
155. M. Metikos-Hukovic, S. Omanovic, A. Jukic, Electrochim. Acta **45**, 977 (1999)
156. F. DiQuarto, S. Piazza, C. Sunseri, M. Yang, S.-M. Cai, Electrochim. Acta **41**, 2511 (1996)
157. M. Santamaria, F. Di Quarto, H. Habazaki, Electrochim. Acta **53**, 2272 (2008)
158. S.J. Lee, E.A. Cho, S.J. Ahn, H.S. Kwon, Electrochim. Acta **46**, 2605 (2001)
159. J.-Y. Huot, J. Appl. Electrochem. **22**, 852 (1992)
160. F. DiQuarto, M. Santamaria, P. Skeldon, G.E. Thompson, Electrochim. Acta **48**, 1143 (2003)
161. S. Ardizzone, G. Spinolo, S. Trasatti, Electrochim. Acta **40**, 2683 (1995)
162. D. Gallant, M. Pézolet, S. Simard, Electrochim. Acta **52**, 4927 (2007)
163. L. Kobotiatis, N. Kioupis, P.G. Koutsoukos, Corrosion **53**, 562 (1997)
164. J.O'M. Bockris, Y. Kang, J. Solid State Electrochem. **1**, 17 (1997)
165. J.C.S. Fernandes, R. Picciochi, M. Da Cunha Belo, T. Moura e Silva, M.G.S. Ferreira, I.T.E. Fonseca, Electrochim. Acta, **49**, 4701 (2004)
166. F.J. Martin, G.T. Cheek, W.E. O'Grady, P.M. Natishan, Corros. Sci. **47**, 3187 (2005)
167. P. Schmuki, H. Böhni, Electrochim. Acta **40**, 775 (1995)
168. S.M. Wilhelm, N. Hackerman, J. Electrochem. Soc. **128**, 1668 (1981)
169. E.B. Castro, J.R. Vilche, Electrochim. Acta **38**(1567), 775 (1993)
170. L. Hamadou, A. Kadri, N. Benbrahim, Appl. Surf. Sci. **252**, 1510 (2005)
171. Y.M. Zeng, J.L. Luo, Electrochim. Acta **48**, 3551 (2003)
172. F.M. Delnick, N. Hackerman, J. Electrochem. Soc. **126**, 732 (1979)
173. V. Horvat-Radosevic, K. Kvastek, Electrochim. Acta **42**, 1403 (1997)
174. M. Da Cunha Belo, N.E. Hakiki, M.G.S. Ferreira, Electrochim. Acta. **44**, 2473 (1999)
175. M. Valtiner, S. Borodin, G. Grundmeier, Langmuir **24**, 5350 (2008)
176. A.E. Bohe, J.R. Vilche K. Jüttner, W.J. Lorenz, W. Kautek, W. Paatsch, Corros. Sci. **32**, 621 (1991)
177. L. Sziraki, A. Cziraki, I. Gerocs, Z. Vertesy, L. Kiss, Electrochim. Acta **43**, 175 (1998)
178. H. Mishima, B.A. Lopez de Mishima, E. Santos, C.P. De Pauli, K. Azumi, N. Sato, Electrochim. Acta **36**, 1491 (1991)
179. E.A. Thompson, T.D. Burleigh, Corros. Eng. Sci. Technol. **42**, 237 (2007)
180. J. Biscan, M. Kosec, N. Kallay, Colloids Surf. A **79**, 217 (1993)
181. S.-J. Xia, W.-F. Zhou, Electrochim. Acta **40**, 175 (1995)
182. Z.-L. He, C. Pu, W.-F. Zhou, J. Power Sources **39**, 225 (1992)
183. D.-S. Kong, S.-H. Chen, C. Wang, W. Yang, Corros. Sci. **45**, 747 (2003)
184. S. Virtanen, P. Schmuki, H, Böhni, P Vuoristo, T. Mäntylä, J. Electrochem. Soc. **142**, 3067 (1995)
185. M.G.S. Ferreira, M. Da Cunha Belo, N.E. Hakiki, G. Goodlet, M.F. Montemor, A.M. P. Simoes, J. Braz. Chem. Soc. **13**, 433 (2002)
186. J.S. Kim, E.A. Cho, H.S. Kwon, Electrochim. Acta **47**, 415 (2001)
187. G. Goodlet, S. Faty, S. Cardosa, P.P. Freitas, A.M.P. Simoes, M.G.S. Ferreira, M. Da Cunha Belo. Corros. Sci. **46**, 1479 (2004)

188. G.A. Kokarev, V.A. Kolesnikov, A.F. Gubin, A.A. Korabonav, Soviet Electrochem. **18**, 407 (1982)
189. H.J. Jang, C.J. Park, H.S. Kwon, Electrochim. Acta **50**, 3503 (2005)
190. E. Sikora, D.D. Macdonald, Electrochim. Acta **48**, 69 (2002)
191. M.J. Madou, M.C.H. McKubre, J. Electrochem. Soc. **130**, 1056 (1983)
192. J. Kang, Y. Yang, X. Jiang, H. Shao, Corros. Sci. **50**, 3576 (2008)
193. N. Kallay, Z. Torbic, E. Barouch, J. Jednacak-Biscan, J. Colloid Interface Sci. **118**, 431 (1987)
194. U. Collisi, H.-H. Strehblow, J. Electroanal. Chem. **284**, 385 (1990)
195. K. Nakaoka, J. Ueyama, K. Ogura, J. Electrochem. Soc. **151**, C661 (2004)
196. F. Caballero-Briones J.M. Artes, I. Diaz-Perez, P. Gorostiza, F. Sanz, J. Phys. Chem. C **113**, 1028 (2009)

Chapter 2
Capillarity and Corrosion

Introduction

The surface of a liquid or solid exhibits the property of surface tension because molecules at the surface of the liquid or solid have fewer neighbors than those in the bulk. This situation leads to a net force perpendicular to the surface plane toward the interior of the liquid (or solid). In the case of solids, the property is called its surface free energy and may depend on the orientation of the solid surface.

The surface tension of water at 20 °C is 72.8 mN/m (millinewtons/m). The following units are equivalent:

$$72.8\,\text{dynes/cm} = 72.8\,\text{erg/cm}^2 = 72.8\,\text{mN/m} = 72.8\,\text{mJ/m}^2$$

Some values of surface tension for various liquids are given in Table 2.1 [1, 2].

Capillarity

When a small-diameter glass tube is immersed in a liquid, the liquid will rise in the capillary tubing, as shown in Fig. 2.1. (If the liquid is mercury there will be a depression rather than a rise in the capillary column, but we will be dealing with only aqueous fluids here.) The height of the capillary rise (h) is given by:

$$h = \frac{2\gamma}{\rho g r} \tag{2.1}$$

E. McCafferty, *Surface Chemistry of Aqueous Corrosion Processes*,
SpringerBriefs in Materials, DOI 10.1007/978-3-319-15648-4_2

Table 2.1 Some surface tension values in mN/m at 20 °C [2]

Water	72.94
Methylene iodide	67.00
Dimethyl sulfoxide	43.54
Benzene	28.88
Methanol	22.50
Perfluoroheptane	13.19

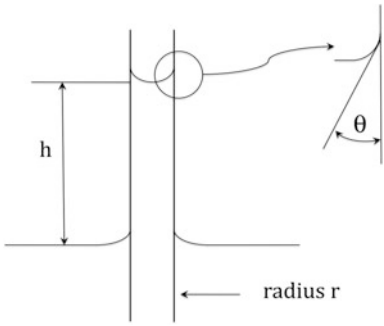

Fig. 2.1 Capillary rise of water in a small-diameter glass tube

where γ is the surface tension of the liquid, ρ is the density of the wetting liquid, g is the acceleration due to gravity, and r is the radius of the capillary.

This equation arises as follows. The force upward in the capillary liquid is:

$$F(\text{up}) = \gamma(2\pi r)\cos\theta \tag{2.2}$$

where θ is the contact angle and is usually zero (see Fig. 2.1).

The downward force is due to the weight of the liquid and is given by:

$$F(\text{down}) = \pi r^2 \rho g h \tag{2.3}$$

At equilibrium, the force up and the force down are equal:

$$F(\text{up}) = F(\text{down}) \tag{2.4}$$

This gives Eq. (2.1).

Figure 2.2 shows some calculated values of the capillary rise h for various capillary radii r. The smaller the capillary radius, the higher the capillary rise.

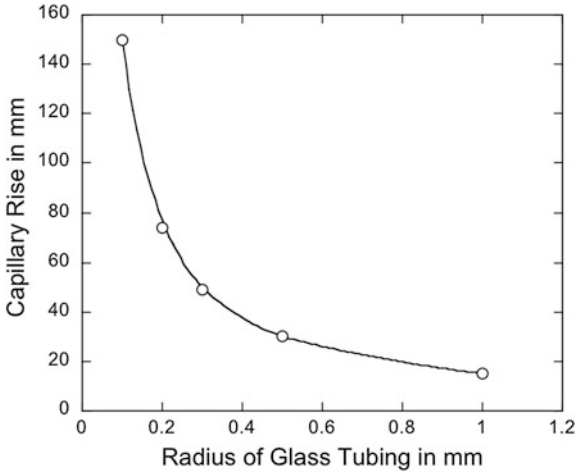

Fig. 2.2 Calculated capillary rise h (in mm) for various glass tubing radii r (in mm)

Application to Organic Coatings

It is well-known that organic coatings do not form perfect barriers to corrosion, but instead they are semi-permeable membranes into which water, oxygen, and chloride ions can pass. Nguyen et al. [3] have detected the presence of molecular water in organic coatings on silicon using Fourier transform infrared-multiple internal reflection. Their results showing the accumulation of water at the organic coating/metal interface are given in Fig. 2.3. Consider an organic coating which is 500 μm

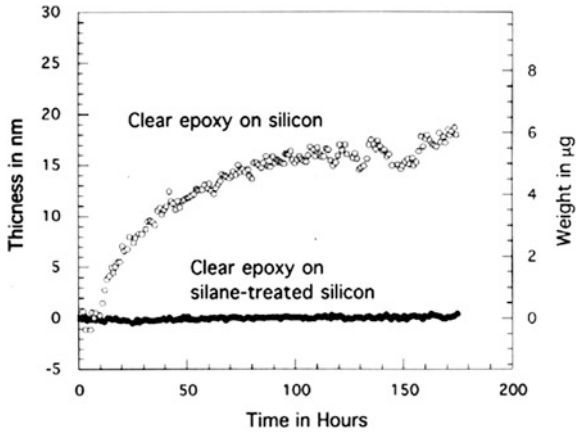

Fig. 2.3 Thickness and amount of water at the coating/substrate interface for clear epoxy coatings on silicon and silane-treated silicon. The epoxy coating thickness was 130–140 mm. Redrawn from Nguyen et al. [3] with the permission of Elsevier

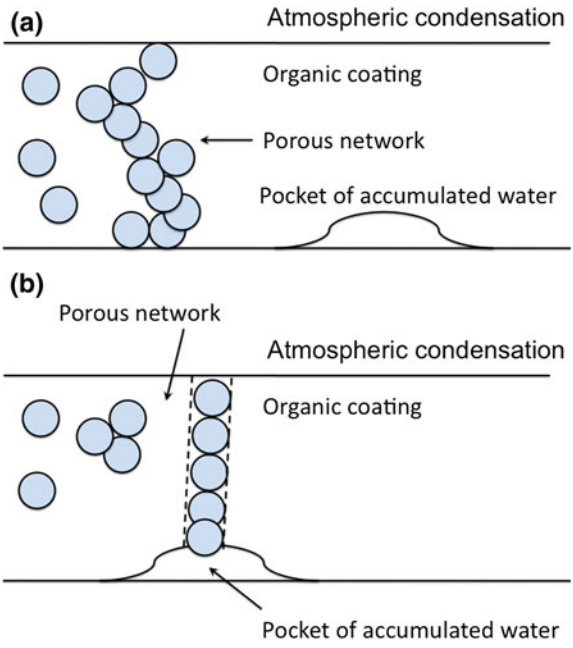

Fig. 2.4 **a** Schematic drawing of an irregularly shaped capillary path in an organic coating. **b** Capillary rise in a porous organic coating

thick (0.5 mm) and having an array of pores which align to give an irregularly shaped capillary path through the organic coating, as shown in Fig. 2.4.

If the accumulated liquid water at the base of the organic coating encounters the porous path in the coating, it will be possible for liquid water at the base of the coating to undergo capillary rise. For an effective pore radius of 3 μm, the height of capillary rise is calculated from Eq. (2.1) to be h = 5.0 m. This means that the capillary height far exceeds the thickness of the organic coating. See Table 2.2.

If the effective pore radius is 30 μm, the calculated height of capillary rise is 0.50 m. We can then consider that some of the organic matter from the coating can leach out into solution, so that the surface tension of the liquid phase will decrease, say to half its value for pure water, 36 mN/m. In that case, the calculated height of capillary rise is still substantial at 0.24 m and exceeds the thickness of the organic coating. Thus, the aqueous solution in the pores connects the internal electrolyte within the network of pores to the external electrolyte, which may be a thin film of water condensed from the atmosphere. This serves to promote degradation of the organic coating and underfilm corrosion.

Table 2.2 Calculated capillary rise in an organic coating

Radius r (μm)	Surface tension γ (mN/m)	Calculated capillary rise h (m)
3	72.8	5.0
30	72.8	0.50
30	36	0.24

Young and Laplace Equation

The pressure difference Δp across a spherical bubble of a fluid is given by the Young and Laplace equation:

$$\Delta p = 2\gamma/r \tag{2.5}$$

where r is the radius of the spherical bubble. This equation arises by considering the free energy change involved when a spherical bubble expands from radius r to radius r + dr. The free energy change is:

$$\Delta G = \gamma\, dA - \Delta p\, dV \tag{2.6}$$

where A is the area of the bubble and V is its volume.

The minus sign in Eq. (2.6) is required because work is done by the system. With $A = 4\pi r^2$, $dA = 8\pi r dr$. With $V = (4/3)\pi r^3$, $dV = 4\pi r^2 dr$. Substitution of these simple expressions for dA and dV into Eq. (2.6) with $\Delta G = 0$ at equilibrium gives the result in Eq. (2.5).

If the curved surface is not spherical but instead has two principal radii of curvature r_1 and r_2 as in Fig. 2.5, then the term 1/r in Eq. (2.5) is replaced by the term $(1/r_1 + 1/r_2)$, and the Young and Laplace equation becomes:

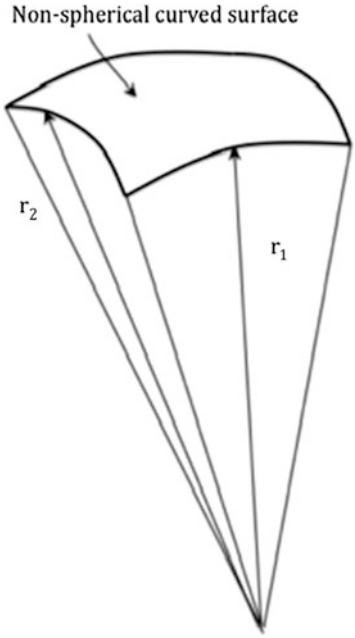

Fig. 2.5 A curved surface defined by two different radii of curvature. Adapted from Ref. [1], p. 9

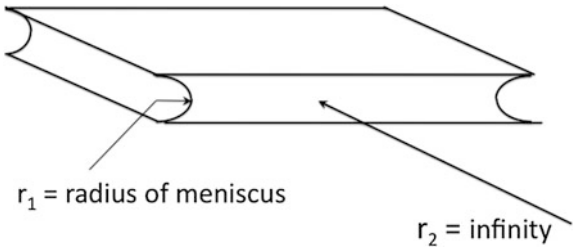

Fig. 2.6 The force required to separate two flat glass plates (separated by a thin film of liquid) can be calculated from the Young and Laplace equation

$$\Delta p = \gamma\left(\frac{1}{r_1} + \frac{1}{r_2}\right) \tag{2.7}$$

The derivation of this equation has been given by Adam [1] and Adamson [2]. When $r_1 = r_2 = r$, Eq. (2.7) reduces to Eq. (2.5).

Force Between Glass Plates

The Young and Laplace equation can be used to calculate the pressure required to separate two flat glass plates which are held together by a thin film of water (or of an aqueous solution). See Fig. 2.6. Here r_1 is given by the radius of curvature of the meniscus and r_2 = infinity. Thus,

$$\Delta p = \gamma\left(\frac{1}{r_1}\right) \tag{2.8}$$

if the two glass plates are separated by a 0.5 mm thin layer of water, then Δp is calculated to be $\Delta p = 146$ Pa. Note that the calculated pressure difference depends only on the surface tension of the wetting liquid and on the geometry of the system. The material properties of the solids are not involved in the calculation. The force between the two glass plates is then: Force = $\Delta p \times$ (Wetted area of plates).

Application to Poultice Corrosion

Poultice corrosion is the name given collectively to corrosion that results from the accumulation of dirt, dust, corrosion products, and other forms of debris.

When this happens, a highly corrosive condition can be created. Strictly speaking, poultice corrosion is not a separate form of corrosion but shares many

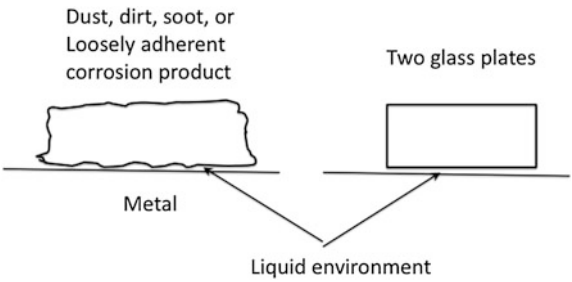

Fig. 2.7 Separation of two glass plates is a model for removing foreign objects from a metal surface

common features with crevice corrosion, which has been discussed in more detail elsewhere by the author [4].

The Young and Laplace equation in the form of Eq. (2.8) can be used to calculate the pressure required to remove a piece of debris from a surface, as shown in Fig. 2.7. This is because the material properties of the solids are not involved in the calculation. Knowing this required pressure, we can assess which cleaning methods will provide sufficient energy to surpass the adhesive force keeping the debris particle connected to the metal surface.

Accumulated dirt, dust, corrosion products, and other forms of debris often are contaminated with oil.

Then, the principles of detergency can be applied. See Fig. 2.8 which is adapted from Adamson [2] and shows an oil-contaminated particle before and after detachment. The change in free energy for detachment is:

$$\Delta G = \gamma_{wo} + \gamma_{mw} - \gamma_{mo} \tag{2.9}$$

where the subscripts refer in turn to the following interfaces: water/oil-contaminated particle, metal/water, and metal/oil-contaminate particle. For the process to be spontaneous we need $\Delta G < 0$. This leads to:

$$\gamma_{mo} > \gamma_{wo} + \gamma_{mw} \tag{2.10}$$

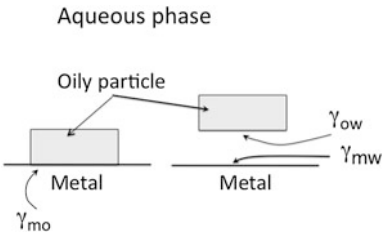

Fig. 2.8 Surface free energy relationships in the detachment of an oily particle from a metal surface. Adapted from Adamson [2] with the kind permission of John Wiley

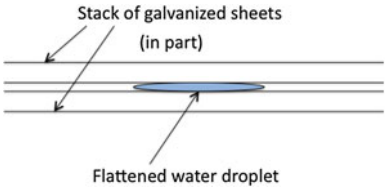

Fig. 2.9 Schematic diagram of a "wet pack" used to test the white rusting (wet storage stain) of galvanized sheets

Equation (2.10) is the condition which describes the effect of detergents on the detachment of oily dirt or oily debris from a metal surface. Detergents which can reduce γ_{wo} or γ_{mw} will serve to make the inequality in Eq. (2.10) hold. Thus, useful detergents are those which can adsorb both at the oily particle/water interface and at the metal/water interface.

Interfacial tensions can be measured with a Wilmhelmy balance in which the force is measured to immerse a thin plate into a two-liquid system. Details are given elsewhere for measurements for the chromium/hexadecane/aqueous solution interfaces [5].

Application to White Rusting

Stacked sheets of galvanized steel can undergo a phenomenon called white rusting (wet storage stain). Here the spaces between adjacent metal sheets act like capillaries for the ingress of water. A differential oxygen cell is set up between metal under the outside of the flattened water droplet (the cathode) and metal in contact with the interior of the water droplet (the anode) [4]. White rusting can be minimized by the use of post-galvanized chemical surface treatments, vapor phase inhibitors, and by storage in a low humidity environment.

The effect of various surface treatments on white rusting can be tested by the use of "wet packs" of galvanized steel. Here small water droplets are deliberately placed between stacked sheets for later visual inspection, as shown schematically in Fig. 2.9.

References

1. N.K. Adam, *The Physics and Chemistry of Surfaces* (Dover Publications, New York, 1968)
2. A.W. Adamson, *Physical Chemistry of Surfaces* (Wiley, New York, 1990)
3. H. Nguyen, E. Byrd, D. Bentz, C. Lin, Prog. Org. Coat. **27**, 181 (1996)
4. E. McCafferty, *Introduction to Corrosion Science* (Chapter 10). (Springer, New York, 2010)
5. E. McCafferty, J.P. Wightman, J. Colloid Interface Sci. **194**, 344 (1997)

Chapter 3
A Recent Model of Passivity for Fe-Cr and Fe-Cr-Ni Alloys

Passivity is the reduction in chemical or electrochemical activity of a metal surface due to the formation of a thin protective oxide film tens to hundreds of angstroms thick.

Fe-Cr Alloys

It has long been known that the introduction of 13 at.% chromium into iron renders the surface of Fe-Cr binary alloys passive. Various previous explanations and their limitations have been discussed elsewhere [1].

This chapter summarizes the graph theory model of passivity developed recently by E. McCafferty [1, 2]. In brief this model shows that there is a critical minimum concentration of Cr^{3+} ions in the oxide film so as to form a continuous network of –Cr–O–Cr– bridges in the oxide film. This condition is provided by the Fe-13 at.% Cr binary alloy.

A mathematical graph is a collection of points (called vertices) connected by lines called edges. The mathematical graph for $Cr_2O_3(G_o)$ is shown in Fig. 3.1.

The vertices of the graph represent Cr^{3+} ions (atoms) whereas edges represent O^{2-} ions. The size of G_o is given by its number of edges. If the number of vertices is N, then the number of edges A is $A(G_o) = (3/2)N$ (to preserve stoichiometry). The configuration of G_o is given by a quantity called the Randic index $X(G_o)$ (3):

$$X(G_o) = \sum_{\text{edges}} (ij)^{-0.5} \tag{3.1}$$

where i and j are the degrees of the vertices connecting the edge ij. (A vertex has a degree 2, for example, if two edges meet at that vertex).

It is shown previously that a simple calculation gives $X(G_o) = N/2$.

Next the composition of the oxide film is changed conceptually by insertion of Fe^{3+} ions so as to give a new graph G having the new properties A(G) and X(G).

E. McCafferty, *Surface Chemistry of Aqueous Corrosion Processes*,
SpringerBriefs in Materials, DOI 10.1007/978-3-319-15648-4_3

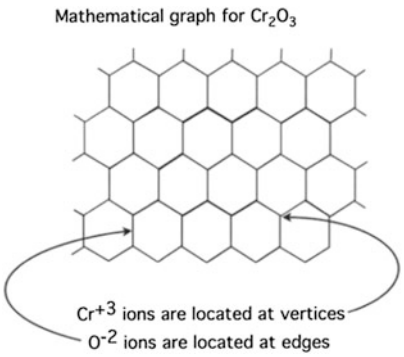

Fig. 3.1 Mathematical graph for chromium oxide. The vertices of the graph represent chromium ions and the edges denote oxygen ions. Reproduced by permission of Elsevier

Following Meghirditchian [3] we define a connectivity function

$$\delta = \frac{X(G)A(G) - X(G_o)A(G_o)}{X(G_o)A(G_o)} \tag{3.2}$$

where G_o refers to the original graph for Cr_2O_3 before the introduction of Fe^{3+} ions, and G refers to the new graph containing both Cr^{3+} and Fe^{3+} ions. Large values of δ indicate that the connectivity of the new graph is very much different than the original graph, whereas small values of δ mean that the connectivities of the two graphs are similar. Note that $\delta = 0$ when $G = G_o$.

Figure 3.2 shows the insertion of Fe^{3+} ions into the graph for Cr_2O_3. The composition of the oxide film after insertion of Fe^{+} ions is $xFe_2O_3 \,.\, (1 - x)\, Cr_2O_3$. If D is the number of edges deleted in G_o to form the new graph G and one Fe^{3+} is inserted per edge deletion (to preserve charge neutrality), then:

$$\frac{\text{Moles } Fe^{3+}}{\text{Moles } Cr^{3+}} = \frac{D}{N} = \frac{2x}{2(1-x)} \tag{3.3}$$

Then, $A(G) = (3/2)N - D$, or

$$A(G) = N\frac{3-5x}{2(1-x)} \tag{3.4}$$

Unlike $X(G_o)$, the term X(G) cannot be calculated directly because it is not known which particular edges have been deleted from G_o to form G. A stochastic calculation is employed, the details of which have been given previously [1, 2]. The result is:

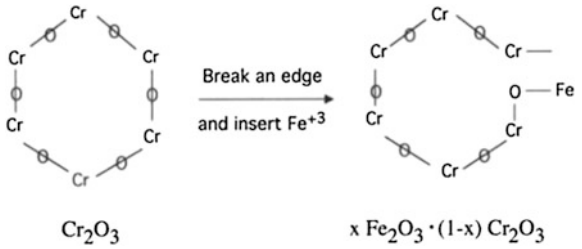

Fig. 3.2 Insertion of Fe^{3+} ions into the graph for Cr_2O_3. Reproduced by permission of ECS—The Electrochemical Society

$$X(G) = \frac{(1/3)^5 N(3-5x)}{(1-x)^5}\{24x^4 + 24(2^{1/2})x^3(3-5x) + 4(3^{1/2}+3)x^2(3-5x)^2 + 6^{1/2}x(3-5x)^3 + (1/2)(3-5x)^4\} - 1 \tag{3.5}$$

Insertion of expressions for A(G), X(G), $A(G_o)$, and $X(G_o)$ into Eq. (3.2) gives the result (after much algebra):

$$\delta = \frac{2(1/3)^6(3-5x)^2}{(1-X)^6}\{24x^4 + 24(2^{1/2})x^3(3-5x) + 4(3^{1/2}+3)x^2(3-5x)^2 + 6^{1/2}x(3-5x)^3 + (1/2)(3-5x)^3\} - 1 \tag{3.6}$$

The behavior of δ as a function of the composition of the oxide film is shown in Fig. 3.3. It can be seen that an atomic fraction of Fe^{3+} in the oxide film of 0.70 suffices to break down the –Cr–O–Cr– network. Said differently, there is a critical concentration of 0.30 mol fraction Cr^{3+} to provide a continuous network of –Cr–O–Cr– linkages in the oxide film.

From the XPS data of Asami et al. [4] for Fe-Cr alloys in 1 M H_2SO_4 a cation fraction of $0.30Cr^{3+}$ in the oxide film corresponds to a metal alloy composition of approximately 13 at.%. See Fig. 3.4. From in situ XANES data of Oblansky et al. [5] for Fe-Cr binary alloys in an acetate buffer a cation fraction of $0.30Cr^{3+}$ in the oxide film also corresponds to a metal alloy composition of approximately 13 at.%. See also Fig. 3.4.

Thus, this graph theory approach explains the well-known observation that 13 at.% Cr induces passivity in Fe-Cr alloys.

The graph theory approach has now successfully explained the occurrence of critical alloy compositions in 18 different binary alloys [1, 2, 6, 7]. Some examples are listed in Table 3.1.

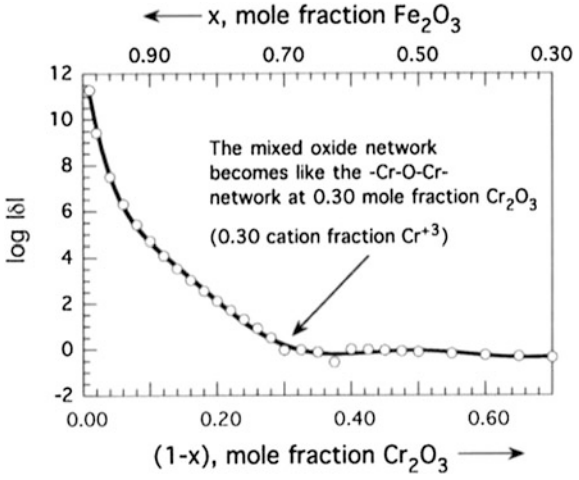

Fig. 3.3 The behavior of the connectivity function δ as a function of the oxide composition for $Fe_2O_3 \cdot Cr_2O_3$ mixed oxides. Reproduced by permission of Elsevier

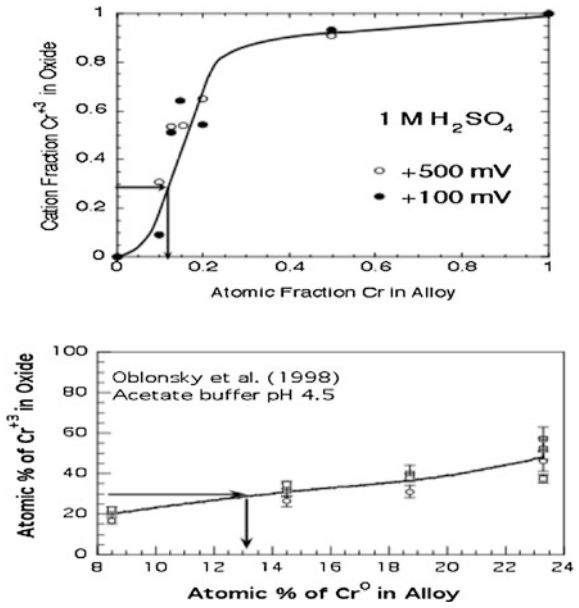

Fig. 3.4 Cr^{3+} content in the passive film on Fe-Cr binary alloys as a function of the chromium content in the alloy after immersion (*top*) in 1 M H_2SO_4 [4]. Reproduced by permission of Elsevier. (*Bottom*) After immersion in an acetate buffer [5]. Reproduced by permission of ECS—The Electrochemical Society

Fe-Cr-Ni Alloys

This graph theory approach has been extended to Fe-Cr-Ni ternary alloys [8] because Fe-18Cr-8Ni (304 stainless steel) is a workhorse among the stainless steels.

The approach is similar to that for Fe-Cr binary alloys except that here there are two foreign cations (Ni^{2+} and Fe^{3+}) which can disrupt continuous threads of –Cr–O–Cr– bridges in the Cr_2O_3 network. See Fig. 3.5. Let $xFe_2O_3 \cdot yNiO \cdot (1 - x - y)$

Table 3.1 Some results from the graph theory model of passivity [1, 2, 6, 7]

Alloy	Critical mole fraction of oxide from δ	Calculated cationic mole fraction in oxide	Corresponding alloy composition from surface analysis data	Observed critical alloy composition from corrosion data
Fe-Cr	$0.30Cr_2O_3$	$0.30Cr^{3+}$	13 at.% Cr [4, 5]	13 at.% Cr [9]
Ni-Cr	$0.17Cr_2O_3$	$0.29Cr^{3+}$	7 at.% Cr [10]	8–11 at.% Cr [11]
Al-Cr	$0.31Cr_2O_3$	$0.31Cr^{3+}$	48 at.% Cr [12]	40–50 at.% Cr [13]
Co-Cr	$013Cr_2O_3$	$0.23Cr^{3+}$	6 at.% Cr [14]	9–11 at.% Cr [15]
Cr-Mo	$0.28MoO_2$	$0.16Mo^{4+}$	21 at.% Mo [16]	20 at.% Mo [16]
W-Zr	$0.21ZrO_2$	$0.21Zr^{4+}$	11 at.% Zr [17]	15 at.% Zr [17]

Cr_2O_3 be the composition of the mixed oxide. For insertion of Ni^{2+} ions into the mixed oxide film, $(3/2)Ni^{2+}$ ions must be inserted on the average for each edge deletion in order to preserve charge neutrality in the resulting oxide. One Fe^{3+} must be inserted for each Cr^{3+} which is replaced in the continuous network.

Following the procedure used for the Fe-Cr binary alloys the result for Fe-Cr-Ni ternary alloys is:

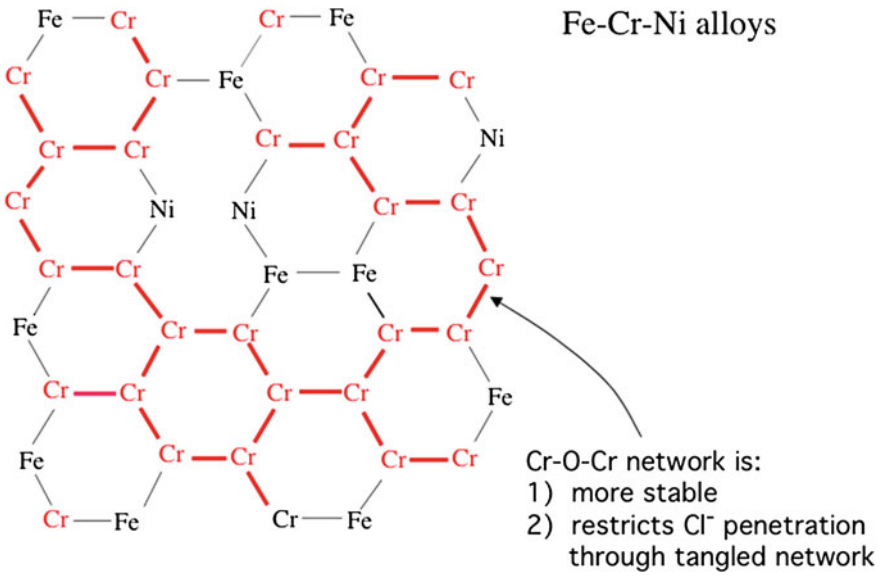

Fig. 3.5 Schematic representation of a continuous –Cr–O–Cr– network on an Fe-Cr-Ni ternary alloy. The oxide also contains Fe^{3+} and Ni^{2+} ions. Reproduced by permission of ECS—The Electrochemical Society

$$\begin{aligned}\delta = \frac{2(1/9)^6(9-15x-11y)^2}{(1-x-y)^6}\{(3/2)[2(3x+y)]^4 \\ + 3(2^{1/2})[2(3x+y)]^3(9-15x-11y) \\ + (3+(3)^{1/2})[2(3x+y)]^2(9-15x-11y)^2 \\ + 6^{1/2}[2(3x+y)](9-15x-11y)^3 \\ + (1/2)(9-15x-11y)^4\} - 1\end{aligned} \tag{3.7}$$

For binary Fe-Cr alloys, there is only one variable (x) in Eq. (3.6) and δ has one root between x = 0 and x = 1. For the case of Fe-Cr-Ni alloys, the root of δ depends both on x(Fe_2O_3) and on y(NiO). The solution is a straight line in x and y.

One method of solving Eq. (3.7) is to assume a fixed value of y(NiO) and to solve graphically for the value of x(Fe_2O_3) which gives δ = 0. The mole fraction of Cr_2O_3 in the oxide film is (1 − x − y).

Figure 3.6 shows the behavior of δ as a function of the composition of the oxide film for a fixed value of y = 0.20. It can be seen that δ = 0 when x = 0.52 (mole fraction Fe_2O_3) and (1 − x − y) = 0.28 (mole fraction Cr_2O_3). That is a mole fraction of 0.28Cr_2O_3 in the oxide film provides a continuous –Cr–O–Cr– network (when y = 0.2).

This is the minimum amount of Cr_2O_3 required because larger mole fractions of Cr_2O_3 also produce small values of δ. From simple stoichiometry 0.28 mol fraction of Cr_2O_3 is equivalent to 0.31 cation fraction of Cr^{3+}, 0.11 cation fraction Ni^{2+}, and 0.58 cation fraction Fe^{3+}. This point lies on the heavy straight line in the triangular diagram in Fig. 3.7, which shows roots of Eq. (3.6) for additional fixed values of y.

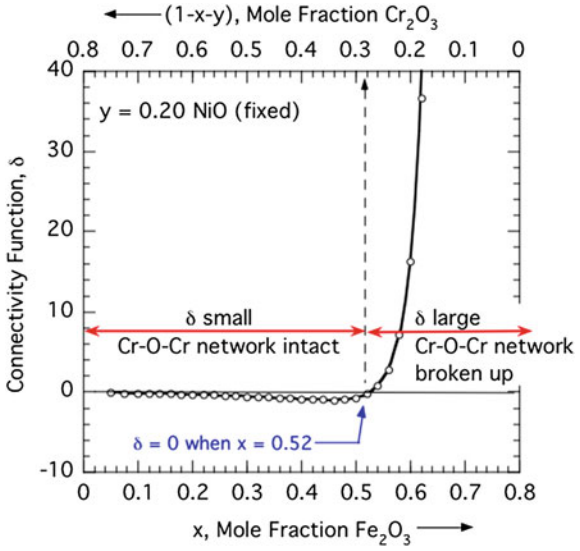

Fig. 3.6 Behavior of the conductivity parameter δ near its root as a function of the Cr_2O_3 mixed oxide network which also contains Fe^{3+} and Ni^{2+} ions. (The *curve* is shown for a fixed mole fraction of 0.20 M NiO). Reproduced by permission of ECS—The Electrochemical Society

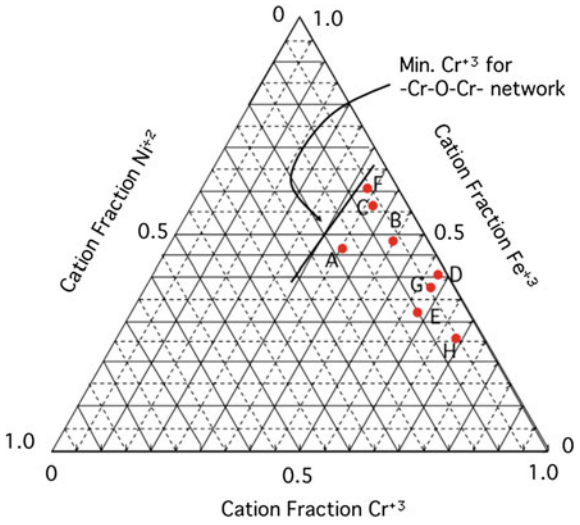

Fig. 3.7 Comparison of calculated and experimental compositions of oxide films on Fe-Cr-Ni alloys [8]. Reproduced by permission of ECS—The Electrochemical Society

Figure 3.7 also shows experimentally observed compositions of oxide films on various Fe-Cr-Ni alloys in different environments. The cation fraction of Cr^{3+} varies from 0.33 to 0.67, i.e., from the minimum value of Cr^{3+} required to higher values indicative of Cr^{3+} enrichment.

Finally it should be noted that when y = 0, Eq. (3.7) reduces to the case for Fe-Cr binary alloys, i.e., Eq. (3.6).

References

1. E. McCafferty, Corros. Sci. **42**, 1993 (2000)
2. E. McCafferty, Electrochem. Solid State Lett. **3**, 28 (2000)
3. J.J. Meghirditchian, J. Am. Chem. Soc. **113**, 395 (1991)
4. K. Asami, K. Hashimoto, S. Shimodaira, Corros. Sci. **18**(151), 1993 (1978)
5. L.J. Oblansky, M.P. Ryan, H.S. Isaacs, J. Electrochem. Soc. **145**, 1922 (1998)
6. E. McCafferty, Corros. Sci. **44**, 1393 (2002)
7. E. McCafferty, J. Electrochem. Soc. **149**, B333 (2000)
8. E. McCafferty, J. Electrochem. Soc. **154**, C571 (2007)
9. P.F. King, H.H. Uhlig, J. Phys. Chem. **63**, 2026 (1959)
10. S. Boudin, J.-L. Vignes, G. Lorang, M. da Cunha Bela, G. Blondiaux, S.M. Khailov, J. P. Jacobs, R.H. Brangersma, Surf. Interface Anal. **22**, 462 (1994)
11. H.H. Uhlig, Z. Elektrochem. **62**, 700 (1958)
12. E. Akiyama, A. Kawashima, K. Asami, K. Hashimoto, Corros. Sci. **38**, 279 (1996)
13. E. Akiyama, H. Habazaki, A. Kawashima, K. Asami, K. Hashimoto, Mater. Sci. Eng. A **A226–A228**, 920 (1997)

14. A.S. Lim, A. Atrens, Appl. Phys. A **54**, 270 (1992)
15. A.P. Bond, H.H. Uhlig, J. Electrochem. Soc. **107**, 88 (1960)
16. P.Y. Park, E. Akiyama, A. Kawashima, K. Asami, K. Hashimoto, Corros. Sci. **37**, 1843 (1995)
17. J. Bhattaira, E. Akiyama, H. Habazaki, A. Kawashima, K. Asami, K. Hashimoto, Corros. Sci. **39**, 355 (1997)

Chapter 4
Uptake of Chloride Ions and the Pitting of Aluminum

Introduction

Aluminum and its alloys undergo pitting in chloride solutions. The protective oxide film present in neutral solutions breaks down in the presence of chloride ions and pitting ensues.

Aluminum is usually alloyed with various elements to improve its mechanical strength, and these alloying additions result in the formation of intermetallic second-phase particles which can disrupt the passive film on the alloy surface.

Chapter 1 considers briefly the pitting of aluminum from the standpoint of an acid-base phenomenon. More information is given here.

Sequence of Steps

The pitting of pure aluminum occurs in a sequence of several steps [1], as shown schematically in Fig. 1.17. The *first step* in the pitting process is the adsorption of chloride ions onto the oxide-covered surface. It is well known that the outermost surface of an oxide or an oxide film is covered with a layer of hydroxyl groups (see Chaps. 1 and 4). For oxide films on aluminum, these hydroxyl groups interact with protons in solution to produce a positively charged surface:

$$\mathrm{AlOH_{surf}} + \mathrm{H^{+}_{(aq)}} = \mathrm{AlOH_2^{+}{}_{surf}} \tag{4.1}$$

Then the adsorption of chloride ions occurs mainly through the operation of attractive coulombic forces between the positively charged oxide surface and the negatively charged Cl^{-} ion.

E. McCafferty, *Surface Chemistry of Aqueous Corrosion Processes*,
SpringerBriefs in Materials, DOI 10.1007/978-3-319-15648-4_4

XPS Studies

Chloride ions next *penetrate the oxide film*, as shown by X-ray photoelectron spectroscopy (XPS). Figure 4.1 shows an XPS Cl 2p spectrum for an aluminum surface held below its pitting potential [2, 3].

Each Cl 2p spectrum is actually a doublet, and there are two distinct sets of doublets. The lower binding energy doublet was removed by sputtering, indicating that this doublet was characteristic of surface chloride. The higher binding energy doublet persisted after sputtering so that this species is due to chloride which has penetrated the oxide film.

Figure 4.2 shows that the concentration of bulk chloride in the oxide film increases as the electrode potential approaches the pitting potential. This shows that the presence of chloride ions in the oxide film promotes film breakdown and pitting. Previous studies have shown that the pitting potential of aluminum is lower the higher the chloride concentration in aqueous solution. See Chap. 1. This provides further evidence that chloride ions promote film breakdown and pitting.

The exact mechanism by which chloride ions penetrate the oxide film is not known with certainty. There are several possibilities: transport of chloride ions through the oxide film through oxygen vacancies [4–6], (ii) transport of chloride ions through the oxide film through water channels [7, 8], or (iii) localized oxide film thinning or dissolution [2, 9].

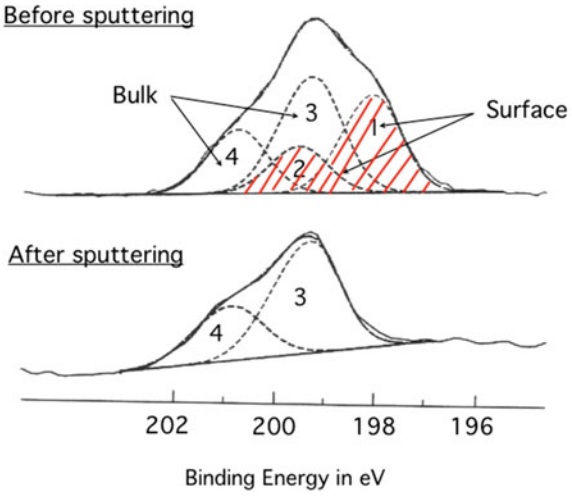

Fig. 4.1 XPS $2p_{3/2}$-$2p_{1/2}$ of chloride on aluminum for a sample polarized at −0.750 V versus S.C.E. before and after sputtering [3]. Reproduced by permission of ECS—The Electrochemical Society

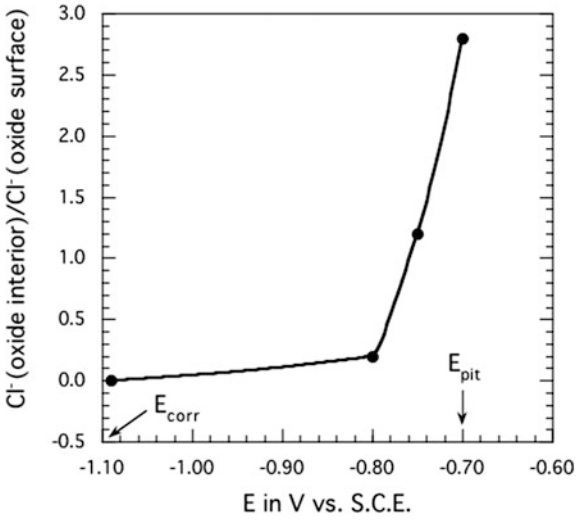

Fig. 4.2 XPS measurement of the uptake of Cl^- by the passive film on aluminum as a function of electrode potential [2]. Reproduced by permission of ECS—The Electrochemical Society

Formation of Blisters

The propagation of corrosion pits on aluminum occurs with the *formation and rupture of blisters* at the aluminum/oxide interface [10]. As propagation proceeds blisters rupture when the hydrogen pressure within the blister becomes sufficiently large. See Fig. 4.3 which shows a ruptured blister. Figure 4.4 shows a schematic diagram of the growth and rupture of oxide blisters on aluminum. When the blister ruptures, the contents of the corrosion pit are opened to the aqueous solution.

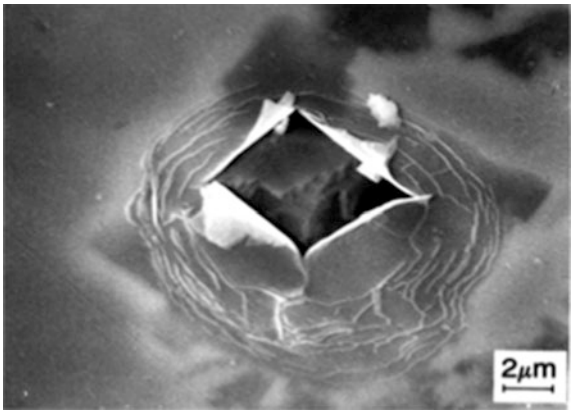

Fig. 4.3 A ruptured oxide blister on aluminum. *Photograph* courtesy of P.M. Natishan and reproduced by permission of ECS—The Electrochemical Society

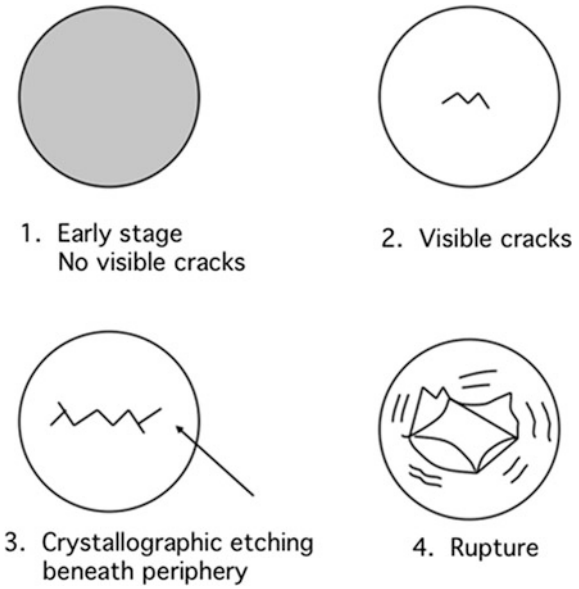

Fig. 4.4 Schematic drawing of the growth and rupture of an oxide blister on aluminum

Localized Corrosion Cells

Experimentally determined values for the internal pH and electrode potential E within several different types of localized corrosion cells are given in Fig. 4.5 [11],

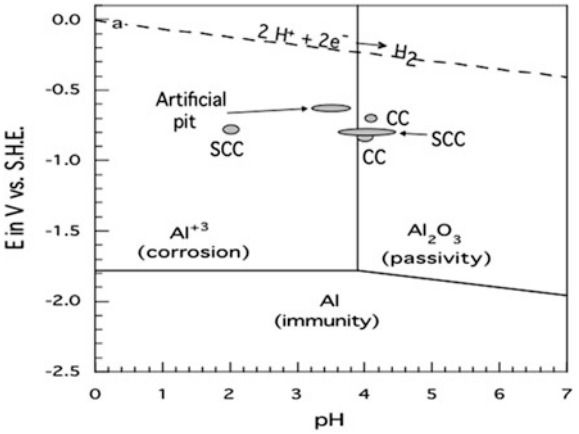

Fig. 4.5 The electrode potential and pH within localized corrosion cells on aluminum superimposed on a Pourbaix diagram for aluminum. *CC* refers to crevice corrosion [12, 13], and *SCC* to stress-corrosion cracking [14, 15]. The results for an artificial pit on aluminum are due to Hagyard and Santhipillai [16]

where they are superimposed on a conventional Pourbaix diagram for aluminum. Each of the data sets for the various localized corrosion cells either lie in the region of corrosion on the Pourbaix diagram or are very close to this region. Data for the various forms of localized attack lie below the "a" line for hydrogen evolution showing that hydrogen evolution is thermodynamically possible in each of these cases of localized corrosion. Hydrogen bubbles have in fact been observed for aluminum in active crevices [12].

References

1. E. McCafferty, Corros. Sci. **45**, 1421 (2003)
2. S. Yu, W.E. O'Grady, D.E. Ramaker, P.M. Natishan, J. Electrochem. Soc. **147**, 2952 (2000)
3. P.M. Natishan, W.E. O'Grady, E. McCafferty, D.E. Ramaker, K. Pandya, A. Russell, J. Electrochem. Soc. **147**, 2952 (2000)
4. C.L. McBee, J. Kruger, in *Localized Corrosion*, ed. by R.W. Staehle, B.F. Brown, J. Kruger, A. Agrawahl (NACE, Houston, 1974), p. 252
5. C.E. Chin, C.Y. Chao, D.D. Macdonald, J. Electrochem. Soc. **128**, 1194 (1981)
6. D.D. Macdonald, J. Electrochem. Soc. **139**, 2434 (1991)
7. J.O'M. Bockris, L.V. Minevski, J. Electroanal. Chem. **349**, 375 (1993)
8. J.O'M. Bockris, Y. Kang, J. Solid State Electrochem. **1**, 17 (1997)
9. T.H. Nguyen, R.T. Foley, J. Electrochem. Soc. **127**, 2563 (1980)
10. P.M. Natishan, E. McCafferty, J. Electrochem. Soc. **136**, 53 (1989)
11. E. McCafferty, *Introduction to Corrosion Science* (Springer, New York, 2010), p. 305
12. D.W. Siitari, R.C. Alkire, J. Electrochem. Soc. **129**, 481 (1982)
13. N.J.H. Holroyd, G.M. Scamans, R. Hermann, in *Corrosion Chemistry within Pits, Crevices, and Cracks*, ed. by A. Turnbull (Her Majesty's Stationary Office, London, 1987), p. 495
14. J.A. Davis, in *Localized Corrosion*, ed. by R.W. Staehle, B.F. Brown, J. Kruger, A. Agrawal (NACE, Houston, 1974), p. 168
15. O.V. Kurov, R.K. Melekhov, Protection Meals **15**, 249 (1979)
16. T. Hagyard, J.R. Santhipillai, J. Appl. Chem. **9**, 323 (1959)

Chapter 5
Formation of Water Films on the Iron Oxide Surface

Introduction

One of the earliest quantitative observations in the field of corrosion science was that there is a critical relative humidity below which atmospheric corrosion is negligible and above which corrosion occurs [1]. Figure 5.1 shows Vernon's results for iron exposed to water vapor containing 0.01 % SO_2 [1]. It can be seen that the corrosion of iron occurs above 60 % relative humidity. The critical relative humidity is typically 50–70 % for most metals.

This communication reviews previous work by the author on the uptake of water vapor on α-Fe_2O_3. This earlier work is discussed here in view of the theme of this monograph.

Experimental

All experiments were carried out on α-Fe_2O_3 powder having a nominal B.E.T. surface area of 10 m^2/g. The adsorption of water from the vapor phase was studied using conventional adsorption isotherms and dielectric relaxation techniques (known popularly today as AC impedance and usually applied to the solid/liquid interface rather than the solid/vapor interface). Experimental details are given elsewhere [2, 3].

The dielectric sample cell consisted of two concentric stainless steel cylinders between which was packed the α-Fe_2O_3 powder. Controlled amounts of water vapor were introduced into the dielectric cell. If the adsorbed water molecule were able to rotate in the applied alternating signal, then a capacitance and dielectric loss tangent (tan δ) was measured. The dielectric constant is given by $\varepsilon' = C/C_0$ where C_0 is the capacitance of the empty cell. The dielectric loss ε'' is given by $\tan\delta = \varepsilon''/\varepsilon'$.

E. McCafferty, *Surface Chemistry of Aqueous Corrosion Processes*,
SpringerBriefs in Materials, DOI 10.1007/978-3-319-15648-4_5

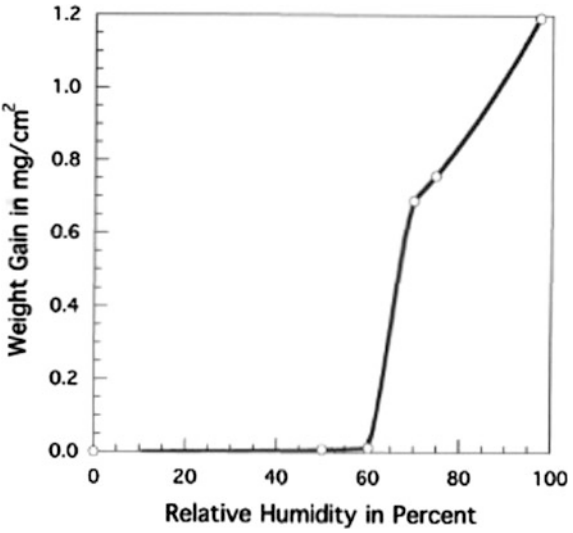

Fig. 5.1 Corrosion of iron in air containing 0.01 % SO_2 after 55 days of exposure showing the effect of a critical relative humidity (approximately 60 %). Redrawn from Ref. [1] by permission of the Royal Society of Chemistry

Results and Discussion

Adsorption isotherms for water vapor at various temperatures are shown in Fig. 5.2. The number of layers adsorbed is taken from the B.E.T.

Brunauer-Emmett-Teller surface areas and the cross-sectional area of the water molecule. Coverages of water refer to the number of physically adsorbed water layers beyond the underlying hydroxyls.

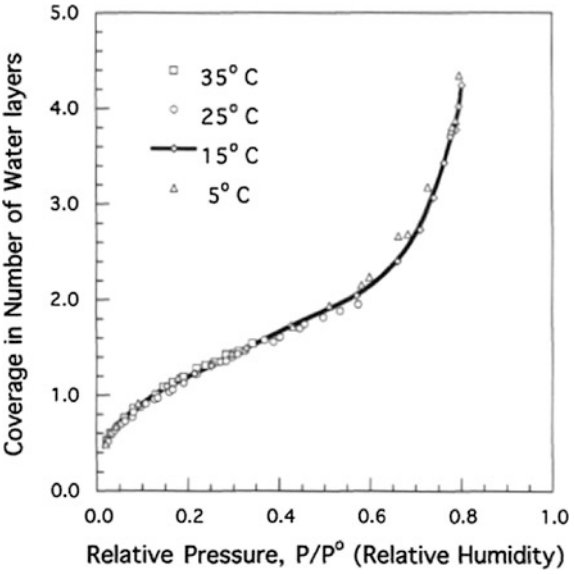

Fig. 5.2 Adsorption isotherms for water vapor on α-Fe_2O_3 showing that multimolecular layers of adsorbed water are formed at a relative humidity of 60 % and higher [3, 6]. By permission of Elsevier

Figure 5.2 shows that at a relative pressure of 0.6 (relative humidity 60 %), the third layer of water molecules starts to form and at higher relative pressures multiple water layers ensue. Thus the critical relative humidity for corrosion corresponds to the adsorption of multimolecular layers of water on the oxide-covered metal surface. If the water layer contains ionic impurities either by leaching from the oxide film or by incorporation from the atmosphere, then a thin-layer electrolyte is formed.

Figure 5.3 shows the dielectric constant as a function of coverage for a frequency of 100 Hz. The first layer of physically adsorbed water does not cause any change in the dielectric constant. This behavior is due to the existence of a monolayer in which the physically adsorbed species are held rigidly by double hydrogen bonding to underlying hydroxyl groups. See Fig. 5.4.

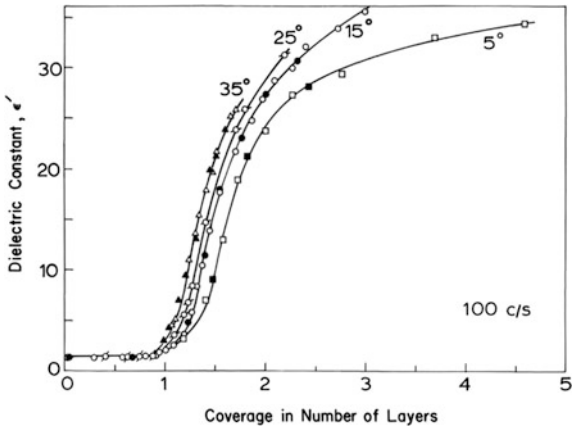

Fig. 5.3 Dielectric constant at 100 c/s as a function of coverage for various temperatures. (*Solid points* indicate desorption). Reproduced from Ref. [2] with permission of the Royal Society of Chemistry

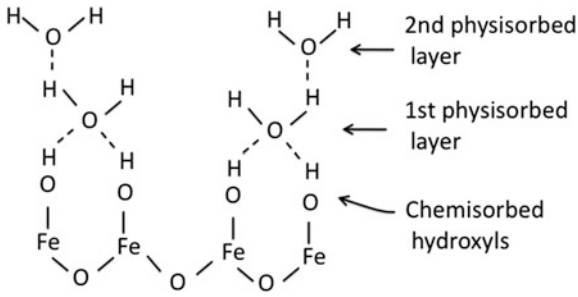

Fig. 5.4 Schematic representation of water adsorption on α-Fe_2O_3. Reproduced from Ref. [3] with permission of the Royal Society of Chemistry

The dielectric constant rises sharply with the start of the second water layer. This increase is due to an increased tendency of water molecules to respond to the alternating field (Debye dispersion process), so that these multilayers must be more mobile than the first physically adsorbed layer. This information is also in accord with the notion that thin layers of adsorbed water start to form at the critical relative humidity for corrosion.

Typical Cole-Cole plots of ε″ versus ε′ are shown in Fig. 5.5. These plots allow calculation of the characteristic relaxation frequency f_{char} [4]. For the formation of multilayers of adsorbed water on α-Fe_2O_3, the characteristic frequency is approximately 10–20 kc/s, characteristic of a hydrogen bonded network. Cole-Cole plots are also called Nyquist plots or complex plane plots.

The tails appearing on the Cole-Cole plots indicate that dielectric processes other than simple Debye dispersion are operative. They are due to surface d.c. conductance, and it is interesting to note that they appear when multimolecular layers of water are formed.

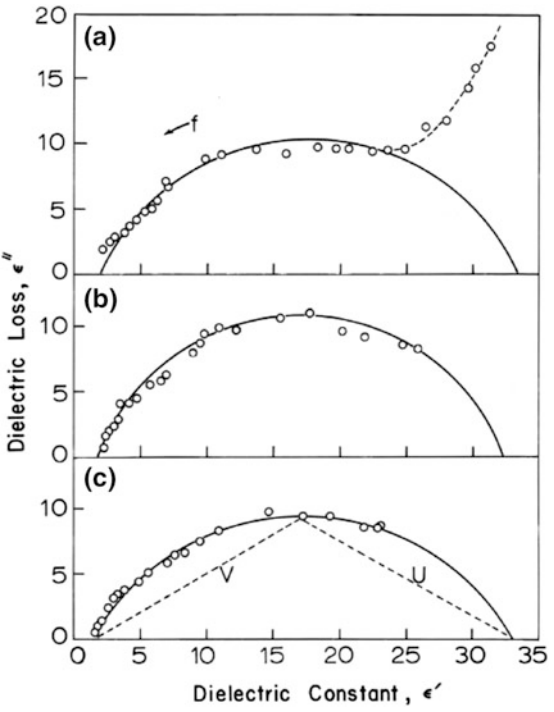

Fig. 5.5 Cole-Cole arc plots for several coverages of water vapor adsorbed on α-Fe_2O_3 at 15 °C. (**a**) θ = 1.70, f_{char} = 176 c/s, (**b**) θ = 1.82, f_{char} = 284 c/s, (**c**) θ = 2.28, f_{char} = 1.09 kc/s. Reproduced from Ref. [2] with permission of the Royal Society of Chemistry

Formation of Liquid-Like Layers

The formation of liquid-like films of water on oxide or oxide-covered surfaces proceeds by the following sequence of events.

1. The first layer of adsorbed water vapor on a bare oxide surface chemisorbs to form a layer of surface hydroxyls. See Fig. 5.6.
2. The first layer of physisorbed water vapor is immobile and is doubly hydrogen bonded to the underlying layer of surface hydroxyls.
3. Successive layers of physisorbed water vapor are more mobile.

Supporting evidence for this model comes from immersional calorimetry measurements and from entropy calculations. Details are given elsewhere [5, 6]. The heat of immersion decreases from approximately 1,000 ergs/cm^2 for the bare oxide surface to 400 ergs/cm^2 as the chemisorbed layer of hydroxyls is successively filled in. As the next layer of water molecules is formed, the heat of immersion decreases further to 100 ergs/cm^2, indicative that this layer is physically absorbed. (This is the layer of water molecules doubly hydrogen bonded to the underlying layer of hydroxyls).

The same conclusion is reached on the basis of entropy considerations. The experimentally determined integral entropy of adsorption is given from multi-temperature adsorption isotherms to be:

$$\left(\frac{\partial \ln P}{\partial T}\right)_{\phi} = -\frac{\Delta S_{\text{ads}}}{RT} \tag{5.1}$$

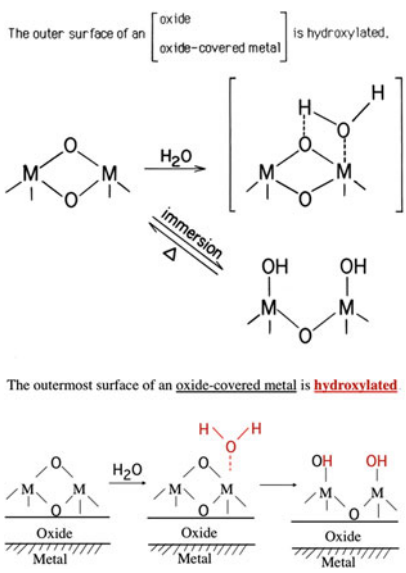

Fig. 5.6 Adsorption of water vapor on a clean oxide surface

where Φ is the spreading pressure given by:

$$\phi = RT \int_{P=0}^{P=P_0} \Gamma \, \mathrm{d} \ln P, \tag{5.2}$$

and Γ is the surface concentration of adsorbed water molecules.

The theoretical integral entropy was calculated for two cases: (i) an immobile physisorbed water layer (i.e. a layer which is doubly hydrogen bonded to the underlying hydroxyl groups, and (ii) a mobile layer of adsorbed water molecules. The calculated entropy change upon adsorption includes contributions from translational, rotational, and vibrational changes. For a mobile adsorbed film, the adsorbed molecules lose one degree of translational freedom and no degrees of rotational freedom. For an immobile adsorbed film, the adsorbed gas loses all its translational freedom and three degrees of rotational freedom if the water molecule is doubly hydrogen bonded to the layer of underlying hydroxyls. There are contributions due to surface vibrational modes for both immobile and mobile adsorption. Details of these calculations are given elsewhere [6].

Figure 5.7 compares the experimental entropy of adsorption with the calculated values for mobile or immobile water layers. It can be seen that the experimental entropy of adsorption agrees quite well with the calculated values for an immobile water layer, but not a mobile layer. This lends support to the notion that the first physisorbed water layer is doubly hydrogen bonded to the underlying hydroxyl groups.

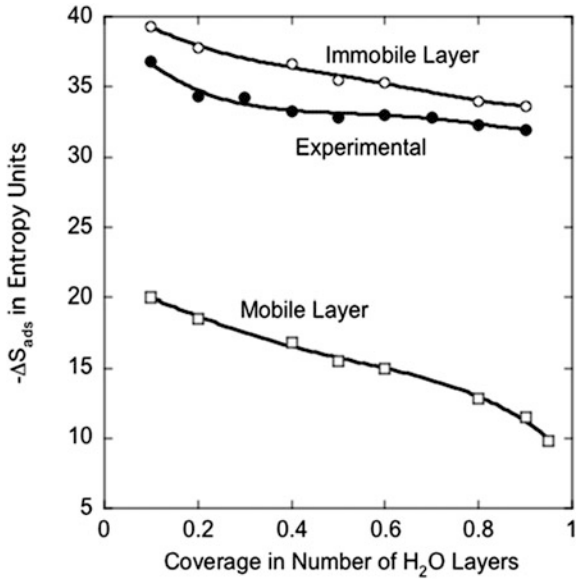

Fig. 5.7 Comparison of experimental entropies of adsorption at 25 °C with theoretical entropies for mobile and immobile adsorbed films of water vapor [3, 6]. Reproduced by permission of Elsevier

References

1. W.H.J. Vernon, Trans. Faraday Soc. **31**, 1668 (1935)
2. E. McCafferty, V. Pravdic, A.C. Zettlemoyer, Trans. Faraday Soc. **66**, 1720 (1970)
3. E. McCafferty, A.C. Zettlemoyer, Discuss. Faraday Soc. **52**, 239 (1971)
4. K.S. Cole, R.H. Cole, J. Chem. Phys **9**, 341 (1941)
5. A.C. Zettlemoyer, E. McCafferty, Z. Physik Chem. N. F **64**, 41 (1969)
6. E. McCafferty, A.C. Zettlemoyer, J. Colloid Interface Sci. **34**, 452 (1970)

Chapter 6
Corrosion Inhibition by Fluorinated Aliphatic Compounds

Introduction

Using fundamental principles of corrosion inhibition it is possible to "tailor-make" effective corrosion inhibitors. Much useful information is available from the field of surface chemistry.

For example, carboxylic acids are surface active agents which adsorb at the metal surfaces by donation of electrons from the oxygen in the –COOH group to the metal. When adsorbed from solutions of non-electrolytes, the hydrocarbon tails are extended outward from the surface to form a close-packed hydrophobic monolayer. It is well known that surfaces terminating in fluorocarbon groups are less energetic than hydrocarbon groups and are less wettable than are surfaces terminating in hydrocarbon groups.

Fluorinated Carboxylic Acids and Amines

If the contact angle θ for a liquid on a solid is small or zero, then the liquid is said to wet the solid. For large values of θ, wetting does not occur. See Fig. 6.1.

Figure 6.2 compares wettability data for films of fluorinated and conventional carboxylic acids preadsorbed onto platinum or glass substrates [1]. The wetting liquid is methylene iodide, an organic liquid often used to rate surfaces. The higher the contact angle, the less wettable and the lower the energy of the surface. Figure 6.2 shows that fluorine substitution produces a "Teflon-like" surface with as little as five carbon atoms.

Thus, the idea of using fluorinated molecules as corrosion inhibitors is intriguing because of the possibility of in situ formation of a low-energy "Teflon-like" surface. The actual configuration of the adsorbed inhibitor would not seem important as either a flat or vertical configuration would present low-energy surface groups to the solution, as shown in Fig. 6.3.

E. McCafferty, *Surface Chemistry of Aqueous Corrosion Processes*,
SpringerBriefs in Materials, DOI 10.1007/978-3-319-15648-4_6

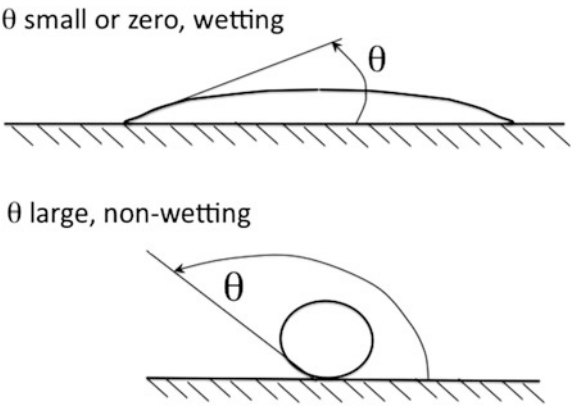

Fig. 6.1 Contact angles for (*top*) a wetting liquid and (*bottom*) for a non-wetting liquid on a solid surface

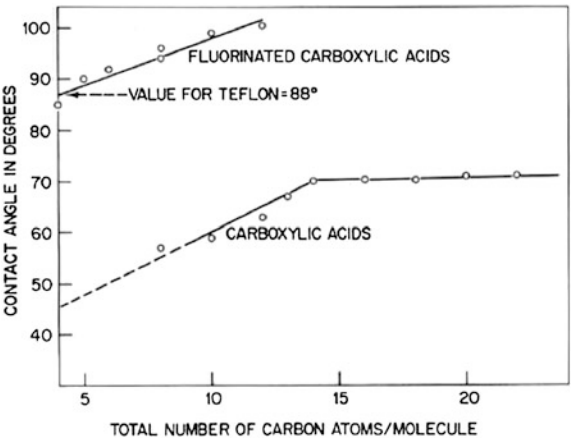

Fig. 6.2 Experimentally measured contact angles for water on films of conventional carboxylic acids and on fluorinated carboxylic acids [1]

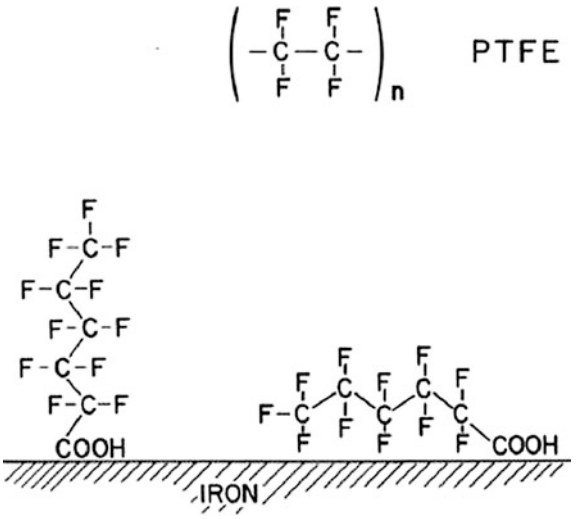

Fig. 6.3 Fluorinated carboxylic acids adsorbed in the vertical and flat configurations compared with poly (tetrafluoroethylene)

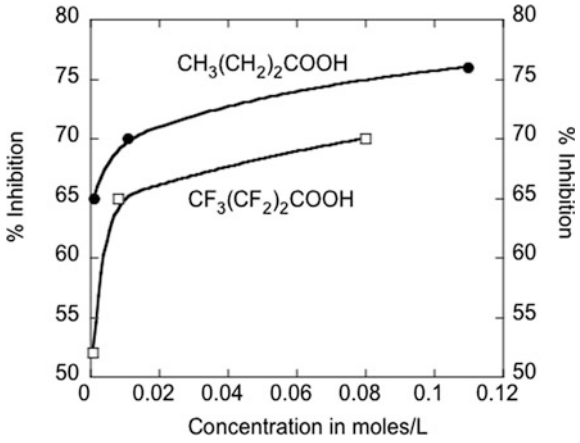

Fig. 6.4 Comparison of $CH_3(CH_2)_2COOH$ and $CF_3(CF_2)_2COOH$ as corrosion inhibitors for iron in 3M HCl

Experimental Results

Corrosion rates were determined for high purity-iron wires or high-purity flat samples using electrochemical polarization curves or colorimetric analysis of the electrolyte containing freely corroding iron. The corrosive medium was 3M HCl with and without added butyric acids. Experimental details are given elsewhere [2, 3].

The efficiency % I (% inhibition) of the inhibitor is given in the usual way as:

$$\%I = (i_u - i)/i_u \tag{6.1}$$

where i_u is the corrosion rate of the uninhibited iron (i.e., its open-circuit corrosion rate) and i is the corrosion rate of the inhibited iron. Figure 6.4 shows that perfluorobutyric acid $CF_3(CF_2)_2COOH$ is a poorer—not better—inhibitor than its conventional analog, $CH_3(CH_2)_2COOH$.

The reason is that the electronegativity effect of F atoms adjacent to the carboxyl group is predominant over the potential increase in hydrophobic character. That is, the strongly electronegative F atoms withdraw electrons from the –COOH group to make it a stronger acid and weaker base. Thus, the density of electrons available for bonding with the iron surface is decreased.

This effect is schematically illustrated in Fig. 6.5, which also lists ionization constants. Thus, the weaker bond strength with the totally fluorinated acid results in its poorer inhibitive effect.

However, Fig. 6.5 also shows that the presence of methylene groups interposed between the surface active carboxyl group and the fluorocarbon tail shields the –COOH group from the inductive effect of the fluorine atom.

These observations lead us to suggest that the most effective fluorinated compounds should be only partially fluorinated, as shown in Fig. 6.6. The chain should feature several "insulating" $–CH_2–$ segments which shield the –COOH group from the fluorine atoms in the hydrophobic tail.

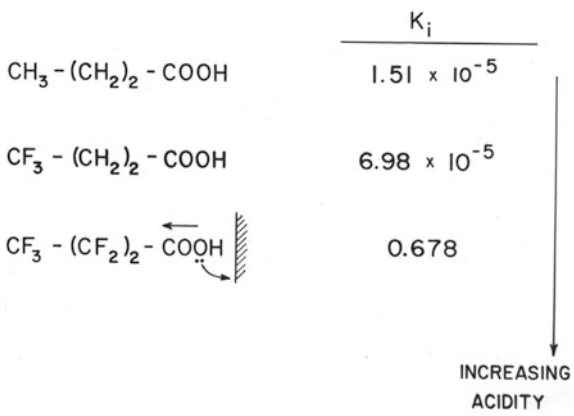

Fig. 6.5 Effect of fluorine substitution on the ionization constant of butyric acid

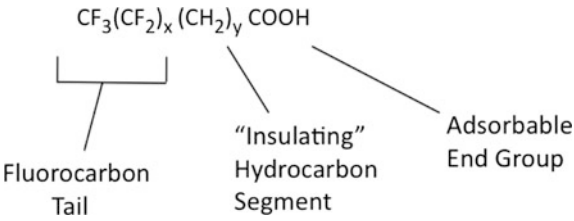

Fig. 6.6 A "tailor-made" corrosion inhibitor

Table 6.1 shows measured corrosion rates for iron in deaerated 3M HCl with and without added propyl amine $CH_3CH_2CH_2NH_2$ and pentafluoropropyl amine $CF_3CF_2CH_2NH_2$. Table 6.1 shows that the partially fluorinated amine is a better inhibitor than its conventional analog.

It is interesting to note that pentafluoropropyl amine is a better inhibitor than propyl amine despite the fact that the latter is the stronger base. The beneficial aspect of an improved hydrophobic tail overcomes the detrimental aspect of a weaker electron donor.

Table 6.1 Results for the two propyl amines

Compound	% I	pK_a*
$CH_3CH_2CH_2NH_2$	59	10.53
$CF_3CF_2CH_2NH_2$	77	5.7

* Higher values of pK_a correspond to stronger bases and better electron donors

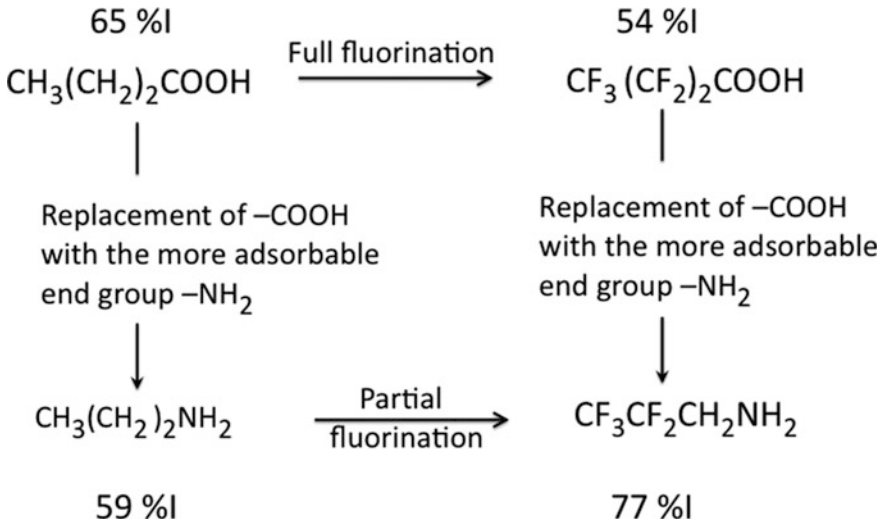

Fig. 6.7 Effect of fluorination and of replacing a –COOH end group with a $–NH_2$ end group on the corrosion of iron in 3M HCl. Inhibitor concentrations are 1×10^{-3} M in each case

The results for the limited set of experiments discussed here are summarized in Figs. 6.6 and 6.7. In brief, partial fluorination is better than full fluorination.

Also, amines are better inhibitors than their corresponding carboxylic acids.

Suggestions for Further Work

The effect of systematic progressive fluorination along the hydrocarbon chain should be investigated. If solubility proves to be a problem, then the fluorocarbon can be preadsorbed onto the metal surface by adsorption from solution or by "painting" the fluorocarbon onto the metal surface. Aromatic (cyclic) fluorocarbons can also be investigated.

References

1. E.G. Shafrin, W.A. Zisman, Upper limits for the contact angles of liquids on solids, NRL report 5985, Naval Research Laboratory (1963)
2. E. McCafferty, Corrosion inhibition by hydrophobing compounds. Paper No. 72, presented at corrosion/74, Chicago, IL, 4–8 Mar 1974
3. E. McCafferty, M.K. Harvey, Reports of NRL progress (Nov 1976), p. 23